RESEARCH TRIANGLE INSTITUTE

170-01106

GEODETIC SATELLITE ALTIMETER STUDY

FINAL ENGINEERING REPORT

N70-28484
(ACCESSION NUMBER)
(THRU)
184
(PAGES)
1
(CODE)
CR-110085
(NASA CR OR TMX OR AD NUMBER)
07
(CATEGORY)
FACILITY FORM 602

A Study of the Capabilities of the Geodetic Satellite Altimeter to Measure Ocean-Surface Characteristics

April 1970

Prepared Under

NASA CONTRACT NO. NASW 1909

For

The Geodetic Satellite Program Office
Office of Space Science and Applications
Washington, D. C.

MAY 1970
RECEIVED
NASA STI FACILITY
INPUT BRANCH

RESEARCH TRIANGLE PARK, NORTH CAROLINA 27709

PRECEDING PAGE BLANK NOT FILMED.

FOREWORD

This report was prepared for the National Aeronautics and Space Administration by the Research Triangle Institute under contract NASW-1909. J. D. Rosenberg, Director of the Geodetic Satellite Program, acted as NASA coordinator. J. T. McGoogan and H. R. Stanley, of NASA Wallops Station, also contributed to the study.

The study was performed in the Engineering and Environmental Sciences Division of the Institute. L. S. Miller served as project director with assistance from Messrs. E. W. Page and W. H. Ruedger. Professors W. A. Flood and N. H. Huang of the North Carolina State University at Raleigh served as consultants and contributed to this report.

ABSTRACT

This report presents the results of an eight-month study of signal processing techniques applicable to the Geodetic Satellite Altimeter program. The first subject treated is the analysis of random errors in the altitude measurement process which arise from signal fluctuations and receiver noise. Results are presented based on both theoretical analyses and computer simulation of the altimeter concept. Characteristics of the electromagnetic energy scattered from the ocean-surface are then discussed from the standpoint of identifying statistical properties of the altimeter signal and for identifying measurement biases that may arise in the scattering process. The report concludes with a discussion of the presently known oceanographic factors pertaining to the scattering problem.

CONTENTS

		Page
FOREWORD		ii
ABSTRACT		iii
Section		
1	INTRODUCTION AND SUMMARY OF RESULTS	1-1
	1.1 Study Objectives	1-1
	1.2 Conclusions and Recommendations	1-2
2	RADAR SYSTEM STUDY	2-1
	2.1 Background	2-1
	2.2 Description of Present Altimeter Concept	2-1
	2.3 Discussion of Errors in Altitude Measurement Process	2-5
	2.4 Evaluation of Threshold Techniques	2-19
	2.5 Effect of Video Non-Linearity	2-23
	2.6 PRF and Miscellaneous Considerations	2-25
	2.7 Summary	2-26
	References	2-28
3	ALTIMETER SIMULATION MODEL	3-1
	3.1 General Discussion	3-1
	3.2 Mathematical Description	3-4
	References	3-13
4	REVIEW OF ELECTROMAGNETIC SCATTERING FROM ROUGH SURFACES AS RELATED TO THE GEODETIC ALTIMETER	4-1
	4.1 General Discussion	4-1
	4.2 Summary	4-2
	4.3 Radar Backscattering from the Sea	4-3
	4.4 Calculation of the Normal Incidence Backscattering Cross-Section	4-10
	4.5 Coherence of Backscattered Signal	4-13
	4.6 Frequency Dependency	4-15
	4.7 Analysis of Wave Height Effects on the Altimeter Waveforms	4-16
	References	4-19
5	OCEANOGRAPHIC STUDY	5-1
	5.1 Summary and Conclusions	5-1

CONTENTS (Continued)

Section		Page
5.2	Background	5-2
5.3	Equilibrium Range of the Spectrum	5-3
5.4	Slope Spectrum	5-9
5.5	The Relationship Between Mean Squared Slope and Surface Wind Speed	5-10
5.6	Directional Characteristics of Ocean Wave Spectra	5-14
5.7	Theory of Wave Generation by Wind	5-15
5.8	Other Mechanisms of Wave Generation and Modifications	5-18
5.9	Probability Structure of the Ocean Surface	5-21
5.10	Methods of Measuring Directional Spectra and Some Results	5-23
	References	5-32

APPENDICES

Appendix		Page
A	COMPUTER SIMULATION WAVEFORMS	A-1
B	THEORETICAL ALTITUDE ERROR ANALYSIS	B-1
C	OPTIMAL PROCESSING TECHNIQUES	C-1
D	ANALYSIS OF OCEAN SURFACE EFFECTS ON RECEIVED WAVEFORM	D-1

ILLUSTRATIONS

Figure		Page
2-1	Typical Simulated Results of Square-Law and Linear Detector Waveforms for a 50 ns Rectangular Pulse, SNR = ∞	2-3
2-2	Typical Simulated Results of Square-Law and Linear Detector Waveforms for a 50 ns Gaussian Pulse, SNR = ∞	2-4
2-3	Typical Simulated Results of Square-Law and Linear Detector Waveforms for a 50 ns Gaussian Pulse, SNR = 10 db	2-6
2-4	Typical Waveforms Involved in Double-Delay Differencing	2-7
2-5	Final Waveforms for 10 Simulated Cases of Double-Delay Differencing Operations, SNR = ∞	2-8
2-6	Histograms of Pulse-by-Pulse Altitude Jitter, 50 Computed Cases	2-10
2-7	Histograms of Pulse-by-Pulse Altitude Jitter, 50 Computed Cases	2-11
2-8	Comparison of Theoretically Computed and Simulated Altitude Errors Versus SNR	2-13
2-9	Histogram of Pulse-by-Pulse Altitude Jitter, 50 Computed Cases	2-14
2-10	Averaged Waveform for Rectangular Pulse, 50 Cases	2-16
2-11	Averaged Waveform for Gaussian Pulse (Original Computation), 50 Cases	2-17
2-12	Averaged Waveform for Gaussian Pulse (Second Computation), 50 Cases	2-18
2-13	Double-Delay Differencing Output Using 50 Case Averaged Waveform as Input	2-20
2-14	Histogram of Pulse-by-Pulse Altitude Jitter for 50% Threshold	2-21
2-15	Histogram of Pulse-by-Pulse Altitude Jitter for 33% Threshold	2-22
2-16	Histogram of Pulse-by-Pulse Altitude Jitter for 1% Video Non-Linearity	2-24
3-1	Block-Diagram of Computer Simulation	3-2
4-1	Comparison of Measured Height and Slope Distributions with Gaussian Curves	4-17
5-1	Sketch of Elevation (Energy) and Slope Spectral Distributions	5-11
5-2	Two-Dimensional Spectrum	5-28
5-3	Two-Dimensional Spectrum	5-29
5-4	Two-Dimensional Spectrum	5-30

TABLES

Table		Page
2-1	Standard Deviation and Mean of Histogram Data	2-9
2-2	Effect of Simulation Conditions on the Values Shown in Table 2-1	2-12
2-3	Comparison of Altitude Errors, 50 ns Pulse, 1000 Samples	2-26
5-1	Observed Values of Equilibrium Range Constants	5-5
5-2	Some Characteristics of Pierson's (1959) Spectrum	5-7

SECTION 1

INTRODUCTION AND SUMMARY OF RESULTS

1.1 INTRODUCTION

This report presents the results of a study of radar signal processing methods for a geodetic satellite altimeter. The two altimeter precision requirements considered are: 1) maximum radar system errors of one to two meters as required for the GEOS-C program and 2) errors limited to a fraction of a meter as required for Sea-Sat A program. Although the emphasis of this work is on signal processing, it has been necessary to devote a considerable portion of the study effort to oceanographic and electromagnetic scattering considerations.

Section 2 deals with the analysis of errors which arise from measurement noise and signal fluctuations in the radar implementation. Since these error sources are unavoidable in the system, signal processing conditions are discussed which reduce these errors to acceptable values. Results are presented based on a theoretical analysis and on computer simulations of the altimeter system.

Section 3 presents a detailed description of the mathematical techniques used to simulate radar scattering from the sea surface and to model the radar altimeter functions.

Section 4 summarizes the electromagnetic scattering work performed during the study. This subject is of central concern for two reasons: 1) the analysis of radar system errors requires accurate characterization of the scattered signal, and 2) the identification and compensation of any measurement bias arising in the scattering process requires a thorough understanding of the underlying physical mechanisms. The two outstanding problems in these categories are the modeling of wave height effects in the transient region of the altimeter signal and the sensitivity of backscattered power to ocean surface conditions. For an idealized ocean surface, e.g. isotropic, Gaussian height distributions, the problem has been solved. Section 3 of this report considers the effect of more realistic assumptions.

The mathematical results in the previous section require a number of assumptions regarding the ocean surface features. The work reported in Section 5 represents a survey of oceanographic literature pertinent to the electromagnetic scattering problem. The principal topics considered in this

Section are the relationship between mean-square slope of the ocean wave structure and surface wind, and the spectral features of the ocean.

1.2 CONCLUSIONS AND RECOMMENDATIONS

The system analyses conducted during the course of this study indicate that the random errors due to signal fluctuation and receiver noise will result in an altimeter precision on the order of one-half meter for a system within the following characteristics:

Single pulse signal-to-noise ratio	10 to 20 db
Pulse length	50 to 100 ns
Sampling rate	1000 per second

These characteristics are well within the state-of-the-art in radar design. An altimeter can be designed to meet accuracy objectives of the GEOS-C program but particular attention must be given to long-term drift problems.

There are a number of unknowns in the design of an altimeter with an accuracy of a fraction of a meter. One of the most important questions aside from "sea state" bias is the pulse-to-pulse correlation of the altimeter signal. This limits the attainable altimeter accuracy per unit time. Radar reflections from the sea have never been accurately measured under satellite conditions and the GEOS-C satellite is probably the best approach to obtaining this information.

Although the GEOS-C performance can be realized with a conventional pulsed, split-gate, or threshold signal processor, the Sea-Sat A equipment will require more sophistication. The theoretically computed random error for a 50 ns pulse length and for 1000 samples per second is 20 cm. This error can in theory be further reduced through use of shorter pulses, faster pulse rise-time, or more elaborate transmitter waveforms, even if the pessimistic assumption of a one-millisecond signal correlation time is found to apply to satellite data. The results given in this report indicate that systematic errors and equipmental biases will constitute the largest instrumentation error in the Sea-Sat A concept. These non-random errors can arise from effects such as: 1) mean-value shifts in the altitude data as a function of signal statistics or signal-to-noise ratio, 2) environmental or temporal drift characteristics of the satellite equipment, or 3) unrecognized processor non-linearities. Because of the severity of these problems it is recommended that a wide range of radar techniques be investigated for Sea-Sat A. It is further recommended that future radar altimeter research emphasize the Sea-Sat A requirements, since added knowledge of problem

areas and techniques required for the Sea-Sat A system may lead to a more evolutionary concept for GEOS-C. Until the first satellite altimeter is in operation, many elements of the altimeter function will remain speculative.

In regard to electromagnetic scattering, it is found that the radar cross-section σ_o can be related to mean squared slopes of an isotropic sea surface. For non-isotropic ocean surface conditions the relationship is more complex. Derivation of the functional relationships through a theoretical electromagnetic approach appears unrealizable at this time because of the extreme difficulty in obtaining accurate high frequency ocean-wave data. Equivalently, the ocean surface autocorrelation function cannot be measured with the required accuracy using existing methods. An empirical approach is therefore recommended for obtaining normal incidence data in which actual radar data is correlated with ground truth information under varying sea surface and meteorological conditions. Because of the normal incidence geometry problems and altitude limitation associated with conventional aircraft measurements, extraction of such data from the GEOS-C experiment is strongly recommended.

For the investigation of "sea state" effects on the altimeter signal, acquisition of near-surface (short pulse) radar and laser profilometer data is recommended. Such data would constitute a basis from which to assess the effects of the approximations and assumptions in the electromagnetic models of sea-state bias.

The principal conclusion of the oceanographic study is that mathematical arguments require the two-dimensional power spectrum to exhibit 180° symmetry. At present, there is no single technique which will provide a two-dimensional spectrum of the accuracy and spatial resolution needed for electromagnetic scattering investigations.

SECTION 2

RADAR SYSTEM STUDY

2.1 BACKGROUND

This section presents the results of the study pertaining to radar signal processing. A number of important error sources have been investigated during the course of the program. These include: errors arising from the signal fluctuations inherent in planetary or ocean scattering*, errors resulting from the limited number of samples available per unit time, and errors caused by thermal noise and processor non-linearities. The importance of these errors is assessed relative to the two altimeter precision categories and to techniques for minimizing and/or compensating for these errors.

This section is organized as follows: As a means of establishing concepts and nomenclature, a general description of the altimeter techniques under consideration is given. Computed waveforms are shown to clarify the concepts. This discussion is followed by a presentation of the principal results of the radar altimeter study. Error sources and parametric effects are investigated using theoretical results and computer simulations. The section concludes with a consideration of general system characteristics and a review of potential alterations to the radar system. Computational aspects of the simulation and radar characteristics which are heavily influenced by either electromagnetic or oceanographic considerations are considered in later sections.

2.2 DESCRIPTION OF THE PRESENT ALTIMETER CONCEPT

A number of organizations have considered the problems of measurement of satellite altitudes to the precision required in the geodetic investigation[1-7]. The more conventional system characteristics such as transmitted waveform, power level, sensitivity, bandwidth, and antenna gain have been covered in the cited references and will not be discussed here. As presently envisioned, the first generation altimeter will consist of an X-band pulsed radar with provisions for measurement of time-of-arrival of the received signal. The development of

---

* The term "self noise" is commonly used in radar astronomy to describe this effect.

such a system differs in several important areas from the design of conventional radar systems. Attainment of the desired accuracies will require optimum signal processing and timing techniques, and knowledge of the effects of oceanographic features on the scattered signal.

Some of the technical problems that must be considered in developing satellite equipment are: 1) the limited space, power, and weight available, 2) the nature of ocean backscattered signal, and 3) satellite dynamics. As discussed more fully in Section 4, return from the ocean surface arises from many discrete regions. The signal is dispersed in both time and frequency. For the assumed satellite conditions, a 50 nanosecond (ns) transmitted pulse will give rise to a received signal with a time spread of 2.6 microseconds for a 3 degree antenna beamwidth. The signal will fluctuate in amplitude with characteristics similar to signals received over a rapidly fading channel. These signal characteristics can be seen by an examination of the receiver waveforms, shown in Fig. 2.1, which were obtained as a by-product of the simulation study. Figure 2.1 shows ten typical received waveforms corresponding to the transmission of a 50 ns rectangular pulse scattered from the ocean's surface and received by a very wideband receiver. Waveforms with the vertical scale labeled E represent the output of a linear envelope detector and those labeled E^2 represent the output of a square-law detector. The horizontal scale shows relative time in nanoseconds, with 25 ns corresponding to the instant at which one-half the pulse envelope arrives on the sea surface. These computed waveforms correspond to independent samples. For a simulated radar inter-pulse period less than the correlation time, the waveforms would show evolutionary changes. Referring to Fig. 2.1, except for the transient region in which the entire pulse is not incident on the surface, the sea return signals are much like samples of receiver noise.

Simulated waveforms are shown in Fig. 2.2 corresponding to a Gaussian shaped pulse that is 50 ns wide at the e^{-1} points. The horizontal scale shown in this case is based upon the center of the pulse arriving at the ocean surface at 51 ns. The same distribution of reflecting area was assumed in the computations used in Figs. 2.1 and 2.2; the Gaussian returns therefore appear as smoothed versions of the rectangular data. The Gaussian envelope is considered indicative of matched filter IF characteristics. Note that the Gaussian results demonstrate that filtered waveforms need not be sampled rapidly for good

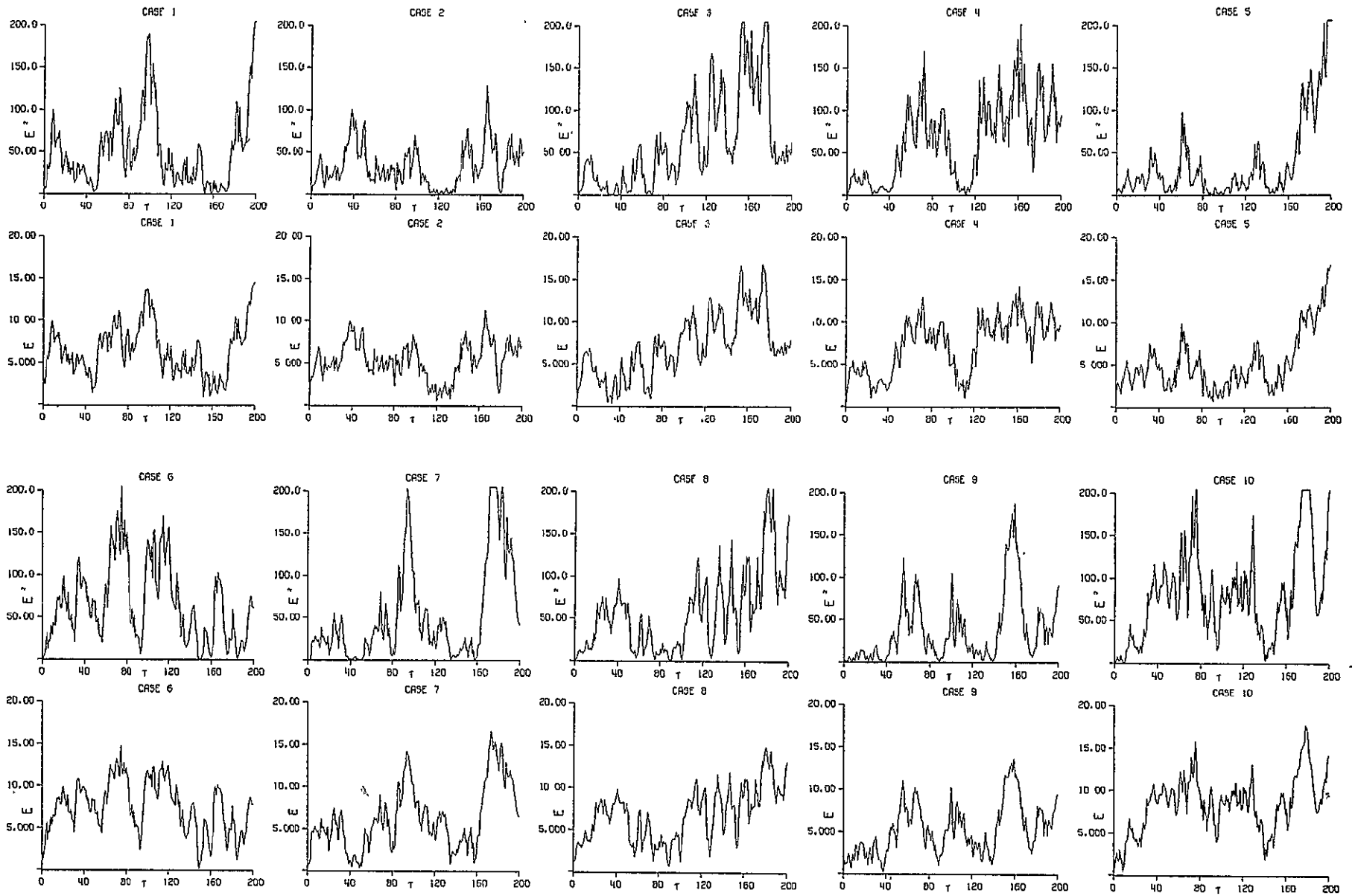

Fig. 2.1. Typical Simulated Results of Square-Law and Linear Detector Waveforms for a 50 ns Rectangular Pulse, SNR = ∞.

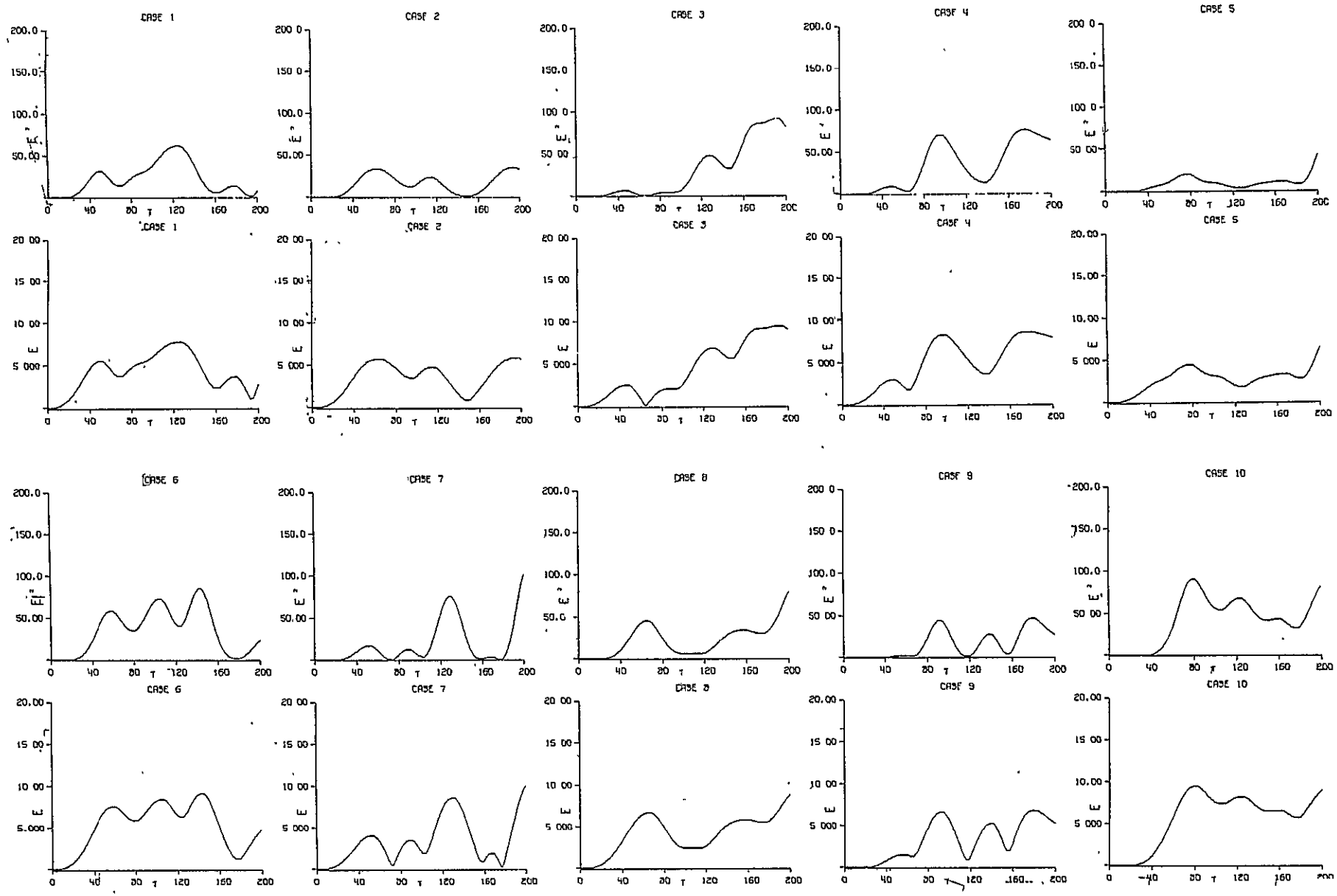

Fig. 2.2. Typical Simulated Results of Square-Law and Linear Detector Waveforms for a 50 ns Gaussian Pulse, SNR = ∞.

reconstruction of the waveform. Also, it is noted that for a system containing an AGC response-time on the order of one second, some of the received waveforms will contain very little average energy over a 200 ns time interval. Case 5 of Fig. 2.2 demonstrates the fact that the instantaneous altitude error can be several times the pulse length for a matched filter IF regardless of the measurement scheme used. Some of the waveforms shown in Fig. 2.1 exhibit a saturation effect. This is not a result of the simulation program; is is simply due to the scale size used in the figure.

Figure 2.3 shows the effect of receiver noise on the altimeter waveforms. The same signal characteristics were used as in Fig. 2.2, and a comparison of Figs. 2.2 and 2.3 shows the effects of a 10 db signal-to-noise ratio (SNR) on the waveforms. The fine structure in the noise is due to the finite slope of the noise spectrum with frequency.

The double-delay differencing type of altitude processor consists of two-stage signal differencing with a delayed and inverted replica of the original signal[1]. The sample waveforms involved in the double-delay differencing operation are shown in Fig. 2.4 (the signal waveform previously shown as Case 1, Fig. 2.3 was used). Figure 2.5 shows typical waveforms at the output of the double-delay differencer for ten individual cases (for the noise free Gaussian signal). A comparison of Figs. 2.4 and 2.5 shows that individual cases depart drastically from the results that would be obtained by using an idealized ramp signal. The most significant feature in Figs. 2.4 and 2.5 is that multiple zero-crossings are present. Because of these ambiguities, the double-delay technique would not be suitable in the altimeter without the addition of a threshold circuit or a closed-loop implementation.

Additional examples of simulated waveforms are contained in Appendix A. The quantitative results of the radar system study are discussed in the next section.

2.3 DISCUSSION OF ERRORS IN THE ALTITUDE MEASUREMENT PROCESS

The two principal methods of altitude extraction examined in this report are: 1) double-delay differencing and 2) thresholding. The investigation was limited to these techniques, because the General Electric Company had concurrently investigated the split-gate technique[4]. The results given below apply to both open and closed-loop systems.

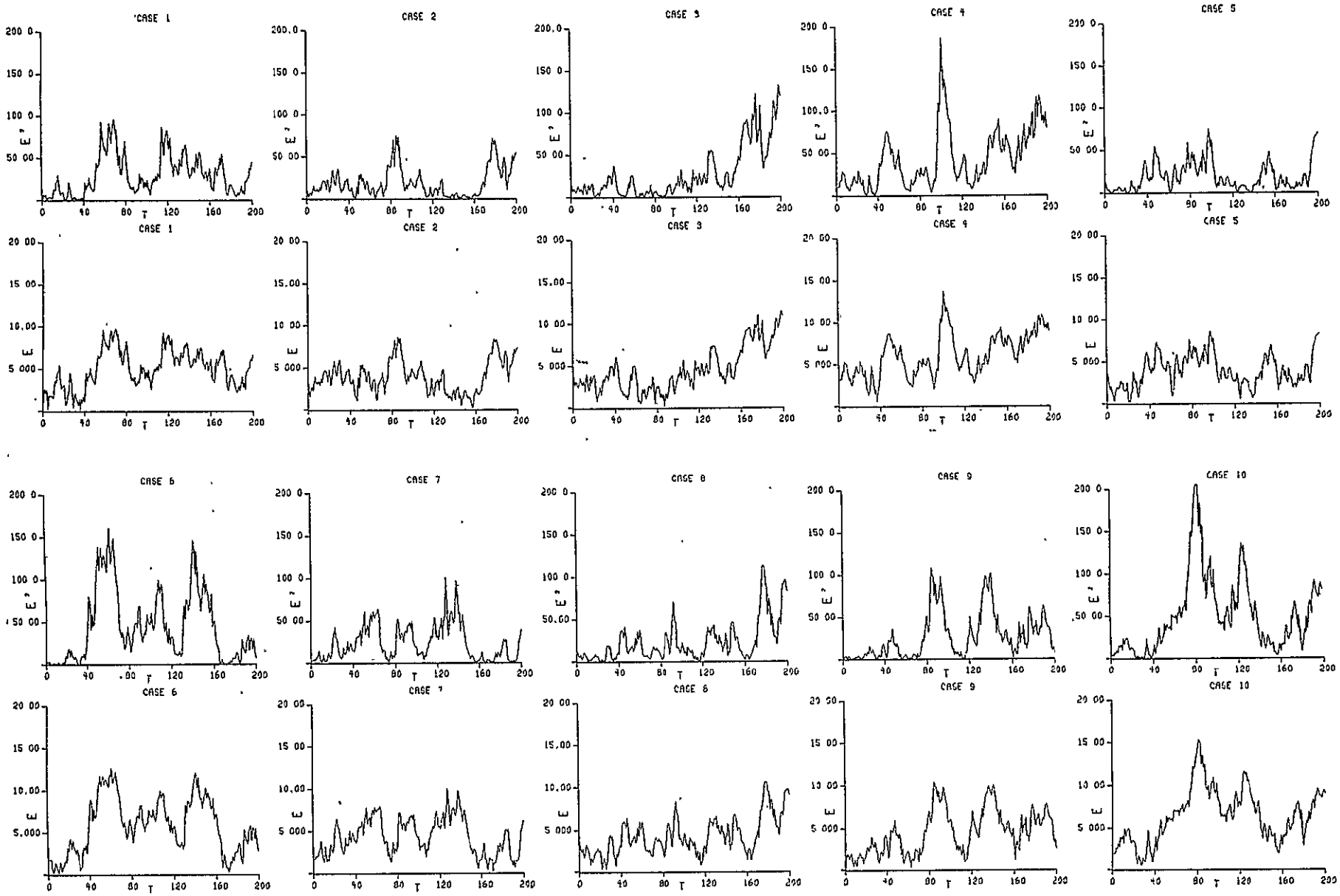

Fig. 2.3. Typical Simulated Results of Square Law and Linear Detector Waveforms for a 50ns Gaussian Pulse, SNR= 10db

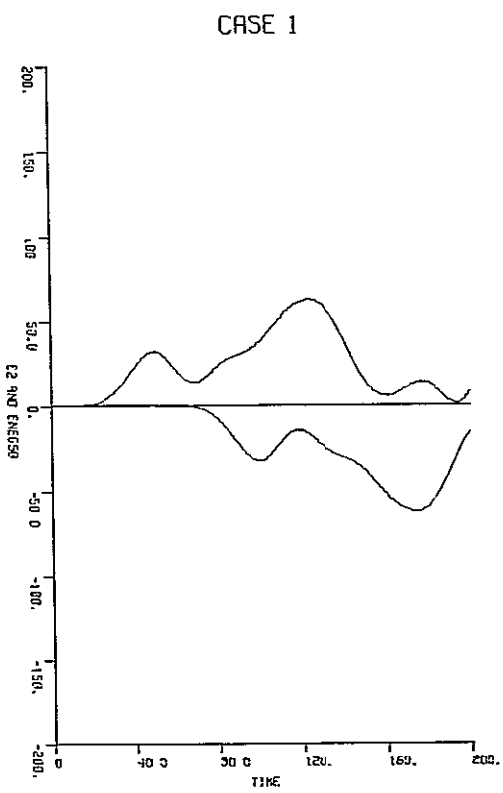

1st Difference

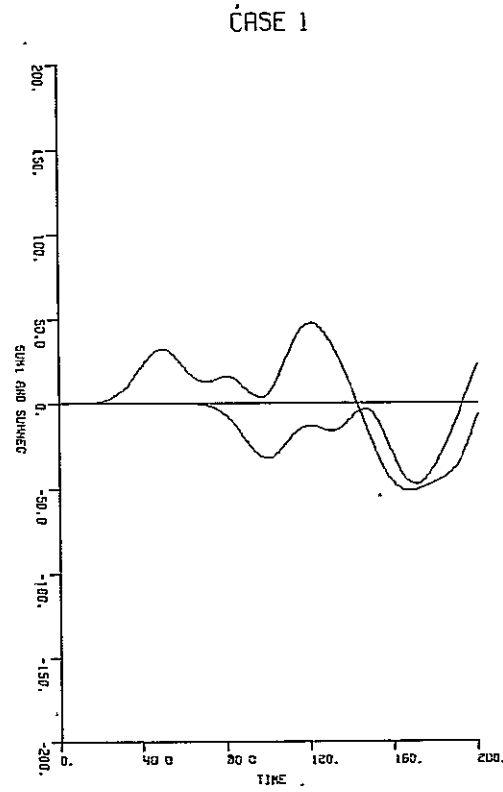

2nd Difference

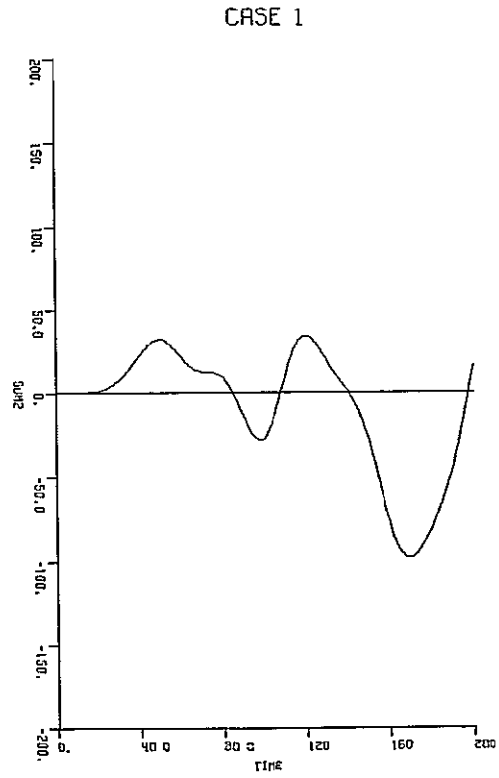

Final Waveform

Fig. 2.4. Typical Waveforms Involved In Double Delay Differencing

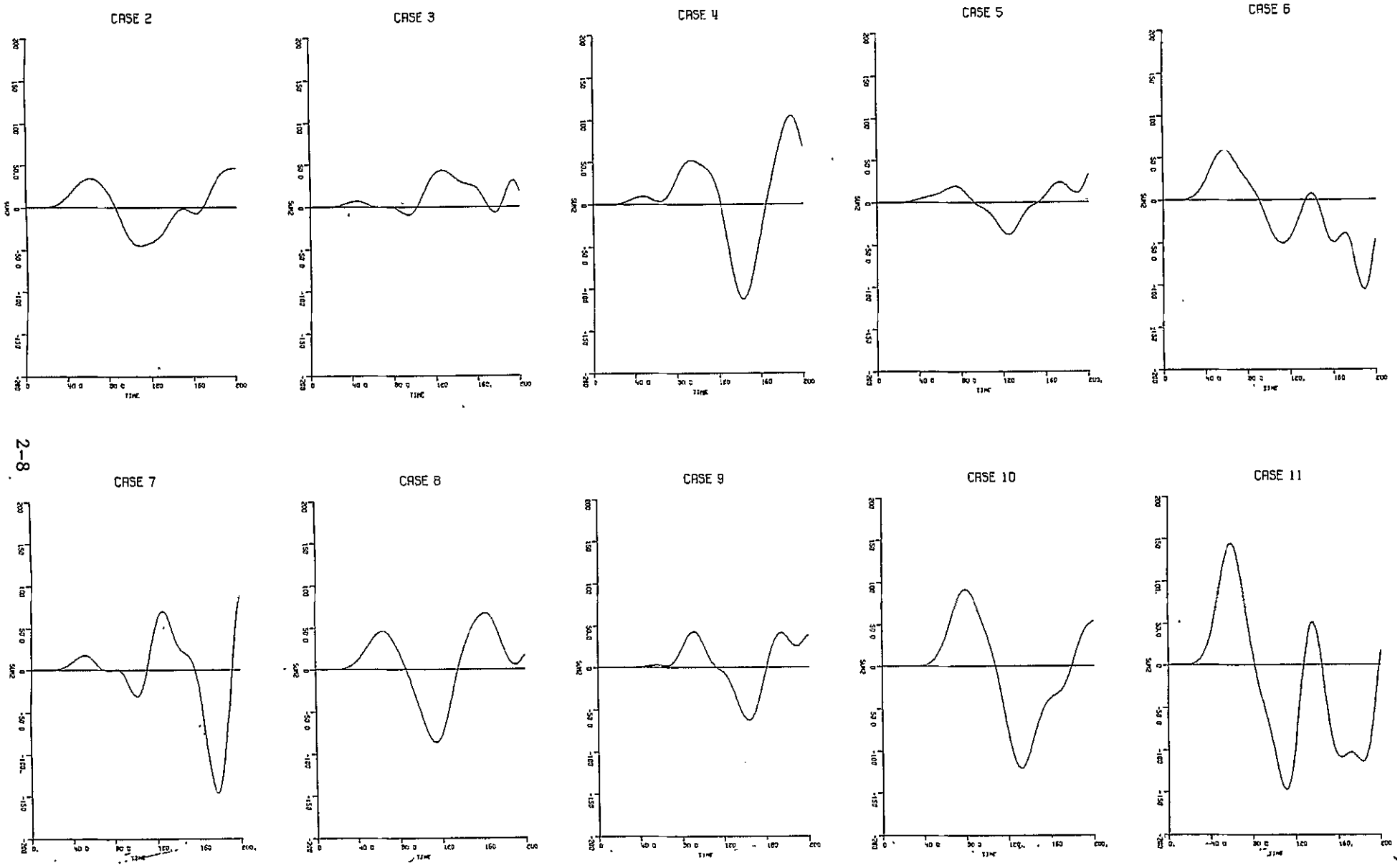

Fig. 2.5. Final Waveforms for 10 Simulated Cases of Double Delay Differencing Operations, SNR = ∞.

Histograms of the individual altitude errors at the output of a double-delay differencer were obtained through digital simulation for fifty independent cases. A 50 ns Gaussian shaped pulse was used; the delay interval for the double-delay difference was 50 ns. Figures 2.6 and 2.7 show the histogram data for signal-to-noise levels of ∞, 30, 20, and 10 db. The standard deviation σ and mean crossings μ derived from the histogram data are shown in Table I.

The altitude error $\hat{\sigma}_s$ to be expected for a 1000 sample average also was obtained from the histogram standard deviation σ_s through the equation

$$\hat{\sigma}_s = 1.62 \frac{ct}{2\sqrt{n}} \sigma_s$$

where n is the number of samples, c is the propagation velocity, t is the unit of time of σ_s, and the factor of 1.62 is the conversion of pulse length used in the simulation (e^{-1} points) to half-power pulse length.

Table 2-1

Standard Deviation and Mean of Histogram Data

SNR	Std. Dev. (σ_s) in ns 50 cases	$\hat{\sigma}_s$ in meters 1000 cases	Mean (μ) in ns
∞	18	.14	94.6
30 db	18	.14	96
20 db	17.2	.13	89
10 db	18.4	.14	68

Table I shows the altitude variance to be largely independent of receiver noise. The indicated altitude uncertainty $\hat{\sigma}_s$ converts to a (two-way) altitude error of approximately 0.14 meters for 1000 samples.

A theoretical analysis of the altitude error characteristic is given in Appendix B. This analysis assumes that correlation exists within the detected altimeter signal (i.e. matched filter IF) and that a double-delay differencer type of altitude measurement is used. The altitude error σ_a in meters is found to be

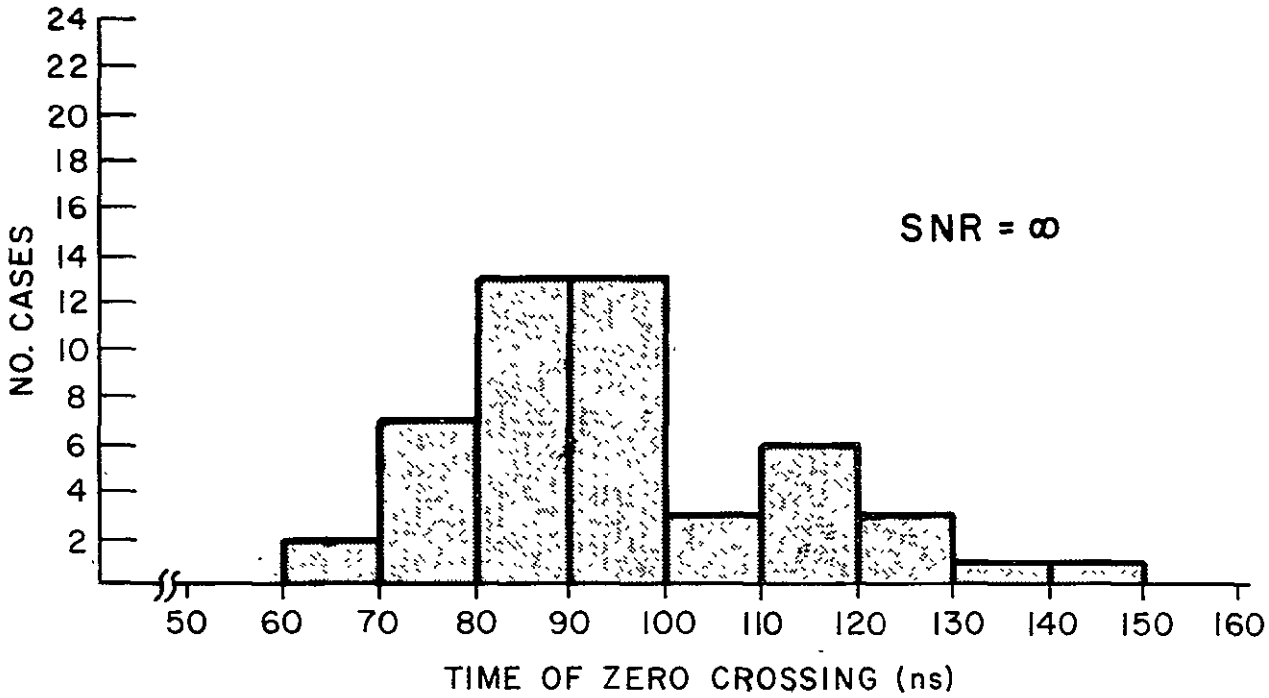

FIG 6A

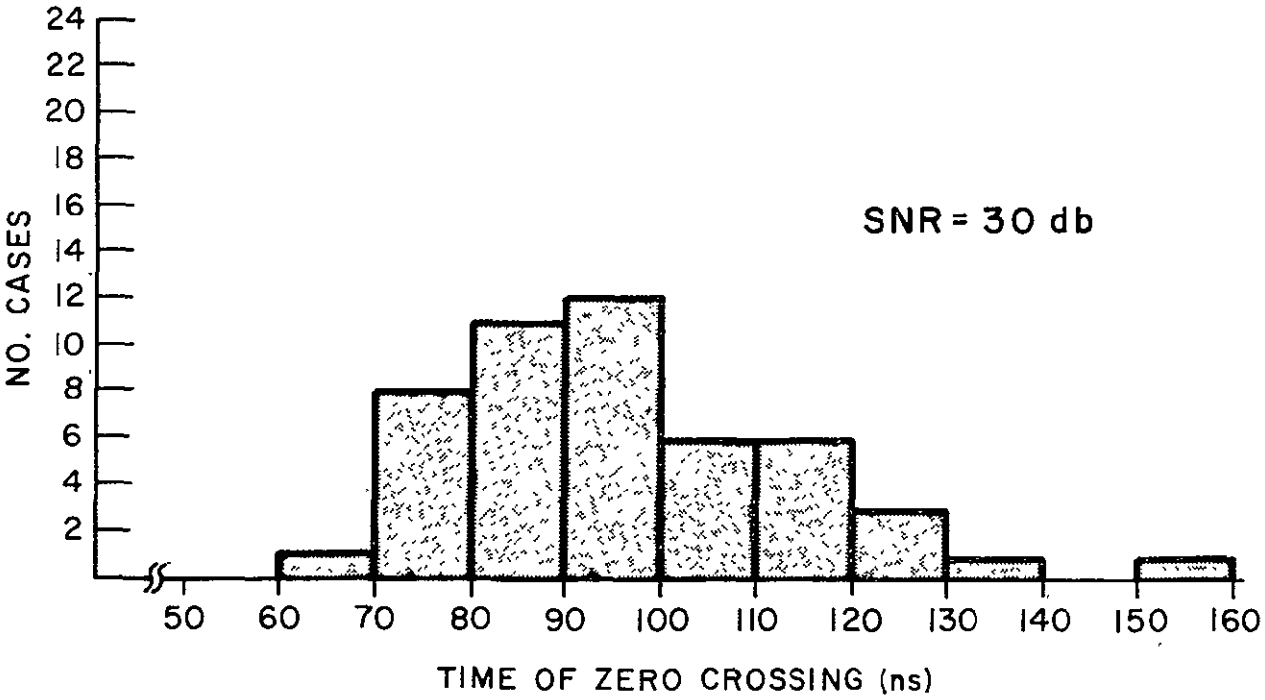

FIG 6B

Fig. 2.6. Histograms of Pulse-by-Pulse Altitude Jitter, 50 Computed Cases

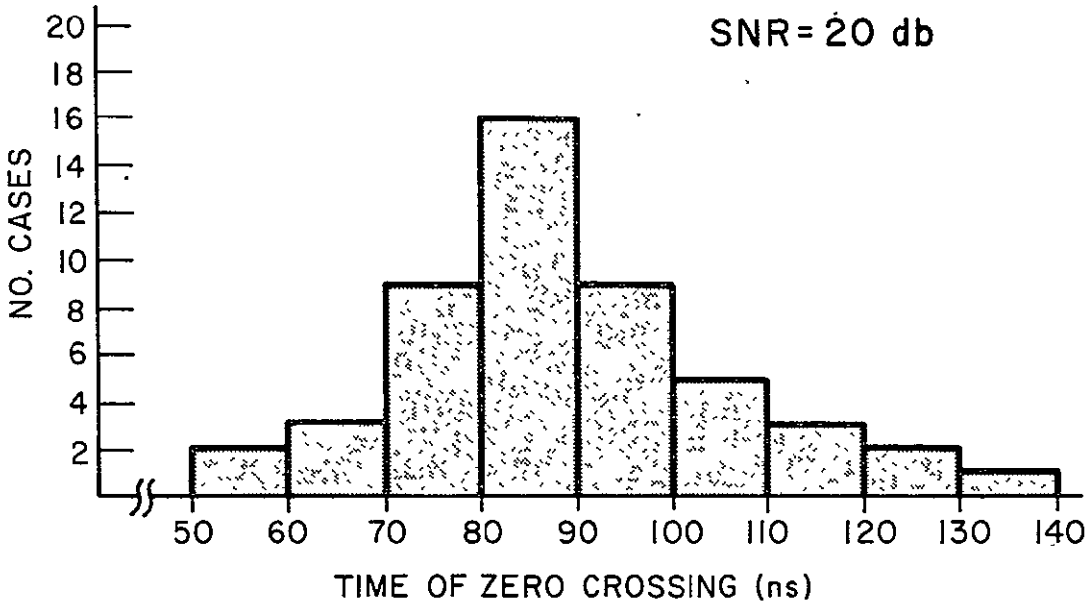

FIG. 7A

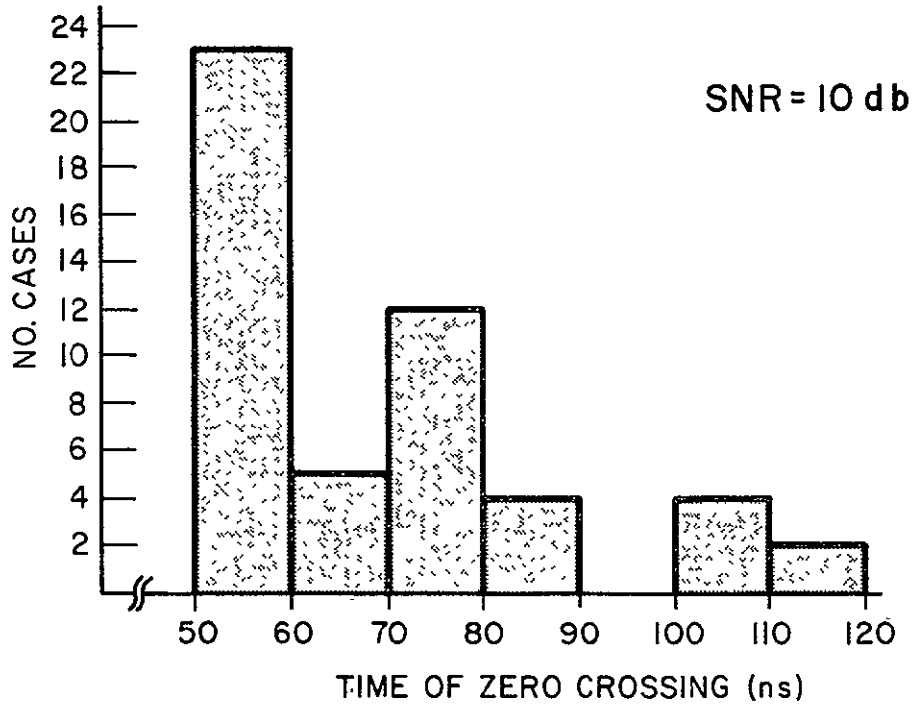

FIG. 7B

Fig. 2.7. Histograms of Pulse-by Pulse Altitude Jitter, 50 Computed Cases

$$\sigma_a = \frac{.15T}{\sqrt{n}} \sqrt{.68 + 9.5\ (SNR)^{-1} + 7.9\ (SNR)^{-2}}$$

where T is the pulse length in nanoseconds (at the half-power point) and n is the number of independent samples. A comparison of theoretically computed and simulated altimeter errors (arising from signal fluctuations and receiver noise) is shown in Fig. 2.8. The two results are in good agreement.

The mean-value figures given in Table I show considerable change with noise level. This fluctuation may be caused by two effects: 1) variation due to the limited sample size present and 2) variations caused by any differences in the spectral characteristics of the signal and receiver noise. To determine which effect was dominant, a series of computer runs were made under varying conditions. Figure 2.9A shows the histogram results obtained for a 20 db SNR and for new sets of random numbers used in the signal and noise simulations. Figure 2.9B shows histogram results for 20 db SNR using a narrower noise bandwidth. These results are summarized in Table II.

Table 2-2

Effect of Simulation Conditions on the Values Shown in Table I

(SNR = 20 db)

Computation	Std. Dev. (σ_s) in ns 50 cases	$\hat{\sigma}_a$ in meters 1000 cases	Mean (μ) in ns
Original	17.2	.13	89
New random numbers	22.8	.18	96
Reduced noise bandwidth	17.9	.14	91

The mean and variance are both seen to be more dependent on initial conditions than on noise bandwidth. A much larger sample size (~1000) is therefore required to provide acceptable accuracy in the histogram data. Computations of such magnitude were outside the scope of this contract and can be performed more efficiently using analog techniques.

The fact that the mean crossing point is sensitive to receiver noise characteristics may be seen from examining the theoretical relationship for the probability of a zero-crossing $p(\tau)$. For Gaussian processes which start at $\tau = 0$,

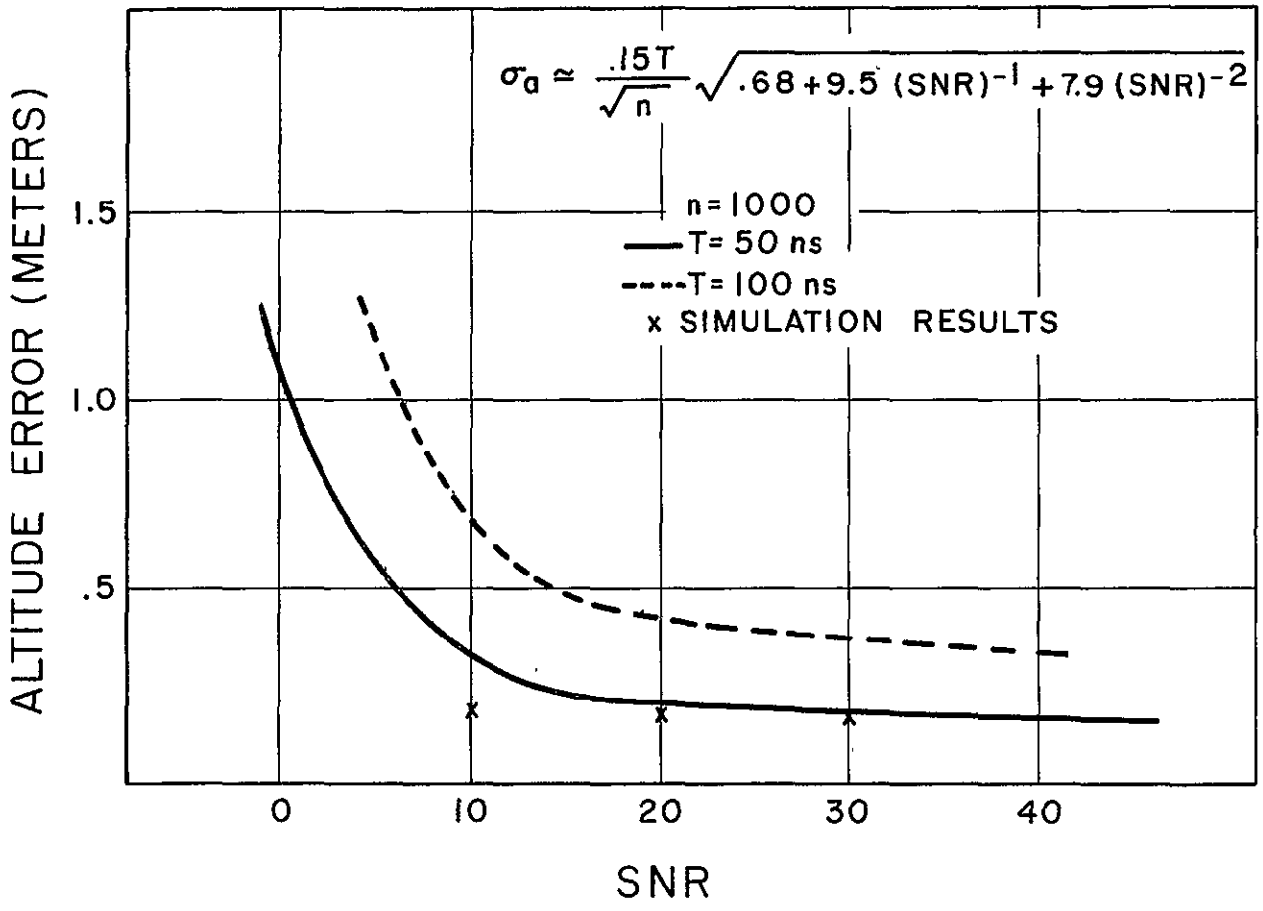

Fig. 2.8. Comparison of Theoretically Computed and Simulated Altitude Errors Versus SNR

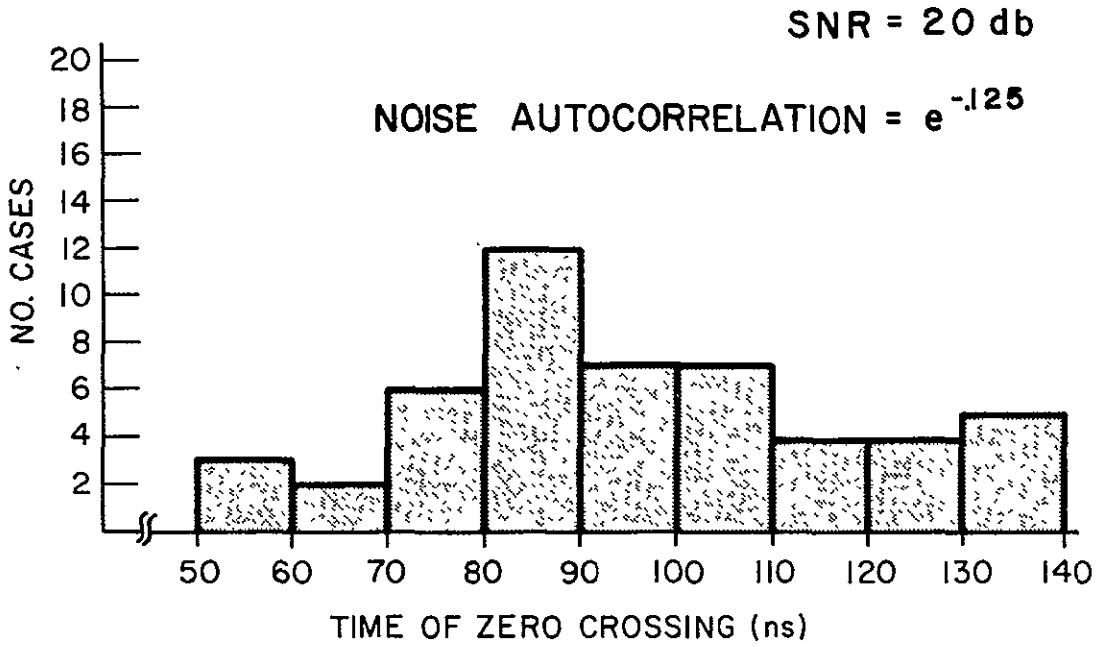

FIG. 9A

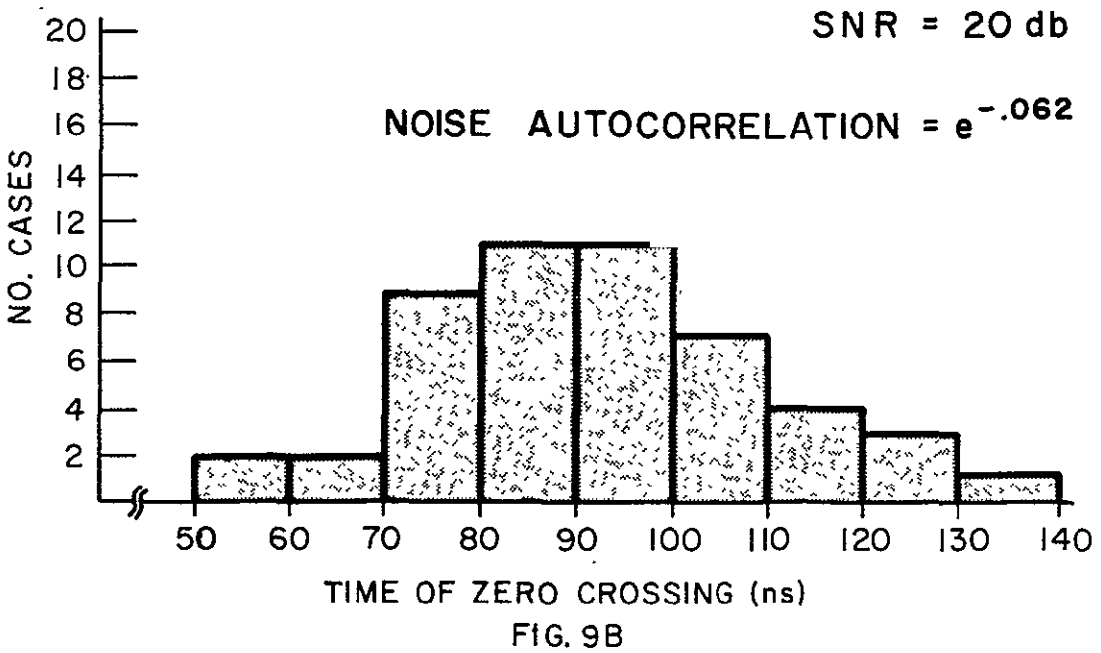

FIG. 9B

Fig. 2.9. Histogram of Pulse-By-Pulse Altitude Jitter, 50 Computed Cases

$\rho(\tau)$ is given by[8],

$$\rho(\tau) = \frac{1}{\pi}\sqrt{\frac{2[R(o) - R(\tau)]}{R(o)}}$$

in which $R(\tau)$ is the correlation coefficient. For additive (uncorrelated) signal and noise this expression becomes

$$\rho(\tau) = \frac{1}{\pi}\sqrt{2\left[1 - \frac{R_s(\tau) + R_n(\tau)}{R_s(o) + R_n(o)}\right]}$$

where the subscripts s and n refer to signal and noise. Assuming exponential correlation functions of the form

$$e^{-\alpha_s t} \quad \text{and} \quad e^{-\alpha_n t}$$

for $\alpha_n > \alpha_s$, the numerator of the square root term $e^{-\alpha_s t} + e^{-\alpha_n t}$ decays faster than for $\alpha_n = \alpha_s$ and the zero crossing probability occurs earlier in time.

Any shift in the mean value of the altitude indication constitutes an important source of error in the altimeter. The above results, although qualitative because of the sample-size limitations, indicate that a bias will exist that is a function of SNR. A similar effect has been noted in the split-gate tracker when a dc restore circuit is not used[4].

Neglecting wave-height effects, the integration of a large number of radar returns from the sea-surface should produce a "ramp-like" signal since the area exposed during the early portions of the pulse illumination will increase linearly. A presentation that is proportional to signal power (i.e. a square-law detector) will therefore exhibit this linear dependency. These computed waveforms for both linear and square-law detectors are shown in Figs. 2.10-2.12. Figure 2.10 shows the waveform obtained by averaging the 50 rectangular pulse cases (see Fig. 2.1). Confidence bounds may be estimated for these data by noting that for a Rayleigh distribution (linear detector case) the variance is equal to $(1 - \frac{\pi}{4})$ times the mean value μ, and for an exponential distribution (square-law detector) the

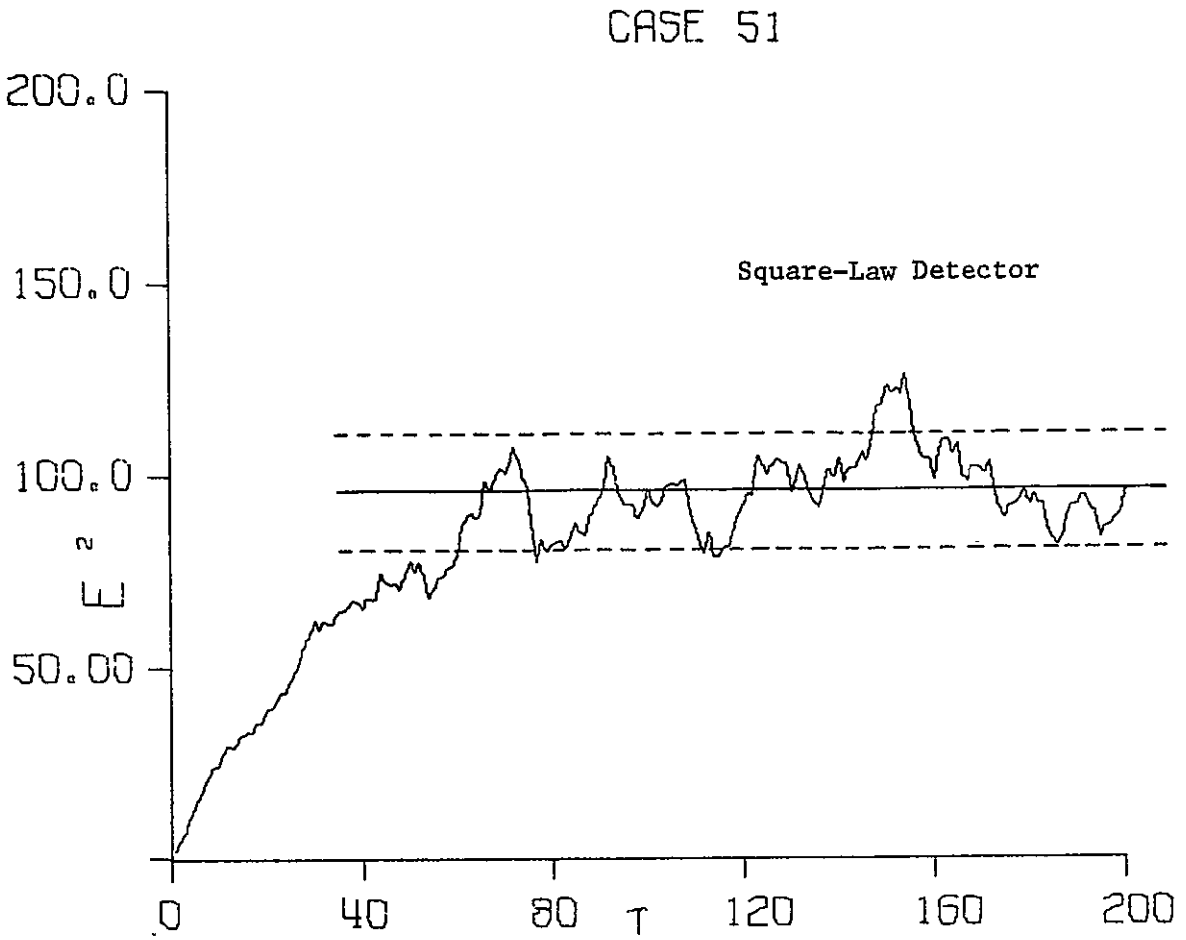

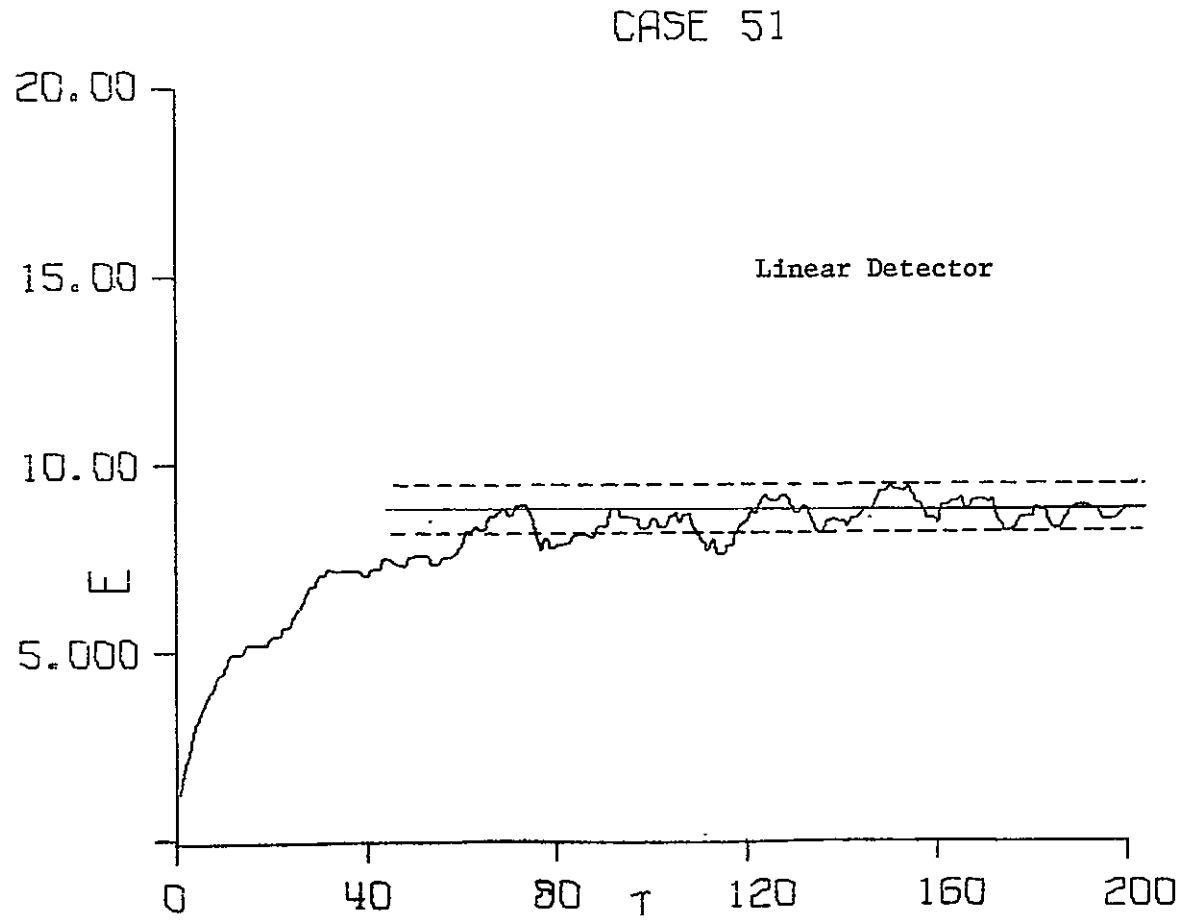

Fig. 2.10. Averaged Waveform for Rectangular Pulse, 50 Cases

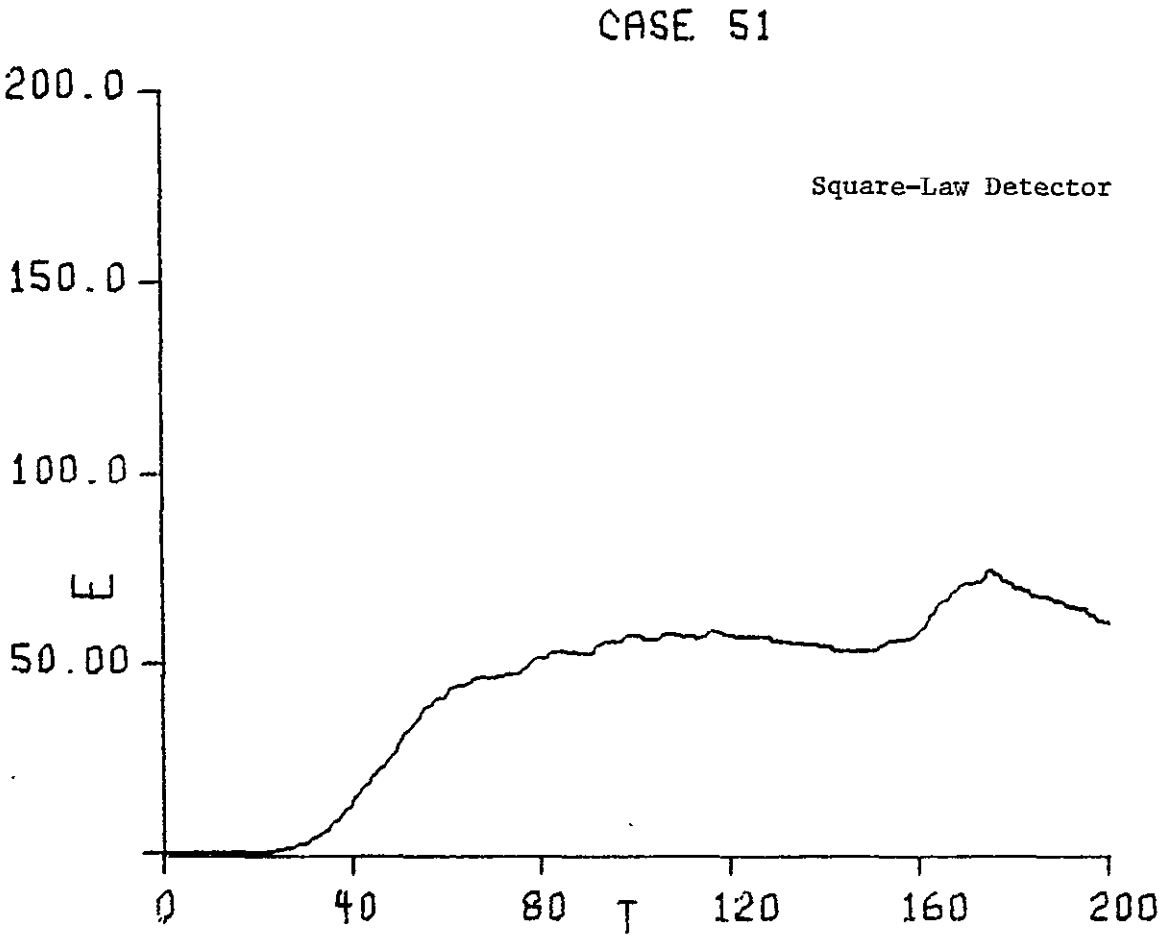

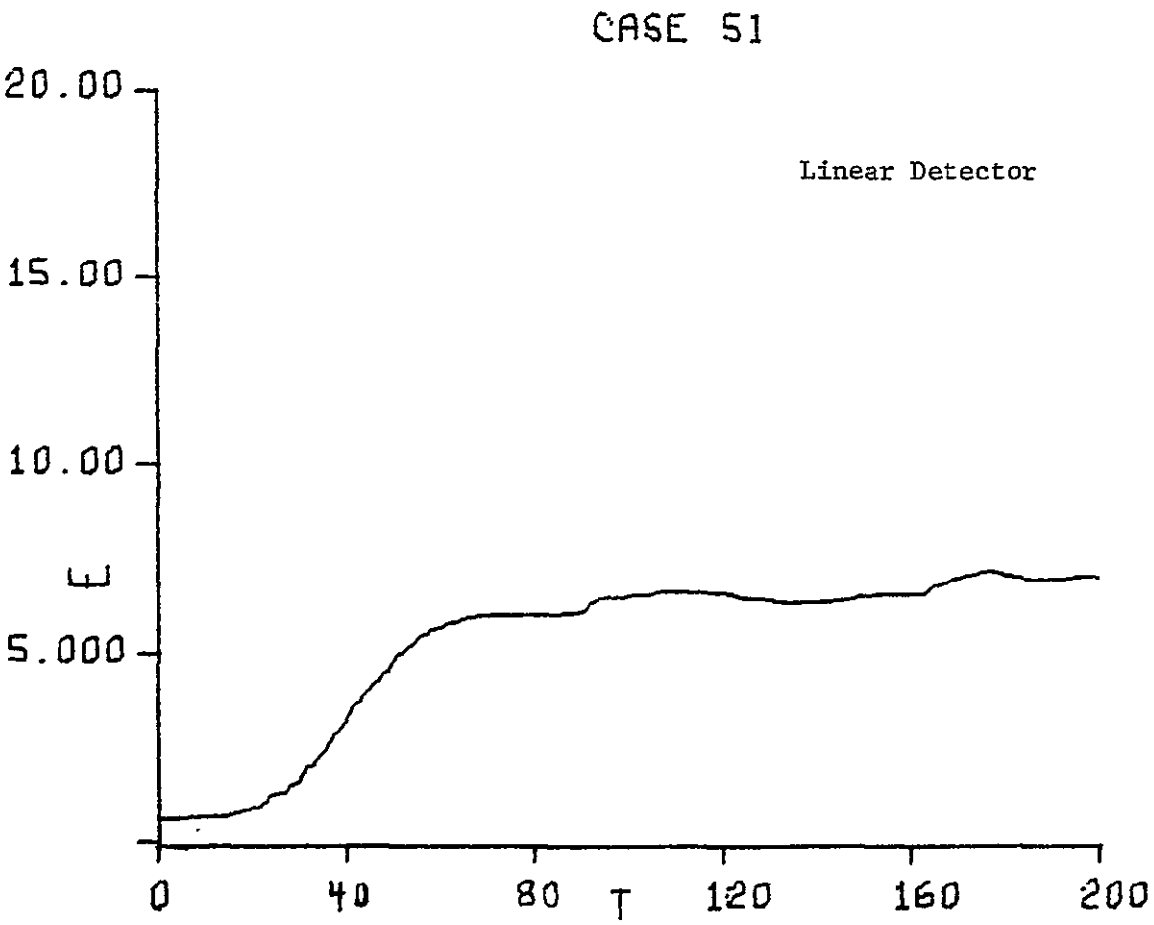

Fig. 2.11. Averaged Waveform for Gaussian Pulse (Original Computation), 50 Cases

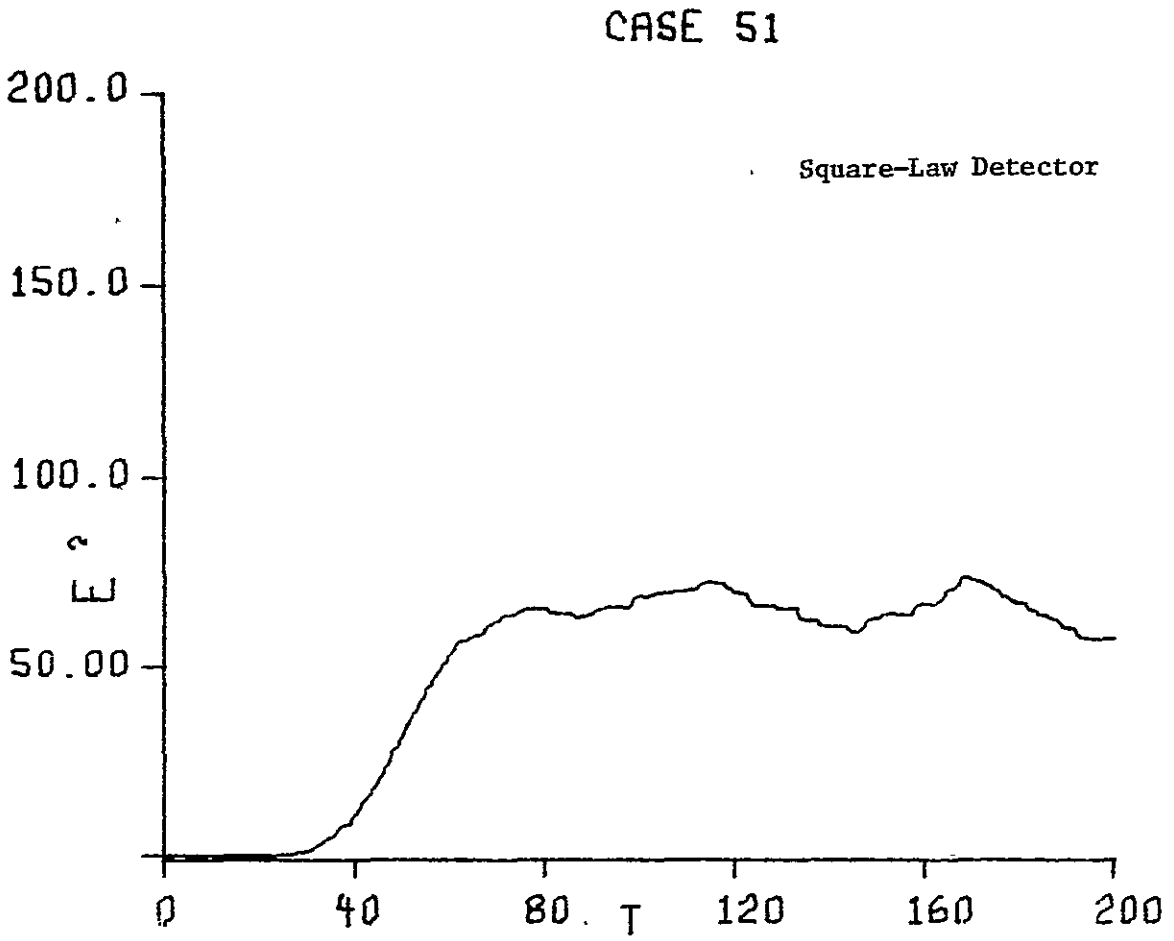

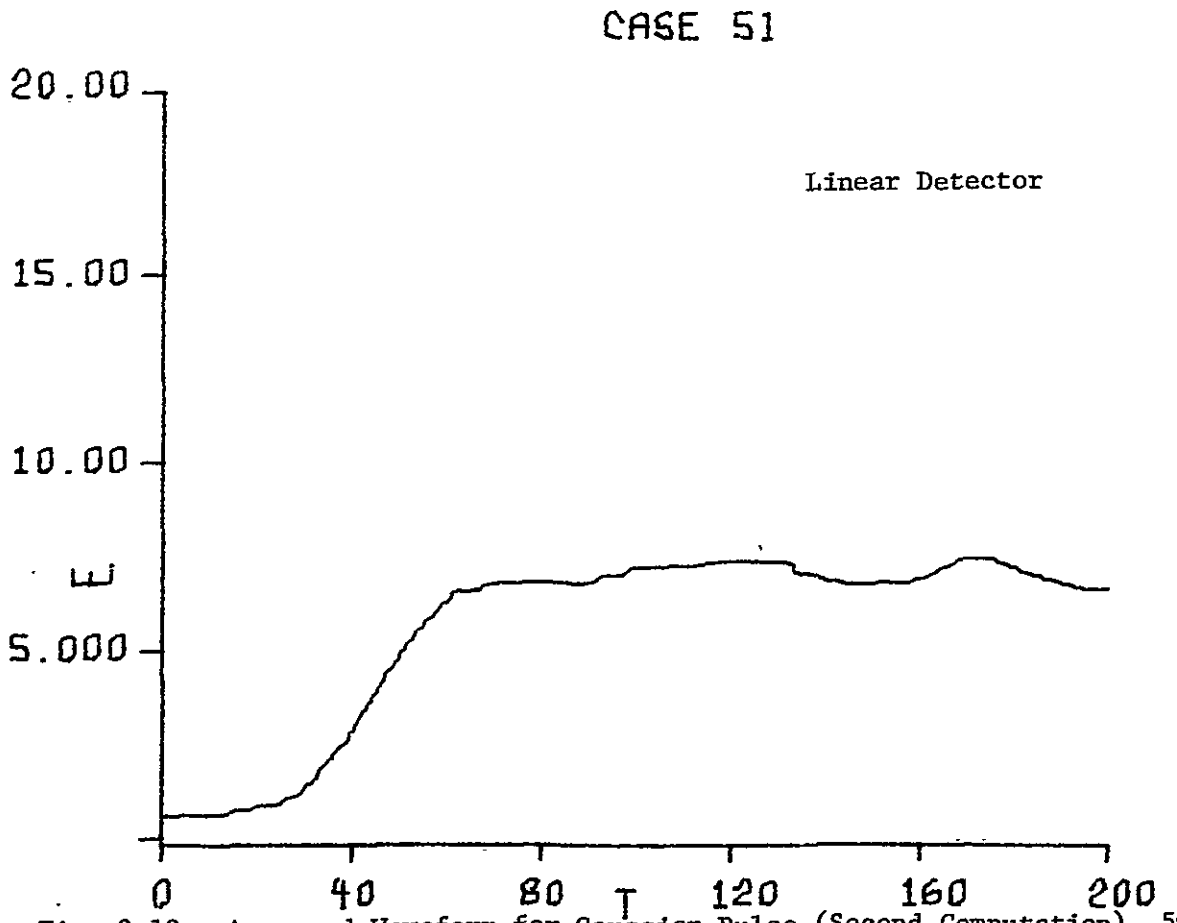

Fig. 2.12. Averaged Waveform for Gaussian Pulse (Second Computation), 50 Cases

variance is twice the square of the mean value. Therefore, standard deviation for the 50 sample waveform is

$$\sigma = \sqrt{\frac{1}{50}\left(1 - \frac{\pi}{4}\right)}\ \mu \qquad \text{Rayleigh}$$

$$\sigma = \mu\sqrt{\frac{2}{50}} \qquad \text{Exponential.}$$

These one-sigma bounds are shown as dotted lines in Fig. 2.10. Figures 2.11 and 2.12 show the average waveforms for two simulation cases of 50 samples each, using Gaussian shaped pulses.

Estimates of the errors to be encounterd in altimeter operation have been made using mean value waveforms as in Fig. 2.12. One may argue that the averaging process can be performed prior to double-delay differencing and certainly the mathematical and conceptual simplifications are appealing. The result of double-delay differencing of an average of 50 waveforms is shown in Fig. 2.13. The zero crossing for this average waveform occurs at 99 nanoseconds. The results of averaging single pulse errors (Table I) indicate that the mean zero crossing occurred at 94.6 nanoseconds. Significant differences can therefore exist between the two computations, and analyses based upon an equivalence between the two should be treated with caution.

2.4 EVALUATION OF THRESHOLD TECHNIQUES

Simulation results are shown in Figs. 2.14 and 2.15 for a threshold type of altitude measurement. The threshold levels used in Figs. 2.14 and 2.15 were, respectively, 50 percent and 33 percent of the maximum value of the average signal. These results contain several interesting features. The 33 percent threshold level (Fig. 2.15) results in an altitude standard deviation of 18 ns (50 cases), which is exactly the result obtained using a double-delay differencer (c.f. Fig. 2.6A). The 50 percent threshold was found to produce a larger standard deviation (25 ns) because of occasional values with large time deviation (the tail shown in the histogram). The fact that some of the threshold crossings occur long after the leading edge can be seen by examination of the waveform data in Case 5 of Fig. 2.2. This particular waveform crosses about 140 ns late. The data

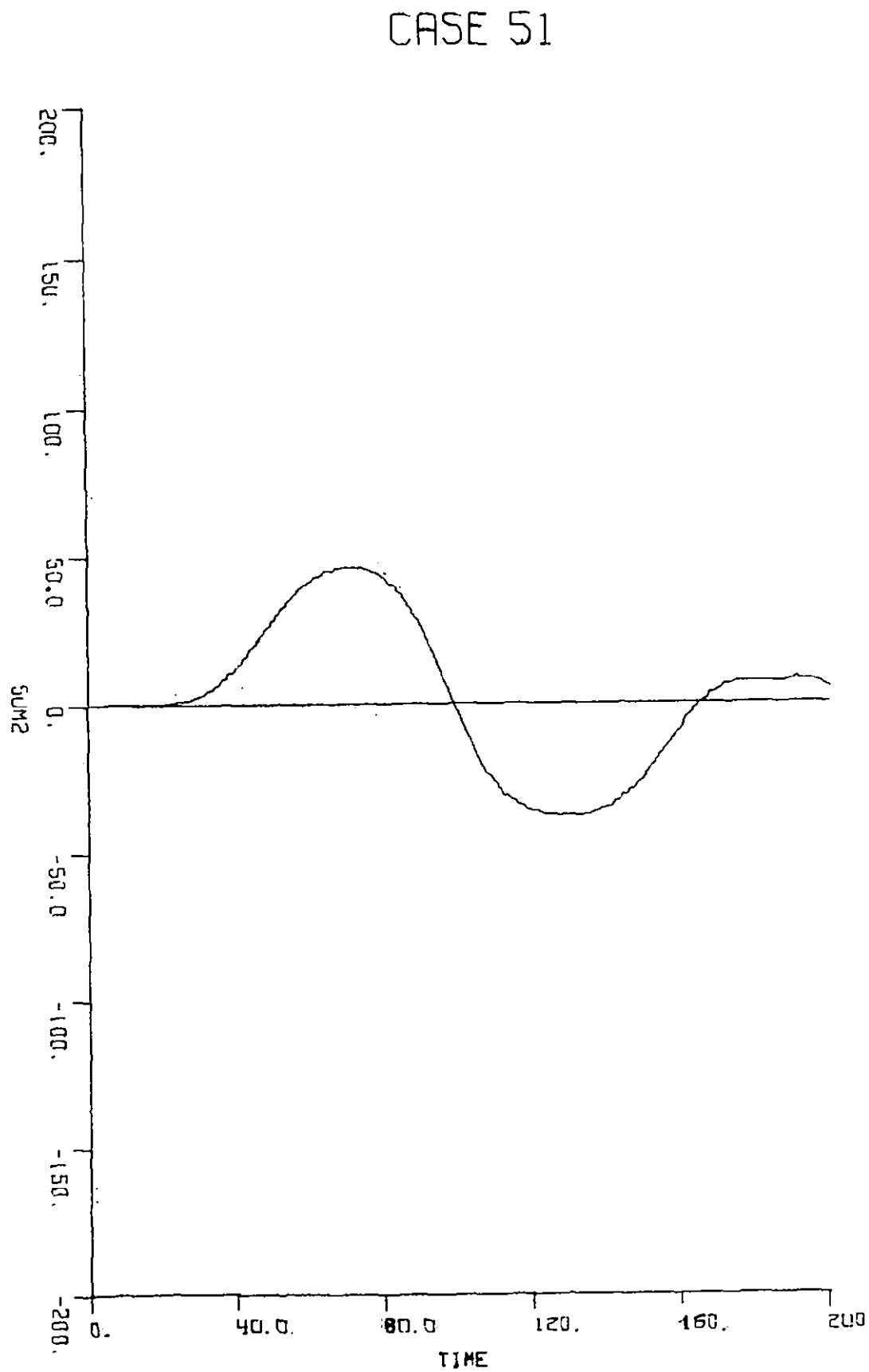

Fig. 2.13. Double-Delay Differencing Output
Using 50 Case Averaged Waveform as Input

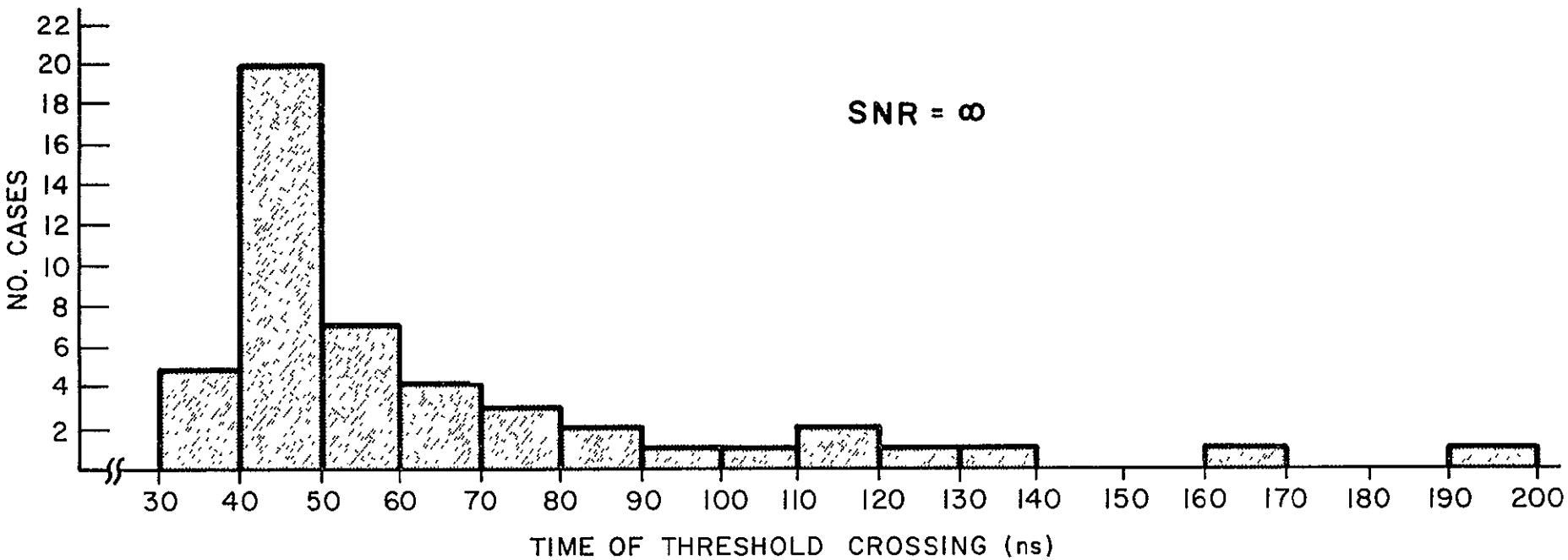

Fig. 2.14. Histogram of Pulse-By-Pulse Altitude Jitter for 50% Threshold

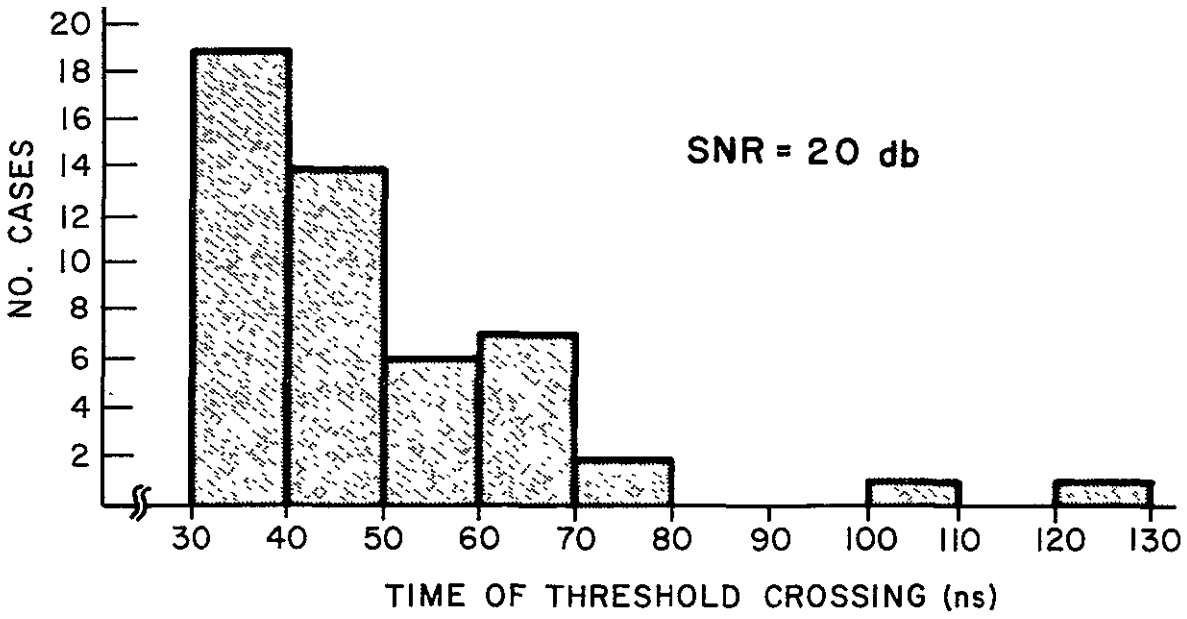

Fig. 2.15. Histogram of Pulse-By-Pulse Altitude Jitter for 33% Threshold

suggest that the 50 percent threshold performance could be improved by either receiver AGC action or by discarding or limiting the very late crossings. This last technique is somewhat akin to the limiting behavior of the time-discriminator used in split-gate systems. Use of AGC would require a sufficiently high prf so that AGC action could be derived on one pulse and applied to the next (correlated) pulse.

The simulation results show that both the 33 percent and 50 percent thresholds result in mean-values that are very close to the à priori values (levels selected from average waveforms such as Fig. 2.12). In view of the dependence upon SNR of the mean value encountered with the double-delay circuit, the threshold data suggest that a threshold technique may be less susceptible to this type of bias. In the future, threshold simulations will be conducted to determine the effect of SNR upon the mean value of the output.

Before leaving the threshold technique, mention should be made of the false-alarm problem and the open-loop altitude measurements. In order to reduce the false alarm rate, the threshold technique would require a much higher single pulse SNR than would the split-gate technique. Possible solutions to this problem, within the power constraint of a TWT transmitter, are: 1) use of pulse compression or 2) use of surface wave transversal filters[9]. Taking into account pulse stretching due to the antenna pattern, the transversal filter method could be implemented by transmitting several pulses spaced three microseconds apart. The threshold circuit is inherently suited to open-loop filtering, whereas the split-gate and double-delay circuits are basically closed-loop sensors.

2.5 EFFECT OF VIDEO NON-LINEARITY

In order to test the effect of non-linearity on a double-delay differencing form of altitude measurement, a video transfer function of the type

$$E_{out} = E_{in} - \frac{.01}{25} E_{in}^2$$

was simulated. Such non-linearity was assumed to be unknown (e.g., due to drift) in the altimeter. This function represents a quadratic non-linearity in the processor. Results of this simulation are given in Fig. 2.16. The variance is seen to be unchanged and the point of mean zero crossing shifted 1.4 ns compared

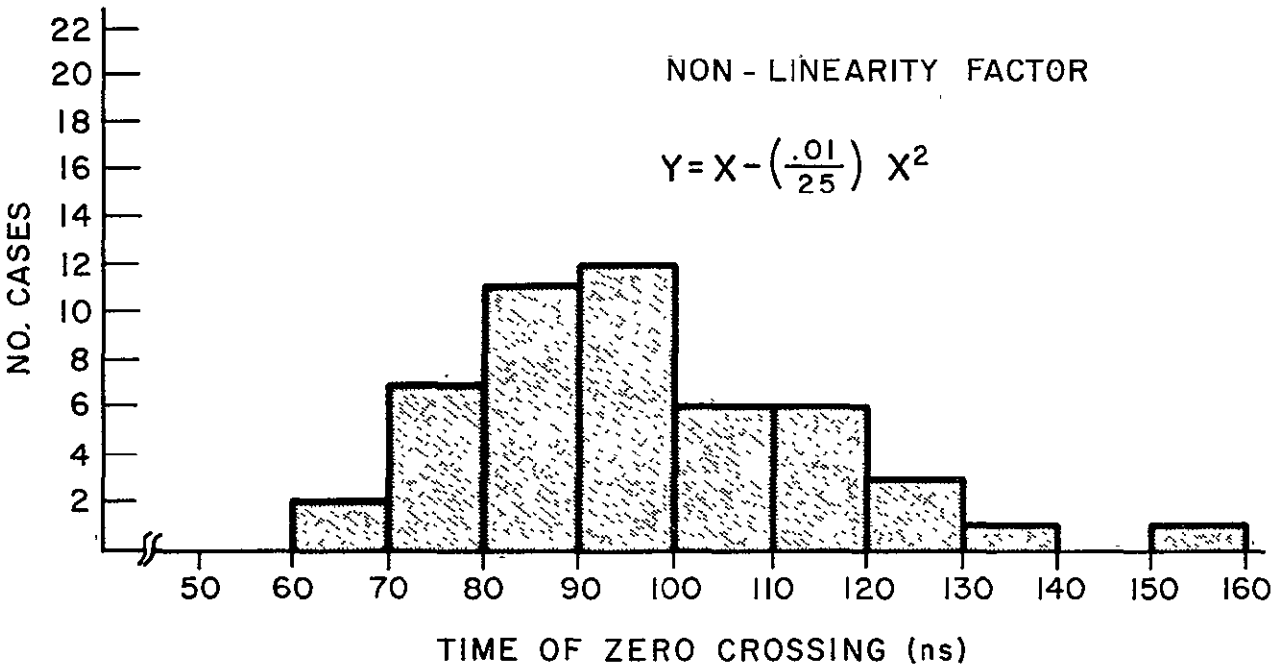

Fig. 2.16. Histogram of Pulse-By-Pulse Altitude Jitter for 1% Video Non-Linearity

to the data given in Fig. 2.6A. The assumed non-linearity represents a one percent departure at the 50 percent point on the mean waveform. The resultant shift is therefore somewhat larger than mean-value estimates would predict. For altimeter accuracies of 1 - 2 meters, non-linearities of this magnitude are not highly significant. For the Sea-Sat A, such non-linearities will be important.

2.6 PRF AND MISCELLANEOUS CONSIDERATIONS

Correlation properties of the altimeter signal may be estimated through computation of the Doppler spread of the scattered signal. Previously published estimates indicate that the Doppler spectrum will be in the neighborhood of 1600 Hz[1]. These figures are based on the signal characteristics at the break between the ramp and the plateau of the mean waveform, for a 50 ns pulse.

For the proposed GEOS-C orbit, a maximum vertical velocity component of about 700 ft./sec. will be present and will result in a (maximum) Doppler shift of approximately 10 KHz. Estimates[+] of the signal correlation properties derived from the Van Cittert-Zernike Theorem[10], place a value of up to 10 KHz on the signal fluctuation. For the purpose of this study, a conservative value of 1000 Hz was used.

Measurement of the vertical Doppler component would facilitate altitude extraction with elliptical orbits, since rate prediction could be used in the signal processor. Alternatively, it might be possible to difference the smoothed (e.g. one second) estimates of altitude to obtain prediction information. The third alternative would use a ground command and control function for this purpose. These techniques could minimize the problems associated with bandwidth and aquisition in a closed-loop tracker[4]. The ground control technique appears preferable from the standpoint of minimizing satellite equipment complexity.

Appendix C presents the results of a brief survey of prior work in optimal processing. The optimal video processor requires an impulse response that is related to the time-inverse of the sea-surface scattering function. From an engineering standpoint, it should be preferable to utilize only that part of the scattering function in the neighborhood of the ramp region. Accordingly, the optimum processor closely resembles an integrate-and-dump circuit, such as is involved in the split-gate tracker. It is therefore doubtful that any significant

---

[+] Suggested by G. Bush of Johns Hopkins University, Applied Physics Lab.

advantages would accrue from synthesizing the theoretically optimum processor encountered in the survey. Adaptive filtering should be investigated.

2.7 SUMMARY

A comparison of the altitude uncertainty for three sensing techniques is shown in Table III.

Table 2-3
Comparison of Altitude Errors
50 ns Pulse 1000 Samples

Sensor	Alt. Error (meters)
Double-delay (20 db SNR)+	.155
Split-gate (20 db SNR)*	.22
Threshold 50% (∞ SNR)	.25
Threshold 33% (20 db SNR)	.14
Theoretical (20 db SNR)	.20

+ Average of first two entries shown in Table II

* Scaled from data for a 100 ns pulse system with dc restorer, given in Ref. 4.

The results summarized in Table III indicate that any of the three sensing techniques considered are usable for the GEOS-C altimeter. (The data for the split-gate technique, shown in Table III, was not derived from the simulation and the figures shown are not directly comparable.) Because of the more extensive hardware experience and greater mean-value stability of the split-gate technique, it is recommended for closed-loop implementations. The threshold technique merits further work, especially if studies of Sea-Sat A requirements show non-analog techniques to be useful. From the processor standpoint, the main problems with Sea-Sat A are due to the mean-value shifts (e.g., non-linearity, systematic changes with SNR, environmental effects, and temporal variations). More information is needed regarding altimeter signal correlation properties (pulse-by-pulse) to determine the best solution to the signal fluctuation error problem with Sea-Sat A.

The theoretical analysis in this report shows that self-noise is a larger

error source than receiver noise, for a SNR greater than 10 db (see Fig. 2.8). This analysis correponds to the use of matched (non-adaptive) IF bandwidths and should be extended to treat pulse rise-time as a variable. A wider bandwidth per se will reduce self-noise errors. Altitude variances for a threshold system using rectangular pulse data (given in Appendix B) have been found to result in one-half the variance obtained for Gaussian shaped pulses.

In summary, the altimeter accuracy requirements for GEOS-C are within the state-of-the-art in radar performance. It is recommended that future studies emphasize Sea-Sat A problems and the development of sampling techniques for use with GEOS-C. The availability of information such as coherence time from the GEOS-C experiment would be of great value to the Sea-Sat A program.

Section 2

REFERENCES

1. The Raytheon Company, "Space Geodesy Altimetry Study", Final Report, NASA Contract NASW-1709, October 1968.

2. The Raytheon Company, "Pulse Compression Radar Study", Final Report, NASA Contract NASW-1709, August 1969.

3. Godbey, T. W. et al, "Equipment Specifications for a Space Rated Altimeter", Final Technical Report, The General Electric Company, Aerospace Electronics, Utica, New York, January 1969.

4. Godbey, T. W. et al, "Radar Altimeter Study Phase II", Final Report, The General Electric Company Aerospace Electronics, Utica, New York, January 1970.

5. Communications and Systems Inc., "Radar Altimeter Experiment for GEOS-C", Report No. R-4035-50-2, December 1968.

6. Lee, H. L., "The Range Error Statistics of a Satellite Radar Altimeter", Technical Report 112-2, The University of Kansas, Center for Research, Inc., Lawrence, Kansas, September 1969.

7. Price, Charles F., "Signal Processing in a Satellite Radar Altimeter", Experimental Astronomy Laboratory, Massachusetts Institute of Technology, Cambridge, Massachusetts, August 1968.

8. Papoulis, A., Probability, Random Variables, and Stochastic Processes, McGraw-Hill Book Company, New York, 1965.

9. Squire, W. B., "Linear Signal Processing and Ultrasonic Transversal Filters", IEEE Trans. Microwave Theory and Techniques, November 1969, p. 1020.

10. Born, M. and Wolf, L. F., "Principles of Optics", Pergemanon Press, New York, 1959.

SECTION 3

ALTIMETER SIMULATION MODEL

3.1 GENERAL DISCUSSION

The preceding section of this report presented results of theoretical analyses and computer simulation studies of the altimeter radar concept. The Monte Carlo technique used to generate the simulation results is described in detail in this section. The simulation approach was indispensable in several areas of the altimeter study because: 1) the mathematical complexity of the phenomena under investigation did not permit closed-form solution, or 2) the assumptions and approximations contained in available theoretical results led to limited confidence in the solutions so obtained. The statistical level-crossing problem and the analysis of time-varying signal statistics are examples of radar system functions that have not been rigorously solved. For non-Gaussian statistics there is a paucity of even approximate relationships in the literature.

The overall simulation program is shown in block-diagram form in Fig. 3.1. It consists of the computation of the ocean-scattered pulsed signal characteristics and the modifications resulting from the receiver bandpass characteristics, additive thermal noise, detector and other non-linear characteristics, and the altitude measurement process. Waveforms and statistical compilations are then obtained from the output data. The salient operations shown in Fig. 3.1 are described in detail below.

The electromagnetic scattering process for the ocean's surface may be visualized as due to specular regions superimposed on the gross wave structure. These specular regions consist of areas with proper orientations and curvature relative to the wavelength of the illuminating radiation. The scattering process is governed by the high frequency region of the ocean-wave spectrum. As discussed in Section 4, backscattered energy at normal incidence is a function of the mean-square slope of the ocean's surface. Since the backscattered signal from the ocean's surface is due to contributions from many individual scattering elements within the radar beamwidth, the well-known Rayleigh distribution of amplitudes

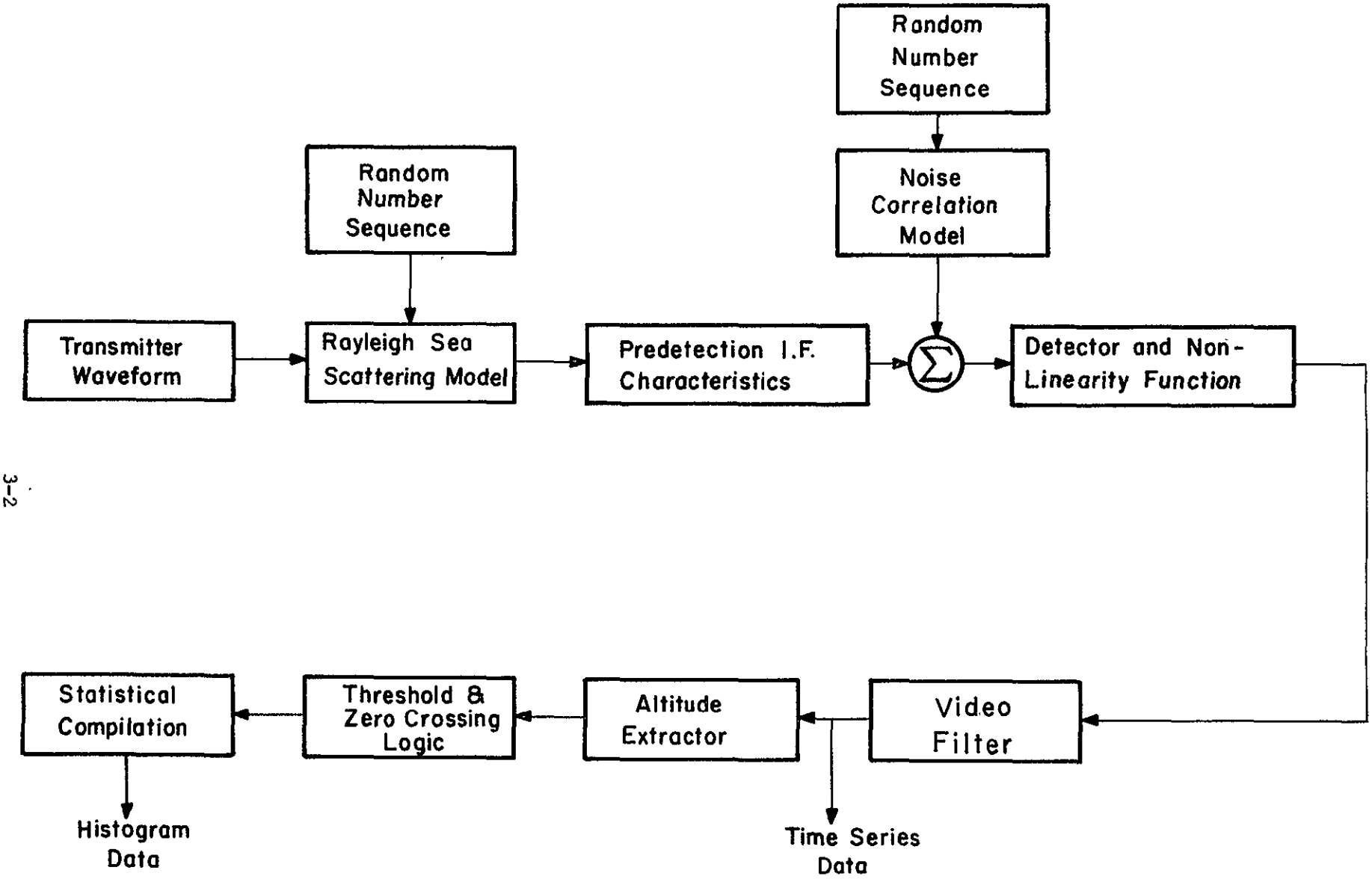

Fig. 3.1. Block-Diagram of Computer Simulation

results[1]. The principal reasons for the wide acceptance of this distribution are: 1) the fact that observed returns provide a reasonably good fit to Rayleigh statistics, and 2) the plausibility of the physical model (i.e. the specular model).

The simulation of ocean scattering is based upon the characteristics for backscattered power at normal incidence. For plane wave illumination at normal incidence, the average backscattered power $\bar{E}_s^2$ at a distance R_o from the scattering surface is[2]

$$\bar{E}_s^2 = \frac{|K|^2 E_i^2}{4\pi R_o^2} \left[\frac{4h_o^2}{\gamma^2}\right]^{-1} (\text{AREA}). \tag{1}$$

where

K is the Fresnel reflection coefficient

E_1 is the incident electric field intensity

h_o^2 is the variance of surface displacement about mean-sea-level, and

γ is related to the sea-surface correlation length.

This equation indicates that for a given radar wavelength and a time-invariant sea, the backscattered power is proportional to the illuminated area. Since the area illuminated by a finite antenna beamwidth impinging upon a spherical earth is a function of time, the backscattered power is also proportional to time. The area illuminated by a satellite-borne radar pointed toward the nadir is given by[2]

$$A(t) \approx \pi\ a\ c\ t \text{ for } t \leq t_p$$

where

a is the satellite altitude

c is the velocity of light, and

t_p is the transmitted pulse length.

For $t > t_p$, the radius of the leading edge r_L is given by

$$r_L \approx (a\ c\ t)^{1/2} \tag{2}$$

and the radius of the trailing edge is given by

$$r_t \approx [a\ c(t - t_p)]^{1/2}. \tag{3}$$

The projected illuminated area then is

$$A(t) = \pi r_L^2 \approx \pi\ a\ c\ t \text{ for } t \leq t_p \tag{4}$$

and

$$A(t) = \pi r_L^2 - \pi r_t^2 \approx \pi\ a\ c\ t_p \text{ for } t > t_p. \tag{5}$$

Thus, the projected area increases linearly for the length of a transmitted pulse, after which it remains relatively constant until other effects dominate.

3.2 MATHEMATICAL DESCRIPTION

In order to utilize the above model of radar return, macroscopic conditions must prevail since the existence of specularly reflecting points is a random occurrence. For the geodetic satellite geometry, examination of the scattered signal in one nanosecond increments corresponds to area increments of one square kilometer. An area of this size should contain at least five independent scatters and the Rayleigh distribution will match the expected signal statistics.

The Rayleigh amplitudes are simulated for each one-kilometer area by generating numbers x_i and y_i from independent normal distributions with zero mean and unit variance. The Rayleigh signals $e(n)_j$ at the output of a linear detector for rectangular pulse illumination are

$$e(n)_j = \left[\left(\sum_{i=1}^{n} x_{ij}\right)^2 + \left(\sum_{i=1}^{n} y_{ij}\right)^2\right]^{1/2} \qquad n \leq t_p \tag{6}$$

where the n subscript indicates the time index in one-nanosecond steps for the jth sample function. For a rectangular pulse, of length n = 50, the partial sums

($n \leq 50$) of $e(n)_j$ represent the transient region of the scattered pulse. For example, the partial sum for the first interval $e(1)_j$ corresponds to the aggregate return from the reflecting areas exposed during the first one nanosecond. (The term "time interval" and one nanosecond increment will be used interchangeably in the following discussion, although time can be scaled to an arbitrarily larger interval. Smaller time intervals correspond to areas for which the ocean surface statistics may not be independent.) For $n = 2$, $e(2)_j$ corresponds to the vectorial magnitude of returns from both area increments. Since the scattering areas are assumed uncorrelated, signal power will be additive and $e(2)_j$ will increase linearly (in the mean) up to the assumed pulse length ($n = 50$).

The simulated waveforms obtained for a rectangular pulse are mainly of theoretical interest because of the large receiver bandwidth implied. Figure 2.1 showed such waveforms for both the linear and square-law detector outputs. In order to simulate more realistic conditions, a Gaussian shaped pulse was used in the study of radar parameters. This waveform was chosen because the output of real networks with near-rectangular input signals resembles a Gaussian waveform[3].

A Gaussian envelope $f(t)$ of width W measured at the e^{-1} points is given by

$$f(t) = \exp\left[-\frac{t}{W/2}\right]^2$$

and the width of the spectrum $A(f)$ at the e^{-1} points for this envelope is

$$A(f) = \frac{1}{2\pi}\int_{-\infty}^{\infty} \exp\left[-\frac{t}{W/2}\right]^2 \exp\,(i2\pi ft)\,dt$$

$$= \frac{1}{(2\pi W)^{1/2}} \exp\left[-\left(\frac{\pi W f}{2}\right)^2\right]. \qquad (7)$$

The detected waveform for a Gaussian shaped pulse can be generated by the expression

$$e(k)_j = \left[\left(\sum_{i=1}^{200} x_i \exp\left\{-\left[\frac{2}{W}(k-i)\right]^2\right\}\right)^2 + \left(\sum_{i=1}^{200} y_i \exp\left\{-\left[\frac{2}{W}(k-i)\right]^2\right\}\right)^2\right]^{\frac{1}{2}} \qquad (8)$$

in which the time index k begins at k = -50 and terminates at k = 150. The peak of the pulse in this case corresponds to k = 1.

Equation (8) assumes that the effect of a Gaussian shaped transmitted pulse can be combined with the effect of a receiver containing a Gaussian shaped impulse response. This assumption is based on the linear model for sea return and the fact that convolution of two Gaussian functions yields a third Gaussian function. The convolution of the form

$$x_1(t) = \exp\left\{\frac{t^2}{T_1}\right\}$$

and (9)

$$x_2(t) = \exp\left\{\frac{t^2}{T_2}\right\}$$

can be shown to result in the Gaussian function

$$x_3(t) = \exp\left\{\frac{-t^2}{T_1^2 + T_2^2}\right\} . \tag{10}$$

Assuming post detection or video filtering can be described by an RC type filter with corner frequency f_1 given by

$$f_1 = \frac{1}{2\pi RC} \tag{11}$$

then the inpulse response h(t) for the filter is

$$h(t) = \frac{1}{RC} \exp\left\{- \frac{t}{RC}\right\} = 2\pi f_1 \exp\left\{-2\pi f_1 t\right\}. \tag{12}$$

If f_1 is equated to a multiple m of the one-sided bandwidth of the detected pulse given by equation (7), i.e.

$$f_1 = \frac{2m}{\pi W}$$

then h(t) is

$$h(t) = \frac{4m}{W} \exp\left\{-\frac{4m}{W} t\right\} . \tag{13}$$

Combining the above results, the signal at the output of an ideal envelope detector E_n is

$$E(n)_j = \frac{4m}{W} \sum_{k=-50}^{150} e(k)_j \exp\left\{-\frac{4m}{W}(n-k)\right\} . \tag{14}$$

Similarly, the output from a square-law detector $E^2(n)$ is given by

$$E^2(n)_j = \frac{4m}{W} \sum_{k=-50}^{150} e_j^2(k) \exp\left\{-\frac{4m}{W}(n-k)\right\} . \tag{15}$$

For the simulation results given in this report, k varied from -50 to +150 and W = 50. This corresponds to a 50 ns pulse, the peak of which arrives on the sea-surface at k = 1. Receiver time delays are not included in the formulation.

Receiver noise is added to the calculations through the equation

$$e(k)_j = \left[\left(\sum_{i=1}^{200} x_i \exp\left\{-\left[\frac{2(k-i)}{W}\right]\right\}^2 + c_k\right)^2 + \left(\sum_{i=1}^{200} y_i \exp\left\{-\left[\frac{2(k-i)}{W}\right]^2\right\} + s_k\right)^2\right]^{\frac{1}{2}} \tag{16}$$

in which c_k and s_k represent in-phase and quadrature noise voltages selected from independent distributions. These distributions are correlated in time to simulate the effects of receiver predetection bandwidth characteristics.

Before considering the details of receiver noise generation, the remaining aspects of the simulation will be discussed. The satellite altitude information is obtained by processing the video signal to extract an estimate of the time between signal transmission and receptions. The principal schemes for extracting

this estimate are: 1) early gate, late gate, 2) double-delay differencing, and 3) threshold detection. The double-delay differencing and threshold techniques have been implemented thus far in the simulation.

The threshold function is accomplished by level filtering in the digital program. The double-delay differencing operation is implemented through the discrete-time equivalent of the impulse response

$$h(t) = \delta(t) - 2\delta(t - \tau) + \delta(t - 2\tau)$$

where τ is the time lag and δ is a delta function. In programming this equation, the delayed replicas of the signal are combined with the original input through computer storage.

The remaining operations performed in the simulation program consist of non-linear transformations and the compilation of statistical descriptions (such as histogram data). The former is used to study the effect of system non-linearities on the altimeter data. To date, saturation forms of non-linearities of the type

$$E'_n = E_n - \kappa E_n^2 \tag{17}$$

have been used, in which κ is a parameter.

In order to establish signal-to-noise ratios (SNR) in the simulation, the variance of the signal process σ_s^2 must be known. For a Gaussian shaped signal, the autocorrelation function (ACF) of the signal $R_{ss}(\tau)$ is

$$R_{ss}(\tau) = k_s \int_{-\infty}^{\infty} \exp\{-B^2(t - \tau)^2\} \exp\{-B^2 t^2\}\, dt \tag{18}$$

in which k_s is the spectral density function for a shaping filter realization and $B = 2/W$. This function integrates as

$$R_{ss}(o) = \frac{k_s}{B} \sqrt{\frac{\pi}{2}} \stackrel{d}{=} \sigma_s^2 \tag{19}$$

and for B = 2/50 the signal variance is seen to be

$$\sigma_s^2 = k_s \ (25) \sqrt{\frac{\pi}{2}} \ . \tag{20}$$

Two techniques have been developed for the digital noise computations. The simulation results given in this report are based on the technique to be discussed first. The second method, which has not been programmed, was developed to assess the sensitivity of the zero crossing probability distributions to the noise process.

The first technique generates a correlated noise sequence through a recursive first-order difference equation which is driven with random noise. The c_k and s_k terms in (16) are generated through separate difference equations of the form

$$c_k = A_k c_{k-1} + w_k \tag{21}$$

in which w_k is an uncorrelated sequence (zero mean). The quantity A_k is obtained by forming the expectation E of c_k, i.e.

$$E\left[c_{k-1}c_k\right] = E\left[c_{k-1}(A_k c_{k-1} + w_k)\right] = A_k E\left[c_{k-1}c_{k-1}\right] \tag{22}$$

since $E[c_{k-1}w_k]$ is zero. Assuming that w_k is a zero mean process, this last result can be expressed as an ACF, i.e.

$$R_{k,k-1} = A_k R_{k-1,k-1} \tag{23}$$

or, in general

$$A_k = \frac{R_{jk}}{R_{kk}} \stackrel{d}{=} \rho_{jk} \tag{24}$$

which is the normalized ACF. The sequence c_k has a Gaussian realization with an ACF

$$\rho_{jk} = e^{-\alpha|k-j|} \stackrel{d}{=} e^{-\alpha|T_o|} \tag{25}$$

The variance of the c_k process can be found through the development

$$
\begin{aligned}
E(c_k c_k) &= E\left[(A_k c_{k-1} + w_k)\ (A_k c_{k-1} + w_k)\right] \\
&= E\ (A_k^2 c_{k-1}^2) + E(w_k^2) \\
&= E\ \left[A_k^2 (A_{k-1} c_{k-2} + w_{k+1})^2\right] + E(w_k^2) \\
&= \ldots
\end{aligned}
\tag{26}
$$

If A is time-invariant, this becomes for a unity variance w_k,

$$E(c_k c_k) = 1 + A^2 + A^4 + \ldots \tag{27}$$

which can be summed as

$$E(c_k c_k) = 1 + \frac{A}{1 - A^2} \stackrel{d}{=} \sigma_N^2 \qquad A < 1 \tag{28}$$

This equation is used to specify the steady state variance of the c_k sequence. Notice that the recursion must be initialized from a random number with the proper variance if the computations are re-started.

The correlation factor α in the ACF was obtained through a shaping filter analogy. If a shaping filter $H(j\omega)$ driven by white noise produces an exponential ACF, then the output spectrum $\phi(\omega)$ must be

$$\phi(\omega) = \int_{-\infty}^{\infty} R(T)\ e^{-j\omega T} dT = \frac{\alpha^2}{\omega^2 + \alpha^2}\ . \tag{29}$$

The transfer function of the shaping filter is readily seen to be

$$H(j\omega) = \frac{1}{j\frac{\omega}{\alpha} + 1}\ . \tag{31}$$

Note that α is the 3 db bandwidth in radian measure. The equivalent rectangular bandwidth is

$$\int_{o}^{\infty} \frac{dt}{1 + \left(\frac{\omega}{\alpha}\right)^2} = \frac{\alpha}{4} . \tag{31}$$

Thus the $H(j\omega)$ transfer function has a bandwidth equivalent to an idealized rectangular bandpass of $(\pi/2)f$.

For a corner frequency of 20 MHz, the ACF is

$$\rho(\tau) = e^{-125 \times 10^6 \tau} \tag{32}$$

where τ is in nanoseconds.

Analogous to (18), the signal-to-noise ratio is obtained by defining σ_n^2 as

$$\sigma_n^2 = \frac{1}{2\pi} \int_{-\infty}^{\infty} s \frac{\alpha^2}{\alpha 2 + \omega 2} \, d\omega = \frac{k\alpha}{2} . \tag{33}$$

Therefore, the signal-to-noise ratio for the simulation is

$$SNR = \frac{\sigma_s^2}{\alpha_n^2} = \frac{25\sqrt{\frac{\pi}{2}}}{\frac{\alpha}{2}} = \frac{50}{\alpha}\sqrt{\frac{\pi}{2}} = \frac{50}{f\alpha}\sqrt{\frac{1}{4\pi}} . \tag{34}$$

The second method of noise generation was designed to provide noise correlation properties that are matched to the signal characteristics. It assumes that the IF bandpass characteristics are Gaussian to first-order. If a Gaussian bandpass to an Nth order approximation were used, then the normalized ACF ($\rho(\tau)$) could be computed for all time lags τ. Noise would thus be generated by considering not just the last value, but all previously known values in a joint probability distribution of N variables. For a first-order approximation, it was assumed that $\rho(\tau)$ is known for only a fixed increment τ.

For the bivariate Gaussian distribution

$$P(I_1,I_2) = \frac{1}{2\pi\alpha^2[1 - \rho^2(\tau)]} \exp \left\{ - \left[\frac{I_1^2 + I_2^2 - 2I_1I_2\rho(\tau)}{2\alpha^2[1 - \rho^2(\tau)]} \right] \right\} \tag{35}$$

where the α variances are equal, letting $I_2 = I_1 + \Delta I$ and integrating over I_1 gives

$$P(\Delta I,T) = \frac{1}{2\alpha\sqrt{\pi(1 - \rho(\tau))}} \exp\left\{- \frac{(\Delta I)^2}{4\alpha^2[1 - \rho(\tau)]}\right\} \tag{36}$$

in which $P(\Delta I,T)$ is the probability of a change in I in a time T. This distribution is Gaussian with variance $2\sigma^2[1 - \rho(\tau)]$.

The numerical values of the correlation parameter can be established as follows. For a Gaussian waveform

$$y(t) = \exp\left\{-\left(\frac{t}{T}\right)^2\right\} \tag{37}$$

in which T is one-half the pulse duration at the e^{-1} points, the spectral width (one sided) is $f_o = 1/(T\pi)$. Using a transfer function with a squared magnitude of

$$|G(f)|^2 = \exp\left\{-2\,\frac{f^2}{f_o^2}\right\} \tag{38}$$

the normalized ACF $\rho(\tau)$ is found to be

$$\rho(\tau) = \int_{-\infty}^{\infty} \exp\left\{-\frac{2f^2}{f_o^2}\right\} \exp\{-2\pi i f\tau\}\, df = \exp\left\{-\left(\frac{\tau}{2T}\right)^2\right\}. \tag{39}$$

Therefore, for 2T = 50 nanoseconds, the correlation parameter is

$$\rho(\tau) = \exp\left\{-\left(\frac{\tau}{37}\right)^2\right\} \tag{40}$$

in nanoseconds.

Section 3

REFERENCES

1. Skolnik, Merrill I., "A Review of Radar Sea Echo", The Naval Research Laboratory, Washington, D. C., Report No. 2025, July 1969.

2. The Research Triangle Institute, "A Review of Electromagnetic Scattering from the Ocean's Surface", Report on NASA Contract No. NASW 1909, September 1969.

3. Burdic, W. S., Radar Signal Analysis, Prentice Hall, Inc., Englewood Cliffs, N. J., 1968.

SECTION 4

REVIEW OF ELECTROMAGNETIC SCATTERING FROM ROUGH SURFACES AS RELATED TO THE GEODETIC ALTIMETER

4.1 GENERAL DISCUSSION

Satellite altimetry, as presently proposed for the GEOS satellite, is heavily dependent on characteristics of the backscattered signal from the ocean surface. The altimeter techniques under consideration use a beamwidth sufficiently broad (2-3 degrees) that with reasonable satellite attitude control, strong radar returns will always be reflected from the sub-satellite point. The use of pulses in the range of 50-100 nanoseconds ensures that at satellite altitudes of 1000 km, the transient portion of the return will indeed be backscattered normally from the sea surface.

At satellite altitudes of 1000 km, the footprint of the initial 100 nanoseconds of the reflected pulse has a radius of 5.5 km which constitutes a half angle of five milliradians. Consequently, the angle of incidence is very nearly zero during this portion of the pulse, with a total variation of $\pm$ 5 milliradians. With the possible exception of a completely flat sea surface, this variation of incidence angle can be neglected and the analysis can be confined to the case of normal incidence. The significance of this simplification is apparent when one considers the complexity of an analysis which attempts to predict angular dependence of scattered power over the range of angles from 0-90 degrees. Barrick[1] has demonstrated that the usual approximations made in evaluating the vector Kirchoff integrals for rough surfaces generally lead to results which may be in error at angles of incidence greater than 20 degrees. There is, however, excellent unanimity for the theory near normal incidence; Barrick[1], Hagfors[2], and Fung and Moore[3] have shown that models employing geometrical and physical optics can lead to identical answers near normal incidence.

The details of radar backscattering from the sea surface are presented in paragraph 4.3, where allowance is made for the fact that the energy spectrum of a sea is in general anisotropic. The present knowledge of the sea surface energy spectrum is not sufficint to allow calculation of these effects. At normal incidence the radar cross-section is known to be

a function of the mean-square slope of the sea surface. A few measurements of the mean-square slope and the mean-square height of ocean waves have been made. Munk[5] observed that when wave numbers corresponding to spatial wavelengths of less than one foot were removed from the ocean spectrum by means of artificial slicks, the mean-square height of the waves (proportional to the integral of S(k)) was essentially unaffected but that the measured mean-square slope (proportional to the integral of $k^2S(k)$) was reduced by a factor of three. This means that although the scattered power at normal incidence is heavily influenced by sea slopes, it is rather insensitive to the mean-square height of the waves, the latter being a commonly observed oceanographic variable.

4.2 SUMMARY

With X-band satellite altimetry, for waves with rms heights greater than one-half foot,

1. The backscatter cross-section at normal incidence will in general be inversely proportional to the mean-square slope and the degree of anisotropy of the sea surface;
2. assuming a Gaussian shaped autocorrelation function, the incremental signals, sampled at nanosecond intervals for times up to 150 nanoseconds (after the leading edge of the pulse hits the sea), will be independent; and
3. the incremental areas uncovered at nanosecond intervals are large enough to expect that the distribution of the amplitudes of the incremental signals will be Rayleigh-like.

The significance of these results to the simulation of sea returns was discussed in Section 3. In regard to the geodetic altimeter program, this study has led to the following conclusions[6]: Backscattered power can be related to mean-square slope of the sea surface. Experimental programs using radar scatterometers have indicated that empirical relationships can be used to relate the scattered power (slope dependent) to ocean surface winds. A considerable extension of the presently available oceanographic information (e.g., two-dimensional slope spectra) would be needed to place these empirical relationships on a theoretical

basis. Assuming that the empirical results can be used reliably to infer surface winds, the wind information may be used to infer rms wave height forecast programs and other uses. As discussed in Section 5, the oceanographic relationships between mean-square slope and wind velocity are not known to the extent required to permit an electromagnetic solution to the problem. The ocean measurement problems are immense.

4.3 RADAR BACKSCATTERING FROM THE SEA

The design of a satellite-borne radar altimeter will be dependent upon knowledge of the characteristics of the radar backscattering from the sea surface. Backscattering at all incidence angles from a rough surface has received a great deal of attention by numerous authors. The subject is most complex and there is no uniform agreement except near normal incidence for a very rough surface.

At near normal incidence, Barrick[1] has shown that the radar backscattering cross-section is given by

$$\sigma = Kk^2 \iiiint \exp\{-4k^2h_o^2[1 - \rho(x,x', y, y')]\}\, dxdy\, dx'dy' \qquad (1)$$

where: the limits on the integrals are defined by the area illuminated by the radar pulse;

K is a function of sea surface conditions (mean-squared slope) and of the Fresnel reflection coefficient (near normal incidence K is relatively insensitive to sea surface slope);

h_o^2 is mean-squared height of the waves;

ρ (x, x', y, y') is the normalized surface spatial correlation coefficient;

k is the Fourier wave number = $\frac{2\pi}{\lambda}$ in which λ is r-f wavelength; and

(x,y) and (x',y') are positions on the mean sea surface.

The derivation of this equation is based upon physical optics approximations to the Stratton-Chu integral equation. The major assumption is the use of the tangent plane approximation to the surface which requires that the radius of curvature of the surface be large in comparison to the

wavelength of the incident radiation. At a wavelength of three centimeters (X-band) it is not clear that the tangent plane approximation is appropriate for a sea surface with capillary waves. On the other hand, the capillary waves are only millimeters high and, at normal incidence, the effect of millimeter scale irregularities on three centimeter energy is not expected to be large. It is recognized, however, that there may be some error involved in the use of the tangent plane approximation.

A second approximation has been introduced by assuming that the joint probability density distribution of the wave heights at positions (x,y) and (x',y') is a normal (Gaussian) distribution with zero mean value and variance h_o^2. Kinsman[4], among others, presents experimental evidence which indicates that the height of the sea surface is, only to a first order, a normally distributed variable. Since the surface statistics were assumed to be homogeneous, the correlation of the height fluctuations at any two points is a function only of the difference of the coordinates of the points and not of the absolute value of the positions of the two points.

The homogeneous assumption allows (1) to be expressed as follows:

$$\sigma = Kk^2 \iiiint \exp\left\{-\frac{16\pi^2 h^2}{\lambda^2}\left[1 - \rho(x-x',y-y')\right]\right\} dxdy\, dx'dy'$$

with $x-x' = \Delta x$

$y-y' = \Delta y$

and integrating oven an L_x, L_y square area gives

$$= Kk^2 \int_{-L_x/2}^{L_x/2} \int_{-L_y/2}^{L_y/2} \int_{x-L_x/2}^{x+L_x/2} \int_{y-L_y/2}^{y+L_y/2} \exp\left\{-\frac{16\pi^2 h^2}{\lambda^2}\left[1 - \rho(\Delta x,\Delta y)\right]\right\} d\Delta x d\Delta y\, dxdy. \quad (2a)$$

Note that since $\frac{16\pi^2 h^2}{\lambda^2} >> 1$, if ρ (Δx, Δy) departs from one, i.e., for Δx and Δy differing much from zero, the exponent in the integrand would become quite large. The major contribution to the relative coordinate integral (in 2a) occurs for $\Delta x, \Delta y \approx 0$. The exact limits of the relative integral are not important (so long as L_x and L_y are large in comparison to the regions of Δx and Δy which contribute to the integral) and we can extend the limits of the relative coordinate integral to infinity without incurring appreciable error,

$$\sigma = Kk^2 \int_{-\frac{L_x}{2}}^{\frac{L_x}{2}} \int_{-\frac{L_y}{2}}^{\frac{L_y}{2}} \int_{-\infty}^{\infty} \int_{-\infty}^{\infty} \exp\left\{-\frac{16\pi^2 h^2}{\lambda^2}[1-\rho(\Delta x,\Delta y)]\right\} d\Delta x d\Delta y \, dx dy \tag{2b}$$

$$\sigma = Kk^2 \text{ Area} \iint_{-\infty}^{\infty} \exp\left\{-\frac{16\pi^2 h^2}{\lambda^2}[1-(x, y)]\right\} d\Delta x d\Delta y. \tag{2c}$$

Before proceeding, it should be noted that a sea surface composed of infinitely long-crested waves of a single frequency will cause the above arguments to fail. Suppose the waves were traveling in the x direction. The correlation function in the x direction will be periodic and the relative coordinates in the x direction cannot be replaced with infinite limits. In the y direction, the correlation function will be unity for all y. The relative limits for y cannot be replaced with infinite limits either. While it is true that on a real ocean the likelihood of a single frequency, infinitely long-crested wave is zero (the ocean is of finite size), with a sufficiently small antenna footprint (corresponding to an extremely short pulse length) a moderately long-crested narrow band swell could seriously invalidate equations (2b) and (2c).

If the correlation function is assumed differentiable at the origin, then a Taylor series expansion about the point (0,0) is

$$\rho(\Delta x,\Delta y) = \rho(0,0) + \Delta x \left.\frac{\partial\rho}{\partial\Delta x}\right|_{\Delta x=\Delta y=0} + \Delta y \left.\frac{\partial\rho}{\partial\Delta y}\right|_{\Delta x=\Delta y=0} + \frac{(\Delta x)^2}{2} \left.\frac{\partial^2\rho}{\partial\Delta x^2}\right|_{\Delta x=\Delta y=0}$$

$$+\frac{(\Delta y)^2}{2} \left.\frac{\partial^2\rho}{\partial\Delta y^2}\right|_{\Delta x=\Delta y=0} + (\Delta x)(\Delta y) \left.\frac{\partial^2\rho}{\partial\Delta x\partial\Delta y}\right|_{\Delta x=\Delta y=0} + \ldots \tag{3a}$$

In the following development we shall show that

$$\left.\frac{\partial\rho}{\partial\Delta x}\right|_{\Delta x=\Delta y=0} = \left.\frac{\partial\rho}{\partial\Delta y}\right|_{\Delta x=\Delta y=0} = 0,$$

consequently,

$$\rho(\Delta x,\Delta y) \doteq 1-a^2(\Delta x)^2-b^2(\Delta y)^2-c^2(\Delta x)(\Delta y). \tag{3b}$$

where

$$a^2 = -1/2 \left.\frac{\partial^2\rho}{\partial\Delta x^2}\right|_{\Delta x=\Delta y=0}$$

$$b^2 = -1/2 \left.\frac{\partial^2\rho}{\partial\Delta y^2}\right|_{\Delta x=\Delta y=0}$$

$$c^2 = -\left.\frac{\partial^2\rho}{\partial\Delta x\,\partial\Delta y}\right|_{\Delta x=\Delta y=0}$$

Thus,

$$1-\rho(\Delta x,\Delta y) \doteq a^2(\Delta x)^2 + b^2(\Delta y)^2 + c^2\,\Delta x\Delta y \tag{4}$$

Equation (4) shows that the isocorrelation contours for small values of x and y are elliptical. For larger values of x and y more terms of the Taylor series expansion would be required and the contours need not be elliptical. However, for very high frequency backscattering, the elliptical approximation appears reasonable. The proof of the preceeding discussion follows.

Let $z(x,y,t)$ represent the height of the sea surface at the position x,y and the time t

$$z(x,y) = \iint_{-\infty}^{\infty} S(k_x,k_y) \exp\{i[k_x x + k_y y]\} \, dk_x dk_y$$

From transform theory, since $z(x,y,t)$ is a real variable, $S(k_x,k_y) = S^*(-k_x,-k_y)$. If the height fluctuations are averaged at two points x,y and x', y' we obtain

$$\overline{z(x,y)\, z(x',y')} = \iiiint_{-\infty}^{\infty} \overline{S(k_x,k_y)\, S^*(k_{x'},k_{y'})} \exp\{i[k_x x - k_x' x' + k_y y - k_y' y']\} \, dk_x dk_y dk_x' dk_y' \tag{5}$$

For homogeneous, stationary sea surface statistics, $\overline{z(x,y)\, z(x'y')}$ should be independent of time t and a function only of $x'-x$ and $y'-y$. This can only be true if

$$\overline{S(k_x,k_y)\, S^*(k_x',k_y')} = \overline{|S(k_x,k_y)|^2}\, \delta(k_x - k_x')\, \delta(k_y - k_y') \tag{6}$$

where

$$\overline{|S(k_x,k_y)|^2} = \overline{|S(-k_x,k_y)|^2} = F(k_x,k_y) = F(-k_x,-k_y)$$

since

$$\overline{z(x,y)\ z(x',y')} = R(\Delta x,\Delta y)$$

$$= \iiiint_{-\infty}^{\infty} F(k_x,k_y)\ \delta(k_x - k_x')\ \delta(k_y - k_y')$$

$$\exp\ \{i[(k_x - k_x')\ x - k_x'\Delta x + (k_y - k_y')\ y - k_y'\Delta y]\}$$

$$dk_x dk_y\ dk_x' dk_y'$$

$$R(\Delta x,\Delta y) = \iint_{-\infty}^{\infty} F(k_x,k_y)\ \exp\ \{-i[k_x\Delta x + k_y\Delta y]\}\ dk_x dk_y\ dk_x' dk_y' \tag{7}$$

$$\rho(\Delta x,\Delta y) = \frac{R(\ x,\ y)}{R(0,0)} = \frac{\iint_0^{\infty} F(k_x,k_y)\ \cos\ [k_x\Delta x + k_y\Delta y]\ dk_x dk_y}{\iint_0^{\infty} F(k_x,k_y)\ dk_x dk_y} \tag{8}$$

Therefore

$$\frac{\partial\rho}{\partial\Delta x} = \frac{-\iint_0^{\infty} k_x F(k_x.k_y)\ \sin\ [k_x\Delta x + k_y\Delta y]\ dk_x dk_y}{\iint_0^{\infty} F(k_x,k_y)\ dk_x dk_y} \tag{9}$$

$$\frac{\partial\rho}{\partial\Delta y} = \frac{-\iint_0^{\infty} k_x F(k_x,k_y)\ \sin\ [k_x\Delta x + k_y\Delta y]\ dk_x dk_y}{\iint_0^{\infty} F(k_x,k_y)\ dk_x dk_y} \tag{10}$$

$$\frac{\partial^2\rho}{\partial\Delta x\partial\Delta y} = \frac{-\iint_0^{\infty} k_x k_y F(k_x k_y)\ \cos\ (k_x\Delta x + k_y\Delta y)\ dk_x dk_y}{\iint_0^{\infty} F(k_x,k_y)\ dk_x dk_y} \tag{11}$$

$$\frac{\partial^2 \rho}{\partial \Delta x^2} = \frac{-\iint_0^\infty k_x^2 \; F(k_x k_y) \; \cos\,(k_x \Delta x + k_y \Delta y) \; dk_x dk_y}{\iint_0^\infty F(k_x k_y) \; dk_x dk_y} \tag{12}$$

$$\frac{\partial^2 \rho}{\partial \Delta y^2} = \frac{-\iint_0^\infty k_y^2 \; F(k_x k_y) \; \cos[k_x \Delta x + k_y \Delta y] \; dk_x dk_y}{\iint_0^\infty F(k_x k_y) \; dk_x dk_y} \tag{13}$$

Evaluating (8), (9), (10), (11), (12),(13) for $\Delta x = \Delta y = 0$ gives:

$$\rho\;(0,0) = 1$$

$$\left.\frac{\partial \rho}{\partial \Delta x}\right|_{\Delta x = \Delta y} = \left.\frac{\partial \rho}{\partial \Delta y}\right|_{\Delta x = \Delta y = 0} = 0$$

$$-1/2 \left.\frac{\partial^2 \rho}{\partial \Delta x^2}\right|_{\Delta x = \Delta y} = \frac{1/2 \iint_0^\infty k_x^2 \; F(k_x k_y) \; dk_x dk_y}{\iint_0^\infty F(k_x k_y) \; dk_x dk_y} = a^2 \tag{14}$$

$$-1/2 \left.\frac{\partial^2 \rho}{\partial \Delta y^2}\right|_{\Delta x = \Delta y = 0} = \frac{1/2 \iint_0^\infty k_y^2 \; F(k_x k_y) \; dk_x dk_y}{\iint_0^\infty F(k_x k_y) \; dk_x dk_y} = b^2 \tag{15}$$

$$-\left.\frac{\partial^2 \rho}{\partial \Delta x \partial \Delta y}\right|_{\Delta x = \Delta y = 0} = \frac{\iint_0^\infty k_x k_y \; F(k_x k_y) \; dk_x dk_y}{\iint_0^\infty F(k_x k_y) \; dk_x dk_y} = c^2 \tag{16}$$

It is noted that in view of (8), the correlation function can be considered to result from waves travelling in the k_x, k_y directions. Since $F(k_x,k_y) = F(-k_x,-k_y)$, the correlation function could equally well arise from waves travelling in the $-k_x$, $-k_y$ directions. There is an inherent 180° ambiguity in the direction of travel of the waves which make up the spectrum.

4.4 CALCULATION OF THE NORMAL INCIDENCE RADAR BACKSCATTERING CROSS-SECTION

The physical optics approximation to the normal incidence backscattering cross-section per unit area of illuminated rough sea leads to

$$\sigma/\text{area} = Kk^2 \iint_{-\infty}^{\infty} \exp\{-(\frac{4\pi h}{\lambda})^2 [a^2(\Delta x)^2 + b^2 (\Delta y)^2 + c^2(\Delta x)(\Delta y)] \, d\Delta x d\Delta y \tag{17}$$

It may not prove feasible to use oceanographic spectra to evaluate the constants a^2, b^2 and c^2 since oceanographic spectra do not usually have sufficient detail (at the high wave number end of the spectrum) to permit an accurate evaluation through (11), (12), or (13). Nonetheless, it is possible to relate the cross-section to an oceanographic variable (even though there may be some doubt as to the pertinence of the oceanographic measurement).

The maximum slope of the sea surface at the point $z(x,y)$ is given by

$$\nabla z(x,y) = \frac{\partial z}{\partial x} \hat{x} + \frac{\partial z}{\partial y} \hat{y}$$

The mean square slope of the surface is

$$\overline{|\nabla z\ (x,y)|^2} = \overline{\left|\frac{\partial z}{\partial x}\right|^2} + \overline{\left|\frac{\partial z}{\partial y}\right|^2} = s^2$$

It can be shown that if $z(x,y)$ has a power spectrum $F(k_x,k_y)$ then $\overline{\left|\frac{\partial z}{\partial x}\right|^2}$ and $\overline{\left|\frac{\partial z}{\partial y}\right|^2}$ have power spectral densities $k_x^2 F(k_x,k_y)$ and $k_y^2 F(k_x,k_y)$

respectively. The mean squared values of $\frac{\partial z}{\partial x}$ and $\frac{\partial z}{\partial y}$ are given by

$$s_x^2 = \overline{\left|\frac{\partial z}{\partial x}\right|^2} = \iint_{-\infty}^{\infty} k_x^2 \, F(k_x k_y) \, dk_x dk_y = -h^2 \left.\frac{\partial^2 \rho}{\partial \Delta x^2}\right|_{\Delta x=\Delta y=0} = 2h^2 a^2 \tag{18}$$

$$s_y^2 = \overline{\left|\frac{\partial z}{\partial y}\right|^2} \iint_{-\infty}^{\infty} k_y^2 \, F(k_x k_y) \, dk_x dk_y = -h^2 \left.\frac{\partial^2 \rho}{\partial \Delta y^2}\right|_{\Delta x=\Delta y=0} = 2h^2 b^2 \tag{19}$$

Substituting (18) and (19) into (20) gives

$$\sigma/\text{area} = Kk^2 \iint_{\infty}^{\infty} \exp\left\{ \frac{-16\pi^2}{\lambda 2} \left[\frac{s_x^2}{2} (\Delta x)^2 + \frac{s_y^2}{2} (\Delta y)^2 + h^2 c^2 \Delta x \Delta y \right] \right\} d\Delta x d\Delta y \tag{20}$$

The term c^2 can be related to the slope covariance, i.e.

$$h_o^2 \, c^2 = \left| \frac{\partial z}{\partial x} \; \frac{\partial z}{\partial y} \right|$$

In general then, the normal incidence radar backscattering is an inverse function of the mean square slope of the sea. It should also be observed that the cross-section is also a function of the degree of anisotropy of the sea surface as is evidenced by the term $h_o^2 \, c^2 \, (\Delta x) \, (\Delta y)$.

One-dimensional ocean wave spectra have been obtained from measurements of wave height versus time at a single point. These measurements are first processed to yield a frequency spectrum which, through the application of the wave dispersion relation, is then interpreted as one-dimensional spatial spectrum. This type of analysis is not without its difficulties because of the averaging of the high frequency components by the transducer as well as the neglect of nonlinearities in the wave equation.

Two-dimensional spectra can be obtained directly from stereo photographs of the sea as demonstrated by Cote, Pierson, et al.[7]. For a variety of reasons, not the least of which is the sheer magnitude of the task, the spectra so derived do not represent the components whose spatial periodicity

is less than 30 feet. Consequently the high wave number end of the ocean wave spectrum is not well known. It should be noted that the very high wave number end of the spectrum is far less important to the oceanographer than it is to the radar user.

For these reasons the importance of the slope covariance on radar cross section has not as yet been evaluated. Frequently, in the absence of knowledge about the detailed behavior of the spectral density function $F(k_x,k_y)$ at high frequencies, the radar backscattering cross-section is specialized to the case of an isotropic sea surface. Under these circumstances s_x^2 is equal to s_y^2 and c^2, the covariance $\overline{\left|\frac{\partial z}{\partial x} \quad \frac{\partial z}{\partial y}\right|}$ is zero. For an isotropic surface

$$\sigma/\text{area} = Kk^2 \iint_{-\infty}^{\infty} \exp\left\{\frac{-8\pi^2}{\lambda^2}\cdot\left[s_x^2\,(\Delta x)^2 + s_y^2\,(\Delta y)^2\right]\right\} d\Delta x d\Delta y \tag{21}$$

$$\sigma/\text{area} = \frac{K\pi}{s^{-2}}$$

Equation (21) is particularly simple and clearly shows the inverse dependence of radar cross-section upon the mean-square slope.

In order to make clear the physical basis for some of the arguments which follow, (2c) will be re-examined for the case of an isotropic sea surface. In this case

$$\sigma = Kk^2 \text{ area} \iint_{-\infty}^{\infty} \exp\left\{\frac{-16\pi^2h^2}{\lambda^2}\left[1-\rho(\Delta x,\Delta y)\right]\right\} d\Delta x d\Delta y$$

$$\sigma/\text{area} = 2\,Kk^2 \int_0^{\infty} \exp\left\{\frac{-16\pi^2h^2}{\lambda^2}\left[1-\rho(r)\right]\right\} r\,dr \tag{22}$$

where $\rho(r)^2 = (\Delta x)^2 + (\Delta y)^2$

and $\rho(r) = \rho\sqrt{(\Delta x)^2 + (\Delta y)^2}$ . . .

which is seen to be the isotropic case.

It is clear that if $\frac{16\pi^2 h^2}{\lambda^2}$ is a large number, the major contribution to (22) will occur for small values of $\rho(r)$ such that $\rho(r) = 1-\delta$ where δ is a very small number. A two term Taylor series expansion for $\rho(r)$ is given by

$$\rho(r) = 1 - \frac{r^2}{z} \left.\frac{\partial^2 \rho}{\partial r^2}\right|_{r=0} + \ldots$$

$$\sigma/\text{area} = Kk^2\, 2\pi \int^{\infty} \exp\left\{-\frac{16\pi^2 h^2}{\lambda^2}\left(1/2 \left.\frac{\partial^2 \rho}{\partial r^2}\right|_{r=o}\right) r^2\right\} r\,dr \tag{23}$$

$$\sigma/\text{area} = 2\pi K k^2 \frac{\lambda^2}{16\pi^2 h^2 (1/2) \left.\frac{\partial^2 \rho}{\partial r^2}\right|_{r=0}} \tag{24}$$

Comparison of (21) with (24) will show that $\left(\frac{\pi^2 h_o^2}{k^2 \lambda^2}\right)\left(\frac{\partial^2 \rho}{\partial r^2}\right)$ must equal $\frac{s^2}{4}$. Direct calculation will verify that $\sigma/\text{area} = \frac{k\pi}{s^2}$. Therefore the radar cross-section for an isotropic rough surface is inversely proportional to the mean squared slope.

The significant feature of this last derivation, which will be used in certain following sections, is that for a rough isotropic surface the major contribution to the integral in (22) occurs for relatively small values of r such that the $\rho(r) \simeq 1$.

4.5 COHERENCE OF BACKSCATTERED SIGNAL

If the entire illuminated surface of the sea were to act as a flat coherent reflector, the returned power should be proportional to the square of the area illuminated. However, the arguments following equation (2) indicate that when the illuminated area exceeds a critical size, the return is proportional to the first power of the illuminated area. Just what are the dimensions over which the sea acts as a coherent reflector? The linear dimensions can never exceed (at high frequencies) the surface correlation length L, and in fact will be shown to be considerably smaller.

Consider, for illustrative purposes only, that the normalized correlation function of the sea surface is Gaussian:

$$\rho(r) = \exp\{-\frac{r^2}{L^2}\} = 1-\frac{r^2}{L^2} \quad \text{for small } r. \tag{25}$$

At x-band, with an rms wave height of one-half foot, the analysis shows that the main contribution to the integral in (2) occured for small values of $r \leq r_1$ where r_1 is defined by

$$[\frac{4\pi h}{2}]^2 \; [\, 1-\rho(\tau_1)] = 4 \tag{26}$$

Therefore,

$$\rho(r_1) = .999 = 1-(\frac{r}{L})^2$$

and

$$\frac{r}{L} = 3 \times 10^{-2}$$

This value of r, which is less than 3 percent of the correlation length, is a measure of the distance over which fields are correlated on the sea surface. Since the contribution to the integral is quite small outside of r_1, r_1 is considered to be a conservative estimate of the linear size of a coherent scattering element. Taking r_1 to be 3 percent of the surface correlation length, for L as large as 500 meters, r_1 is still only 15 meters.

The number of independent scattering areas can be estimated as follows: The radar footprint on the sea-surface expands radially with time. During each one nanosecond time increment that the radius of the footprint increases by 15 meters, the scattering from the incremental areas shall be considered to be independent (uncorrelated) of the previously uncovered area. The radius of the radar footprint as a function of time, t, after the leading edge of the pulse has reached the sea-surface is given by

$$r_L = [act]^{1/2} \text{ for } t \leq t_p \tag{27}$$

where r is the footprint

a is the satellite altitude

t_p is the pulse length.

If a is taken to be 1000 kilometers, then for t_p = 100 nanoseconds the increment of the radius uncovered between (t = 99 to 100 nanoseconds)

$$\Delta r_{100} = r_{100} - r_{99} = 25 \text{ meters}$$

$$\text{for } \Delta r_{100} > r_1$$

In a similar fashion, $\Delta r_{150} = r_{150} - r_{149}$ is approximately 20 meters.

Therefore, incremental signals at nanosecond intervals are incoherent for times as long as 150 nanoseconds after the leading edge of the pulse reaches the sea and the footprint radius is approximately 550 meters.

4.6 FREQUENCY DEPENDENCY

The results obtained in this section can be related to the geodetic altimeter as follows: An operating wavelength of the satellite altimeter at X-band (3 cm wavelength) is currently being considered. Kinsman[4] estimates that 80 percent of ocean waves have heights greater than three feet. It therefore seems reasonable to assume that h, the rms wave height, is greater than one-half foot for an appreciable fraction of the time. At X-band the quantity $16\pi^2 h^2/\lambda^2$ has an approximate value of 4×10^3. Most of the contribution to the integral of equation (22) will occur over a range of r from zero to r_1, where r_1 is defined by equation (26). Thus $\rho(r)$ is found to have a value of 0.999. Over this range it appears reasonable to approximate $\rho(r)$ by equation (25) since the change in $\rho(r)$ is small from r = 0 to r_1. On the other hand, if the operating wavelength were 75 cm (400 MHz) the term in equation (26)

$$\left(\frac{4\pi h_o}{\lambda} \right)^2 = 6.4$$

with the result that the correlation function for the same range of r would decay to a much smaller value ($\rho(r_1) = .375$).

Therefore, at 400 MHz one would not expect that $\rho(r)$ could be well represented by a simple quadratic. It is concluded that the backscattered power would not exhibit a simple slope dependence at 400 MHz if the wave heights were only one-half foot rms. At X-band, however, for the same wave, the backscattering cross-section at normal incidence can be accurately

related to inverse mean-square slope.

4.7 ANALYSIS OF WAVE HEIGHT EFFECTS ON THE ALTIMETER WAVEFORM

The extent to which mean-sea-level measurements derived from an electromagnetic signal depart from true mean-sea-level is presently unknown. If this type of bias is not a significant error source in the altimeter data, then estimation of sea state characteristics can be considered as an elective requirement in the altimeter program. Otherwise, wave height estimation is essential in the satellite. The problem of bias in the mean-sea-level measurement is discussed below.

An extension of the work of Rice and Longuet-Higgins has been formulated. In the one-dimensional case, the distribution of reflecting points F(z) on a rough surface of height variable z is

$$F(z)dz = \frac{1}{n} \int p(z,z',z'')|z''|dzdz''$$

where p is the joint probability of the density of the function z and its derivatives (primed) and n is the normalization term. In order to specify that a point on a rough surface constitutes a normal incidence reflection zone, the first derivative of the height variable z' must be equal to zero (e.g. a critical point) and the second derivative z" must be within the required curvature range.

In order to proceed with the mathematical development, it is necessary to assume Gaussian statistics. The approach is discussed in Appendix D. The degree to which the Gaussian assumption holds is unknown. Figure 4.1 shows measured probability distributions of the ocean surface for the height variable and its slope z'. Note that the slope distribution departs much more from a Gaussian statistic than does the height variable. It is in fact possible for the height distribution to be symmetrical and for the slope and curvature distributions to be skewed. In this case, the radar-measured mean-sea-level would certainly depart from its true value.

It is difficult to pursue this theory because of the above-mentioned lack of oceanographic data. The principal oceanographic unknowns involve the high frequency behavior of the slope and curvature spectra. With data presently available, convergence of the spectrum interval is not even assured.

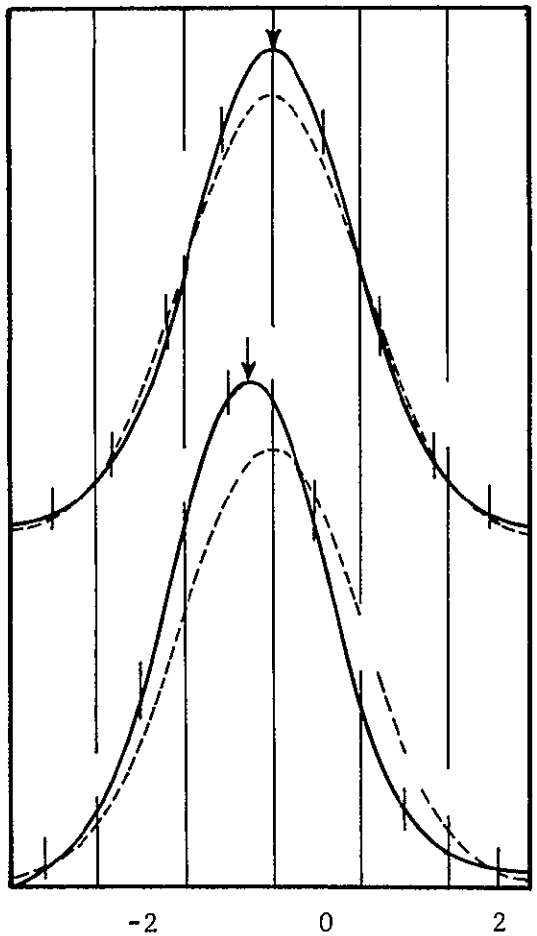

Crosswind (upper) and upwind (lower) components of slope. Solid curve- measured, dashed curve- gaussian. From Cox and Munk

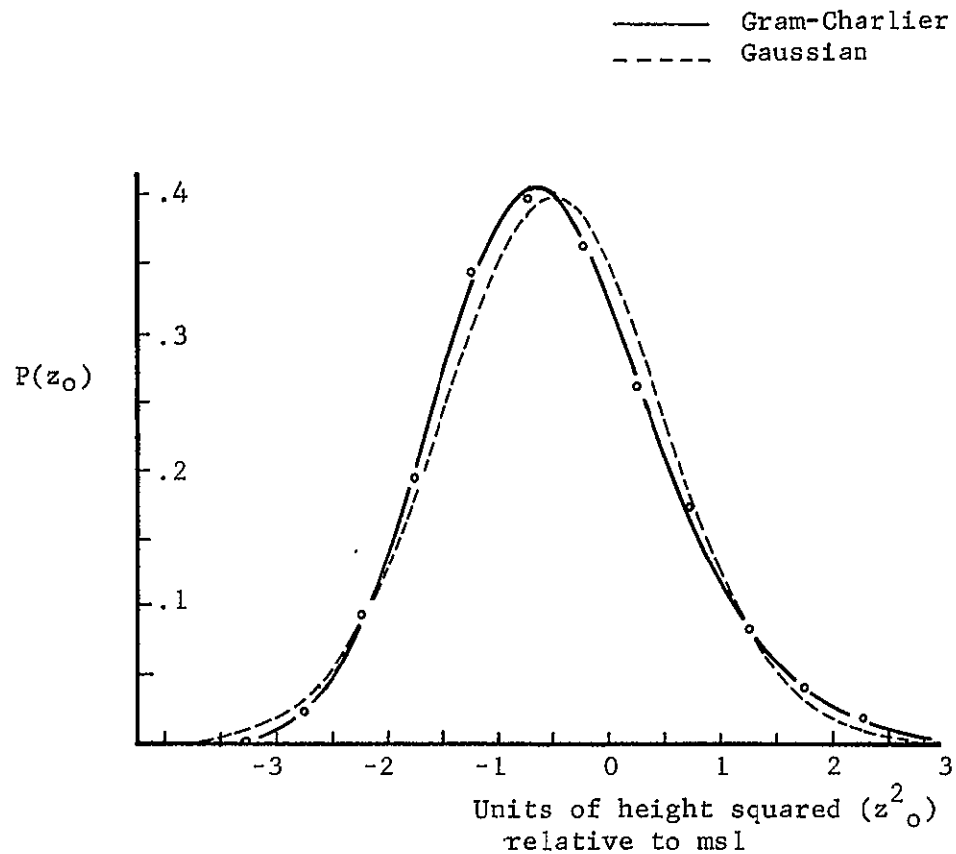

Fig. 4.1. Comparison of measured height and slope distributions with gaussian curves

Because of the assumptions required in a mathematical formulation, it is desirable to examine the bias problem using actual ocean height profiles in a numerical evaluation of the integration. Any errors that may be introduced by the simpler models and assumptions could then be evaluated. Such data can apparently be obtained from laser profilometer measurements and this information would permit completion of the wave model task. Studies could then be conducted to determine (1) feasibility of wave height extractions in the leading portion of the altimeter signal and (2) importance of "sea-state bias".

Section 4

References

[1] Barrick, D. E., "A More Exact Theory of Backscattering from Statistically Rough Surfaces," The Ohio State University Research Foundation, Report No. 1388-18, August 1965.

[2] Hagfors, T., "Backscatter from an Undulating Surface with Applications to Radar Returns from the Moon," J. Geophysical Research, Vol. 69, No. 18, 1964, pp. 3779-3784.

[3] Fung, A. K., and R. K. Moore, "Effects of Structure Size on Moon and Earth Radar Returns at Various Angles," J. Geophysical Research Vol. 69, No. 6, March 1964, pp. 1075-1081.

[4] Kinsman B., Wind Waves, Prentice Hall, Englewood Cliffs, N. J., 1965.

[5] Munk, W. H., "High Frequency Spectrum of Ocean Waves," J. Marine Research, Vol. 14, No. 4, 1955, pp. 302-314.

[6] Research Triangle Institute, "A Review of Electromagnetic Scattering From the Ocean Surface" Report on Contract NASw 1909, September 1969.

[7] Cote, L. J. et al, "The Directional Spectrum of a Wind Generated Sea as Determined from Data Obtained by the Stereo Wave Observation Project," Meteorol. Papers, NYU, College of Engineering, 2(6) 88 pp. (1960).

SECTION 5

OCEANOGRAPHIC STUDY

5.1 SUMMARY AND CONCLUSIONS

In the course of investigating the effects of mean wave-height and spectral anisotropy on the scattering of electromagnetic waves, a number of oceanographic information deficiencies were encountered. The work reported in this section was undertaken as a means of providing statistical characteristics of the ocean surface for use in the work reported in the previous section. This section, therefore, contains a review of prior oceanographic investigations in regard to the dependency of surface characteristics on oceanographic and meteorological parameters.

The general conclusions reached in this section are as follows:

(1) The ocean wind waves are probably generated by the resonance mechanism proposed by Phillips, but their subsequent growth is supported by Miles' shear flow model. In addition to the wind, there are other modification mechanisms, such as wave-wave, and wave-turbulence interactions, etc., that will change the form and pattern of the wind waves.

(2) Because of the favored direction and the modification mechanisms in the wave motion, the statistical distribution of the surface displacement and surface slope are significantly skewed.

(3) By the predominant wind force on waves, the main energy containing part in the two-dimensional wave spectrum is also skewed. In other words, the wave field itself might very well be homogeneous but definitely anisotropic. The anisotropy might be gradually smoothed by the modification mechanisms, especially at high frequencies, and become small but it would never be completely eliminated.

Conclusions specifically relating to the integrated one-dimensional spectrum are as follows:

(1) For a well-developed sea, the spectral form of the high frequency range changes inversely as the fifth power of frequency, or inversely as the fourth power of wave number.

(2) The spectral maximum occurs at a frequency n_o which is equal to the gravity term divided by wind velocity. For most practical purposes, n_o could be used as the cutoff frequency at the lower end of the equilibrium range.

(3) The variance of surface slope, $(\overline{\nabla\zeta})^2$ is logarithmically related to surface wind speed. The dependence of $(\overline{\nabla\zeta})^2$ on fetch and duration is critical only for a short distance or time period respectively.

(4) With moderate to strong winds (< 40 knots), the relation between $(\overline{\nabla\zeta})^2$ and wind speed offers a good method of determining one if the other is known. For wind speeds of 40 knots or less, their relationship is reasonably well established. At higher wind speeds the relationship has not been verified.

5.2 BACKGROUND

The relationship between wind and waves has been obvious, even to casual observers, since time immemorial. Early field and laboratory studies provided generally unrelated information and hypotheses. The fact that the randomness and irregularity of ocean wind waves defied description by the earlier investigators led Rayleigh to write: "The basic law of the Seaway is the apparent lack of any law." With the turning of the century, and especially within the last thirty years, statistical theory began to find its way into applications[1]. The publications of Longuet-Higgins[2] and Pierson[3] began a new era in ocean wind wave study.

From the statistical theory, oceanographers learned that in the study of random wind waves only the various statistical measures of the motion can be regarded as significant observationally, or as predictable theoretically. The fundamental measure of an unknown random wave field is, of course, the joint probability density of the variables. The second moment of this probability density is of central importance because the Fourier transform of it gives the wave energy spectrum which measures the energy contained in a particular wave field. The wave energy spectrum is of prime importance since it is readily measurable. Naturally, the study of the wave energy spectra has become one of the central problems of oceanography.

In the ocean, most, if not all, of the energy of the waves comes from wind. However, the detailed physics involving the energy transfer between wind and waves is still not completely known, in spite of the important works of Phillips[4-6] and Miles[7-10]. Numerous observations and theoretical studies have revealed some definite statistical properties which represent at least part of the whole story, and valuable working relationships between some of the salient parameters involved. In order to serve the immediate purpose, the properties of the high frequency end of the spectrum will be examined first. Although the high frequency waves contain a very limited amount of energy, sea surface slope is strongly dependent upon them. Knowledge of the surface slope-wind relationship could provide the basis for new measurement techniques (Hulburt,[11] Schooley,[12] Cox and Munk[13-14] Cox,[15] and Stilwell[16]).

The following is a review of what is known about the statistical properties at the high frequency end of the wave spectrum (known as the equilibrium range), and one aspect of their application.

5.3 THE EQUILIBRIUM RANGE OF THE SPECTRUM

The notion of an equilibrium range of a spectrum was first advanced by Kolmogoroff[17-18] in the study of turbulence. A similar idea was applied in an ocean wave study by Phillips[19]. The basic concept of an equilibrium range is the same both in turbulence and ocean waves, although the physical processes involved are quite different.

It is observed that as a turbulent wind blows across an ocean surface, energy is continuously transferred to the sea, resulting in wave development. If the duration of the wind is sufficient, some components of the waves presumably will continue to grow, while others, especially the high frequency ones, will reach a state of saturation--limited by instability in the form of breaking. The limiting configuration of a progressive wave was studied by Stokes[20]. He found that when the crest angle reached 120°, the acceleration of a fluid particle at the crest was equal to one half the acceleration of gravity, and at this point the crest, or top of the wave, would break off. Subsequent observations by Gaillard[21] confirmed Stokes' calculation. Ocean waves, however, are irregular with components in many directions and of different frequencies and wave lengths. Breaking may occur: 1) under the same conditions as described by Stokes; 2) when two crests of the wave pattern run together; 3) when a wave moves into a region of high energy density; or 4) when short waves riding over the crest of longer ones have an energy excess as a result of the radiation stress[22-23]. At any rate, it might be reasonably asserted that the wave breaks at some locality when the fluid particles have an acceleration comparable to the acceleration of gravity (g). Energy is dissipated during breaking and at the same time supplied continuously from the wind. At some point, the amount of energy supplied just equals the amount dissipated and the equilibrium state is reached. Under this assumption, Phillips[19], using dimensional analysis, defined the functional form of the frequency spectrum for the equilibrium range:

$$\phi(n) = \beta g^2 n^{-5}; \qquad n_\gamma >> n >> n_o \tag{1}$$

where $\phi(n)$ is the frequency spectrum, β is a constant, n is frequency in cps, n_o is the frequency at the spectral maximum in cps, and $n_\gamma = (\frac{4g^3}{\gamma})^{1/4}$ is the typical frequency for capillary waves.

Similarly, the wave number spectrum $\psi(k)$ is given as:

$$\psi(\underline{k}) = (\frac{B}{\pi})k^{-4} ; \qquad k_\gamma >> k >> k_o \tag{2}$$

where B is a constant containing the angular dependency, k_o is the wave number at the spectral maximum, and $k_\gamma = (\frac{g}{\gamma})^{1/2}$ is <u>the typical wave number of capillary waves</u>.

Various observational results suggest that there is indeed a certain range similar to Phillips equilibrium range. Empirical functions fitted to the observation indicate a dependence of the -5 power of n or -4 power of k. A summary of the dependence of the spectrum on frequency and the values of the constant, β, are given in Table 5-1.

Table 5-1. Observed Values of Equilibrium Range Constants.

Observers	Spectrum $\beta g^2 n^{-S}$		Fetch
	β	S	
Barnett and Wilkerson (1968)[27]		4.95	0-400 km
Burling (1959)[28]	1.48×10^{-2}	5.5	500-100 m
Hicks (1960)[29]	1.21×10^{-2}	4.9	16-300 m
Kinsman (1960)[30]	1.04×10^{-2}	4.5	1,700-3,000 m
Kitaigorodskii (1962)[31]	0.65×10^{-2}	5.5	
Pierson (1962)[32]	1.33×10^{-2}	-5	300 km
Longuet-Higgins, et al. (1963)[33]	$.80 \times 10^{-2}$	-5	500 km

For frequencies or wave numbers greater than n_γ or k_γ respectively, the capillary force would become dominant rather than gravitational force. The breaking of capillary waves was studied by Crapper[24] and Schooley[25]. In spite of the different physics involved, the same similarity theory still applies. Phillips[26] obtained

$$\phi(n) = \beta'\gamma^{2/3}\, n^{-7/3}; \quad n_\gamma << n << n_\nu \tag{3}$$

$$\psi(k) = \left(\frac{B'}{\pi}\right) k^{-4}; \qquad k_\gamma << k << k_\nu \tag{4}$$

where β' and B' are constants, n_ν and k_ν are the cut-off frequency and wave number, respectively, at which viscous forces become important. Observations in the capillary wave range are scarce, but Cox[15], Hidy and Plate[34], and Volkov's[35] observations give some evidence of the validity of the relationship.

A few words of caution must be added here regarding the use of the equilibrium range concept. First, the proposed spectrum function represents the magnitude of wave spectrum only for a well-developed sea when energy becomes saturated over a wide range of wave numbers, or frequencies, manifested by the occurrence of fairly sharp wave crests and intermittent white caps. The sea under this condition is, presumably, statistically stationary. During active development or decay, the above relationships are not valid. The proposed spectrum, then, can be regarded as representing the upper limit of the magnitude of the wave spectrum in these transient states. Fortunately, the transient period (or distance) is not very long and a quasi-stationary state can be realized within hours with wind speeds of 30 to 40 knots or less, or a fetch of approximately 200 km.

Secondly, the cutoff frequencies of the spectrum are dictated at the higher end by capillary forces (in the case of gravity wave spectrum) and viscous forces (in case of capillary wave spectrum). At the lower end the cutoff frequency is less definite. However, by considering the development of the wind wave spectrum (Phillips[6,36,37]), the spectrum can be taken for most practical purposes as the frequency (or wave number) of the spectral maximum. The spectral maximum should occur, according to Phillips' resonance theory[4,5,26,6] at the frequency or wave number having the following relation

$$n_o \propto \underset{\sim}{k}_o \cdot \underset{\sim}{U} \tag{5}$$

where n_o and $\underset{\sim}{k}_o$ are at spectral maximum, and $\underset{\sim}{U}$ is the wind velocity. Using the relationship between n and k; i.e. $\underset{\sim}{n}^2 = gk$, then

$$gk_o = n_o^2 \propto k_o^2 U^2. \tag{6}$$

Hence

$$k_o \propto \frac{g}{U^2}$$

or

$$n_o \propto \frac{g}{U} \tag{7}$$

This theoretical result was subsequently confirmed by the observations of Kitaigorodskii[38], Moskowitz[39], Pierson[40], and Volkov[35]. Pierson's[40] results are summarized in Table 5-2.

Table 5-2. Some Characteristics of Pierson's (1959) Spectrum.

	U^* cm/sec	t hrs.	f max.	U^*fmax/g
1	110	10.5	0.11	0.012
2	106	13.5	0.11	0.012
3	148	10.5	0.08	0.012
4	148	13.5	0.08	0.012
5	143	16.5	0.07	0.011
6	175	14.5	0.07	0.012
7	171	17.5	0.06	0.011

NOTES: 1. U^* is the frictional velocity; it could be related to U, the wind speed, directly. See for example Pierson and Moskowitz[41].
2. t = duration of wind action.

Besides these observations, there are other attempts to develop an empirical expression for the wave spectrum function. Among the better

known earlier ones was that due to Neuman[42], who proposed the following expression using wind velocity as a parameter:

$$\phi(n) = cn^{-6} \exp \{ \frac{2g^2}{n^2 U^2} \} \tag{8}$$

Aside from other objections, the inconsistency of the dimensionality makes it unlikely that it is representative of a genuine physical law. Numerous other attempts have been made by Bretschneider[43,44], Burling[28], and Darbyshire[45,46], to cite a few. But at that time the inclusion of such a parameter as wind velocity by curve-fitting based on limited data seems premature at best.

No major breakthrough was reported until Kitaigorodskii and Kitaigorodskii and Strekalov[38,47] published their findings. Kitaigorodskii[38] assumed that the energy containing part of the wave spectrum is a function of only four variables; i.e.

$$\phi(n) = F(n,g,U_*,X) \tag{9}$$

where U_* = frictional velocity = $(\frac{\tau_o}{\rho})^{1/2}$ and X = fetch.

Then by dimensional analysis, Kitaigorodskii obtained the expression

$$\phi(n) = g^2 n^{-5} F_1 (\frac{U_* n}{g}, \frac{gX}{U_*^2}). \tag{10}$$

When the expression $F_1 (\frac{U_* n}{g}, \frac{gX}{U^2})$ is normalized it does indicate that $\frac{\phi(n)\, n^5}{g^2}$ approaches a constant value. Later, Pierson and Moskowitz[41] made a slight modification of Kitaigorodskii's expression by simply changing frictional velocity, U_* to wind velocity, U, and arrived at the expression:

$$\phi(n) = \alpha \frac{g^2}{n^5} e^{-\beta(\frac{n_o}{n})^4} . \tag{11}$$

where α , β are dimensionless constants, n_o is the frequency at spectral maximum and is equal to $\frac{g}{U}$. In both cases, $\phi(n) \rightarrow dg^2 n^{-5}$ as $n >> n_o$. This conclusion gives considerable support to the Phillips equilibrium range theory.

5.4 SLOPE SPECTRUM

Similar to the energy spectrum discussed in the last section, other spectral functions may also exhibit an equilibrium range. Considering the frequency spectrum of the surface slope $[S_{\alpha\beta}(n)]$ at a fixed point, as an example, Phillips[50] obtains

$$S_{\alpha\beta}(n) = \frac{2}{\pi} \int_o^\infty \frac{\partial\zeta(\underline{x}.t')}{\partial x_\alpha} \frac{\partial\zeta(\underline{x}.t' + t)}{\partial x_\beta} \cos nt \, dt \tag{12}$$

where x_α, x_β are the horizontal vector components and ζ is the surface elevation. In the equilibrium range, by dimensional analysis,

$$S_{\alpha\beta}(n) = c_{\alpha\beta} n^{-1}, \qquad n_\gamma >> n >> n_o \tag{13}$$

where $c_{\alpha\beta}$ is a constant tensor. Under the assumption of statistical symmetry with respect to the wind direction, $c_{\alpha\alpha}$ was determined to be[33]

$$c_{\alpha\alpha} = c_{11} + c_{22} = 0.8\text{x}10^{-2} \tag{14}$$

In the capillary range,

$$S_{\alpha\beta}(n) = c'_{\alpha\beta} n^{-1}, \; n_\gamma << n << n_\nu \tag{15}$$

and $c'_{\alpha\beta}$ is not necessarily equal to $C_{\alpha\beta}$. An experimental study by Cox[15] gives some support to the prediction.

Since the slope spectrum is derived from the product of derivatives of the surface elevation, the relationship between them can be shown schematically as in Fig. 5.1. Accordingly, the variance of surface slope is given by

$$\overline{(\nabla\zeta)^2} = \int_{\underset{\sim}{k}} k^2 \, \psi(\underset{\sim}{k}) \, d\underset{\sim}{k}$$

$$= \int_n \frac{n^4}{g^2} \, \phi(n) \, dn \tag{16}$$

Equation (16) shows that the contribution to $\overline{(\nabla\zeta)^2}$ is heavily weighed by the factor k^2 or n^4 in the integrand. Thus a major contribution comes from the high frequency (or wave number) end where a negligible amount of energy is contained. However, due to the results of recent research in optical methods by Schooley[12], Cox and Munk[13,14], Cox[15], Stilwell[16] and in radar devices by Barnett and Wilkerson[27], both using the surface reflections, the importance of the study of surface slopes has markedly increased. In the following section an important application is presented.

5.5 THE RELATIONSHIP BETWEEN MEAN SQUARED SLOPE AND SURFACE WIND SPEED

In the first attempt to optically study ocean surface slopes, Hulburt[48], using sun glitter, concluded that the reflecting facets of the sea surface occured most frequently at about 15°. No direct relationship between the wind vector and $(\nabla\zeta)^2$ were found, but it was stated clearly that the wind was the major cause of the change of $\overline{(\nabla\zeta)^2}$.

Twenty years elapsed before Cox and Munk[13,14,48] Schooley[12], and Cox[15] conducted another series of experiments. The principle used in all the

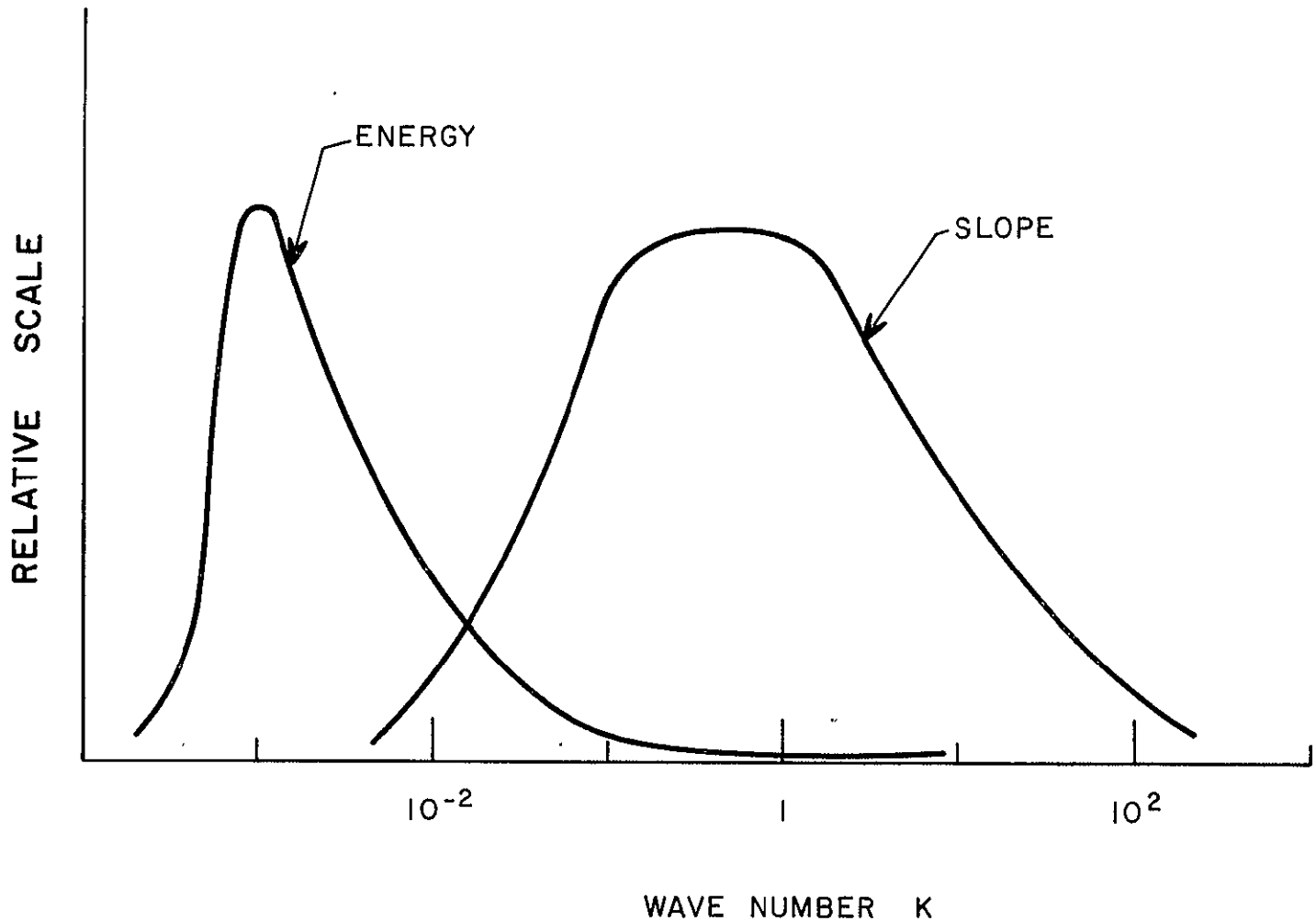

Fig. 5.1. Sketch of Elevation (Energy) and Slope Spectral Distributions

optical measurements of the surface slope was the same, but the importance of the latter studies lay in a proposed relationship between $\overline{(\nabla\zeta)^2}$ and the surface wind.

Schooley[12] used flash photography taken from a bridge. He made no serious attempt to find an empirical formula to describe the observations. At about the same time period, Cox and Munk[13,14,18] studied sun glitter photos taken from an airplane. The cases of a clean surface and a surface covered with artificially induced oil slicks were both studied. Their extensive measurements led them to claim that $\overline{(\nabla\zeta)^2}$ varied linearly with wind velocity. In an attempt to lend more support to their curve fitting result, Neuman's spectrum was used to calculate the relationship approximately. From the calculation, a linear relationship between $\overline{(\nabla\zeta)^2}$ and U was indeed obtained. However, since Neuman erroneously used $\phi(n) \propto n^{-6}$ for high frequency, the value of the calculation and the result are questionable.

Later Cox[15] made a laboratory study and concluded that the relationship was not a simple linear one. Furthermore, the value becomes independent of fetch after a short critical distance. These findings are in general agreement with Phillips' equilibrium range theory.

Since Phillips' equilibrium range theory is consistent with numerous independent observations it was used to derive a relationship between $\overline{(\nabla\zeta)^2}$ and U. As discussed in Section 4.3, the cutoff wave number could be taken as k_c and $k_o \simeq \frac{g}{U^2}$. Then

$$\overline{(\nabla\zeta)^2} = \int_{\underset{\sim}{k}} k^2 \; (\underset{\sim}{k}) \; d\underset{\sim}{k} \simeq \int_{k_o}^{k_c} k^3(k) \; dk = B \log \left(\frac{k_c}{k_o}\right) \tag{17}$$

If k_c is much less than the capillary wave range; i.e. $k_c << k_\gamma = \left(\frac{g}{\gamma}\right)^{1/2}$, then

$$\overline{(\nabla\zeta)^2} = B \log \left(\frac{k_c U^2}{g}\right). \tag{18}$$

However, if k_c is within or greater than the capillary wave range then

$$\overline{(\nabla\zeta)^2} \simeq B' \log \left(\frac{k_c}{k_\gamma}\right) + B \log \left(\frac{k_\gamma}{k_o}\right) \tag{19}$$

When these calculations are plotted together with data from Cox[15] and Cox and Munk[13,14,48] for the case of an oil slick which filtered out almost completely waves with length less than 30 cm. the Phillips calculation shows remarkable agreement. For the case with capillary components, the agreement becomes less as wind velocity increases. This could be due to the difficulty in measurement of $\overline{(\nabla\zeta)^2}$ as reported by Cox and Munk.

Using Pierson's[41] spectrum and integrating from $n_o = \frac{g}{U}$ to some frequency n, with the help of the dispersive relationship, gk = n, then

$$\begin{aligned} \overline{(\nabla\zeta)^2} &= \int_{n_o}^{n} \frac{\alpha g^2 \omega^4}{\omega^5 g^2} e^{-\beta\left(\frac{n_o}{\omega}\right)^4} d\omega \\ &\simeq \frac{\alpha}{2} \left[\ln \frac{U^2 k}{g} - \frac{\beta}{2} + \frac{\beta}{2} \frac{k_o^2}{k^2}\right] \end{aligned} \tag{20}$$

This is of the same function form as (18). Since Pierson's formula applies only to gravity waves, its usefulness is limited.

The relation between $\overline{(\nabla\zeta)^2}$ and U seems to be well defined both experimentally and theoretically; however, the application of this relationship is not without difficulty, especially when the wind velocity becomes very high (40 knots or higher). The difficulties are twofold. First, as the wind increases, the stability of the wave is controlled not only by breaking but also by blow-off from the crest. The validity of Phillips' equilibrium range theory under this condition has not been carefully studied. Secondly, with increased breaking of the energy-saturated waves, optical observation becomes more and more difficult. White-caps tend to result in an over-estimation of the surface

slope[13]. This, however, could be overcome by improving measuring techniques. (Clearly, the radar technique is a promising one.)

5.6 DIRECTIONAL CHARACTERISTICS OF OCEAN WAVE SPECTRA

Based upon the statistical approach to ocean wave study, the free surface is represented as a sum of independent components of sinusoidal waves of different amplitudes, phases, and directions of propagation. The mathematical ideas involved in this representation are simple enough, yet the inverse of the problem; i.e., to find those components which accurately represent the random wave field, poses an extremely difficult task for oceanographers. This, in essence, is the problem of finding a two-dimensional wave spectrum for a random wave field.

The difficulties encountered in the measurement techniques necessary to obtain good two-dimensional spectra remain almost insurmountable. However, the practical need for this information has forced researchers to seek a modus vivendi; i.e., to seek a limited goal of determining a one-dimensional spectrum to represent an integrated effect of the actual two-dimensional phenomenon. This one-dimensional spectrum could be obtained by means of a Fourier analysis of a measurement record at a single point. Even a one-point measurement was difficult to obtain in the deep water a decade or so ago, because of the lack of a working platform.

The information contained in a one-dimensional spectrum is, indeed, valuable as far as the total energy of a given sea state is concerned. However, this information is far from complete. The directionality is necessary not only from the practical aspects of wave prediction, mass transport, impact of waves on coastal structures, etc., but also in the basic study of the detailed physical processes involved in wave generation. The skewness of the surface distribution has important bearings on radar and optical studies of the ocean surface itself.

A reasonably accurate characterization of these parameters has evolved during the last decade through the persistent effort of many researchers. These field studies have gradually revealed the statistical properties of the ocean waves. The purpose of this discussion is to review these efforts, and some of the salient results of the directional statistical properties. These properties can be divided conveniently into two

categories: 1) the probability structure of the ocean surface and 2) the directional distribution of the energy in a two-dimensional spectrum. The first deals with the geometrical shape of individual waves; the second deals with the combined effects of the individual waves upon the wave spectrum.

In order to understand these results, the processes of generation and the mechanisms of modifying the waves will be discussed first. The process of generation of waves on the ocean surface are summarized in the next section.

5.7 THEORY OF WAVE GENERATION BY WIND

The interactions between the atmosphere and the ocean appear in various forms. From the oceanic viewpoint and with the atmosphere as the primary energy source, motion ranging from global circulations to micro-scale turbulence are found. The progress in the study of ocean circulation has been summarized by Stommel[49] and in the study of waves, by Phillips[50]. Only a few years ago, Ursell[51], in a review paper on the theory of wave generation by the wind, stated that all of the three basic elements for determining the mechanism of wave generation were still wanting; namely, a correct theory, a well-documented experimental study, and a demonstration of a good agreement between the two. This pronouncement served as a great stimulation for the study of this problem. Within a year, two independent theories by Phillips[52] and Miles[53] were advanced. Since then, both theoretical and experimental works have resulted in tremendous progress. A brief outline of the theoretical aspect is given below.

Phillips[52,54] postulated the resonance mechanism of atmospheric turbulent pressure and the surface waves. The air flow is always turbulent, the pressure fluctuation in the air is, therefore, random. However, as the turbulent air flows over a random ocean surface, interaction occurs. The fluctuation of the pressure can be separated into two groups. The first consists of the purely turbulent pressure fluctuations whose pattern is everchanging as the eddies in the turbulence grow, interact and decay. The second consists of a spatial pattern of pressure variation that travels over the surface at a pressure pattern convective velocity. The existence

of this latter pattern was confirmed by observations of Willmarth and Wooldridge[55]. To this semi-rigid convecting pressure fluctuation, Phillips assigned a relationship of the same wave number k as the surface waves. The total pressure field thus could be expressed in Fourier-Stieltjes representation as

$$d\hat{\omega}\ (\underset{\sim}{k},t) = (\nu + i\mu)\ \rho\omega c^2 k dA\ (\underset{\sim}{k},t) + d\omega(\underset{\sim}{k},t) \tag{21}$$

where the pressure $p(\underset{\sim}{x},t)$ in the physical space is

$$p(\underset{\sim}{x},t) = \int_{\underset{\sim}{k}} d\hat{\omega}(\underset{\sim}{k},t)\ e^{i\underset{\sim}{k}\cdot\underset{\sim}{x}} \tag{22}$$

and the surface elevation $\zeta(\underset{\sim}{x}\cdot t)$ is

$$\zeta(\underset{\sim}{x}\cdot t) = \int_{\underset{\sim}{k}} dA(\underset{\sim}{k}\cdot t)\ e^{i\underset{\sim}{k}\cdot\underset{\sim}{x}} \tag{23}$$

and $dA(\underset{\sim}{k}\cdot t)$ is the purely random part uncorrelated to surface waves, ν,μ are the coupling coefficients, c is the phase velocity of the surface wave with wave number k, ρ_ω is water density, and k is $|\underset{\sim}{k}|$.

Through the linearized equations of motion, Phillips[4] was able to relate the surface wave spectrum, $\phi(\sigma,\theta)$ to the pressure spectrum $\pi(k,\tau)$ as

$$\phi(\sigma,\theta) \simeq \frac{k^2\sigma t}{2(g\rho_\omega)^2} \int_0^\infty \pi(\underset{\sim}{k},\tau)\ \cos\ [(\frac{U_c\ \cos\ \theta}{c} - 1)\sigma\tau]\ d\tau \tag{24}$$

where τ = time variable, t = duration of wind action, U_c = convective velocity of pressure pattern approximately equal to the mean wind velocity.

There is sufficient evidence to support this theory. First, if there is a rigidly convecting pressure pattern, and if the response mechanism is indeed responsible for the wave generation, then waves of frequency n would be expected to appear in a bimodal distribution in the two-dimensional wave spectrum at angles $\pm\alpha$ dictated by the resonance condition. The resonance condition is

$$n = \underline{k} \cdot \underline{U}_c = \underline{kU}_c\ \cos\ \alpha_m \tag{25}$$

or

$$\alpha_m = \cos^{-1}\left(\frac{c}{U_c}\right) = \cos^{-1}\left(\frac{g}{kU_c^2}\right)^{1/2} \tag{26}$$

Field observation by SWOP[57] indicated that there was indeed a bimodal distribution. Secondly, if resonance did occur, the components of waves grow and the fastest should travel at approximately the same speed as the mean wind, and the initial growth rate should be linear. This is also supported by field observations of Barnett and Wilkerson[27].

Complementary to Phillips' resonance theory, but physically quite different, is the model suggested by Miles[7] and augmented by Brooke Benjamin[58], Lighthill[59] and Phillips[26]. Miles considered shear flow over existing waves. The mechanism involved is the momentum transfer from the perturbed shear flow of the wind to the perturbing waves; therefore, this model depends crucially upon the wind profile over the waves. Based on this physical picture, Miles calculated the flux of momentum from the wind to the waves through a "matched layer", (where $U(z_m) = c$ with $U(z)$ = mean wind velocity, c = phase velocity of the existing waves) as

$$\tau_\omega = \pi\rho_a \left[\frac{\overline{\omega^2}}{k}\left(-\frac{U''}{U'}\right)\right]\Big|_{z=z_m} \tag{27}$$

where ρ_a = air density, $U(z)$ = mean wind velocity profile, and $\overline{\omega^2}$ = mean square vertical induced fluctuation of the air.

Since the energy density E of the wave is related to its momentum M by

$$E = Mc$$

the energy flux formula is

$$E = \tau_\omega c = \pi\rho_\alpha c \left[\frac{\overline{\omega^2}}{k}\left(-\frac{U''}{U'}\right)\right]\Big|_{z=z_m} . \tag{28}$$

Subsequent works of Miles[60] and Phillips[26] uncovered a link between the two different theories. From Miles' model one can calculate the coupling coefficients between air pressure fluctuation and wave as

$$\nu = -\frac{\rho_a k}{\rho_\omega c^2} \int_o^\infty (U \cos \alpha - c)^2 \, e^{-kz} dz \tag{29}$$

$$\mu = \frac{2\tau_\omega(o)}{\rho_\omega c^2 k^2 a^2}$$

Since ν is definitely negative, the surface pressure should be exactly out of phase with the surface elevation. Confirmation by observations were reported by Longuet-Higgins et al[33], and Shemdin and Hsu[61].

From the experimental results, it is believed that both Phillips' and Miles' theories are correct to some extent. Phillips' resonance theory was successful in initiating the wave motion, but it is not an effective mechanism to feed in energy to support the continuous growth. Miles' model, on the other hand, depends upon the pre-existing waves to perturb the shear flow; therefore the trigger mechanism is missing. These short-comings were partly taken care of by subsequent works. Yet, another difficulty of the inability to incorporate the fully turbulent air flow in the theory is still unsolved (see, for example, Phillips[6]). In spite of this, Phillips' and Miles' theories have successfully explained many details in wind wave generation.

5.8 OTHER MECHANISMS OF WAVE GENERATION AND MODIFICATIONS

Of all the factors having dynamical influence on waves, the primary one is, of course, the wind, which is responsible for generation, growth, and even under special condition, decaying of the waves. However, the wind is by no means the only mechanism that has dynamical consequence. Once the energy is fed into the ocean, other processes become dominant such as turbulence resonance and shear flow instability. These processes cannot create energy, but they certainly transfer energy from one form to another. Their results may be shown by a simple change of form of waves, and ultimately change the probability structure. Some of these mechanisms are discussed below.

(a) Wave-Wave Interaction (non-resonant)

This involves the interaction of waves with their own higher harmonics; or in other words, the higher order solutions of the classic

wave equation such as Lamb[62], Pierson[41] and De[63]. The higher order contributions tend to modify the geometry of the wave structures.

(b) Wave-Wave Interaction (non-linear resonant)

While the bounded interaction discussed above only results in the change of waveform, the non-linear resonant interaction changes the wave pattern. It transfers energy from an existing frequency to previously non-existing ones. The mechanism was discovered by Phillips[37] for gravity waves, and then simplified and augmented by Phillips[64,65], Longuet-Higgins[66], Benny[67], Hasselmann[68,69] and Bretherton[70]. A similar resonance phenomenon in capillary waves was discovered by McGoldrick[71]. The mathematical principle of this resonance is simple. Assume systems of interacting waves expressed as

$$\left\{\begin{aligned} \zeta &= \sum_{\gamma=\pm 1}^{\pm n} a_r e^{i\chi_r}; \quad \chi_r = \underset{\sim}{k}_r \cdot \underset{\sim}{x} - n_r t \\ \phi &= \sum_{\gamma=\pm 1}^{\pm m} b_r e^{\underset{\sim}{k}_r z} e^{i\chi_r} + \phi_1(\underset{\sim}{x}\cdot z, t) \end{aligned}\right\} \tag{30}$$

where ϕ_1 is the product of the interaction, ζ is free surface elevation, and ϕ is the velocity potential. Using these expressions in the first and second order equation, we can only get similarly bounded resonance as in part (a). However, when the third order equation is used; i.e.

$$\left\{\begin{aligned} \frac{\partial^2\phi}{\partial t^2} + \frac{g\partial\phi}{\partial z} = -\zeta \frac{\partial}{\partial z}\left(\frac{\partial^2\phi}{\partial t^2} + g\frac{\partial\phi}{\partial z}\right) - \frac{1}{2}\zeta^2 \frac{\partial^2}{\partial z^2}\left(\frac{\partial^2\phi}{\partial t^2} + g\frac{\partial\phi}{\partial z}\right) \\ - \frac{\partial}{\partial t} u^2 - \zeta \frac{\partial^2}{\partial z \partial t} u^2 - \underset{\sim}{u} \cdot \nabla \left(\frac{1}{2} u^2\right) \text{ at } z = 0 \end{aligned}\right\} \tag{31}$$

the interaction of three primary waves of $r = 1,2,3$ will produce a fourth wave of wave number and frequency K_4 and N_4 respectively provide the resonance condition

$$\left\{\begin{array}{l} \underset{\sim}{K}_1 \pm \underset{\sim}{K}_2 \pm \underset{\sim}{K}_3 \pm \underset{\sim}{K}_4 = 0 \\ N_1 \pm N_2 \pm N_3 \pm N_4 = 0 \end{array}\right\} . \tag{32}$$

Quantitative measurements of resonance interacting waves were conducted by McGoldrick et al[72] and Longuet-Higgins and Smith[73]. Their results confirmed Phillips' theory.

In the case of a random ocean where there are infinitely many chances to form the resonant quartets, the interaction mechanism will produce wave components of all wave numbers of small energy density, including, of course, those traveling against the wind.

(c) Scattering of Gravity Waves by Turbulence

Scattering of waves by turbulence has been studied by many authors. Some of the previous works were summarized by Batchelor[74]. The true application to oceanic environment was advanced by Phillips[75]. Physically, it should be fully expected that the presence of random velocity fluctuations in the water of a velocity scale comparable with particle velocity associated with wave motion and a length scale comparable with the wavelength of existing waves will result in the convective distortion of the wavefronts, and so the establishment of a scattered wave field. In the ocean, it is well known that because of wind-induced currents, waves, and wave breakings, turbulence is always present in the surface layer. But the lack of information on the turbulence on the ocean surface layer seriously hampered detailed analysis of the interaction between turbulence and waves. As a result, Phillips was forced to consider only the weakly turbulent case when

$$U_t << c(k) \tag{32}$$

where U_t is the r.m.s. turbulent velocity and $c(k)$ is the phase of the wave of wave number k. Under this restriction, Phillips found that the spectrum of the scattered waves $s(k \cdot \theta)$ will be

$$s(\hat{\underset{\sim}{k}} \cdot \theta) = \frac{\pi k^2}{(gk)^{1/2}} \quad \psi(\overline{\underset{\sim}{K}}) \tag{33}$$

where $\hat{\underset{\sim}{k}}$ is the scattered wave number, k is the incident wave number, $\psi(\overline{\underset{\sim}{K}})$ is the wave number spectrum of turbulence and $\overline{\underset{\sim}{K}}$ is the wave number of turbulence.

Furthermore, the scattering is most effective for a given θ when the scattered wave will have the magnitude of wave number equal to the incident wave.

Unfortunately, due to the difficulty of measurement, no well-documented evidence of any sort could be found either to support or to dispute this result. However, since the physical model used in this analysis is resonable, the analysis is rigorous and there is no reason why the result should fail or change drastically from that predicted even in a strongly turbulent case. Here again a mechanism is present which will produce weak waves traveling against the predominant direction of wind force.

(d) Others

Aside from the mechanisms discussed, other processes such as generation of parasite capillary waves (Longuet-Higgins[76]), short waves on current or riding on long waves (Longuet-Higgins and Stewart[77]), attenuation of waves by breaking (Phillips[78]), second-order resonant interaction between capillary waves (McGoldrick[71]) all contribute to the change of waveform. But since their influence on the directional distribution of energy, or on anisotropic properties of the surface, is much smaller than the others, a detailed summary is omitted.

5.9 PROBABILITY STRUCTURE OF THE OCEAN SURFACE

The ocean surface can be regarded as the sum of a large number of independent wave components of different wave numbers, phases and amplitudes. If the area under consideration is small compared to the generating storm area, its statistical properties could be taken as stationary. Furthermore, by the central limit theorem, the probability distribution of the surface displacement should be Gaussian. Then

$$p(\zeta) = \frac{1}{(2m\overline{\zeta^2})^{1/2}} \exp\{-(1/2)\zeta^2/\overline{\zeta^2}\}. \tag{34}$$

Field observations invariably indicate that to a first-order approximation, the probability distribution is indeed Gaussian as reported by Longuet-Higgins[79,80]. However, because of the favored direction of the wind force, and linear and non-linear wave-wave interaction, skewness is always introduced. Therefore, there are some higher order modifications of the surface. For example, the third-order correction to the Stokes irrotational wave indicates pointedness of the crests. Careful field observation by Kinsman[30] indeed substantiated this prediction. Longuet-Higgins[81] calculated the correction of the distribution from a Gaussian expression and found that the surface elevation could be better approximated by the successive terms of a Gram-Charlier series as

$$p(\zeta) = \frac{1}{(2\,\overline{\zeta^2})^{1/2}} \exp\{(1/2)\ t^2\}\{1 + (1/6)\ \overline{\zeta^3}H_3 + \ .\ .\ .\} \tag{35}$$

where

$$t^2 = \zeta^2/\overline{\zeta^2} \text{ and } H_3 = t^3 - 3t.$$

On the other hand, the non-linear interaction and the favored direction of wind force also changes the surface slope. Although the non-linear effect studied by Phillips[37] and Longuet-Higgins[81] showed that the change in skewness $m_3 = \overline{\zeta^3}/(\overline{\zeta^2})^{3/2}$ was of the same order as the fourth power of surface slope, the wind effect has never been accurately calculated. Detailed field measurements reported by Cox and Munk[13,48] showed the skewness much higher than could be accounted for by non-linear effects alone.

Considering the random wave field as a whole, the cumulative effects of the wind are manifested clearly in the directional energy distribution. Inspection of the two-dimensional energy contours indicates that the direction of wave energy distribution is skewed toward the wind direction. Even at high wave numbers where there is a considerable amount of

scattering and smoothing, the skewness is still obvious.

5.10 METHODS OF MEASURING DIRECTIONAL SPECTRA AND SOME RESULTS

Since oceanographers first adopted a statistical approach to ocean wave study, the effort to actually describe a given random ocean by a complete spectrum has continued. Unfortunately, the task has never been carried out with total success. The difficulty is twofold. Firstly, the difficulty arises from the basic statistical and mathematical tools, borrowed in whole or in part from other fields. Ideally, by the oceanographer's definition, a complete wave spectrum of a given sea state will describe not only the total energy and the directional distribution of energy but, more precisely, the sense of the directional distribution. Secondly, by rigorous spectral analysis, under the assumption of homogeneity, the sense of the directional distribution of energy cannot be determined uniquely. This can be explained as follows. Take the surface elevation at position $\underset{\sim}{x}$, and time t as $\zeta(\underset{\sim}{x} \cdot t)$, then at position $\underset{\sim}{x} + \underset{\sim}{r}$, and time $t + \tau$, we have $(\underset{\sim}{x} + \underset{\sim}{r},\ t + \tau)$. Their correlation function $R(\underset{\sim}{x},t;\ \underset{\sim}{r},\tau)$ is

$$R(\underset{\sim}{x},\ t;\ \underset{\sim}{r},\tau) = \overline{\zeta(\underset{\sim}{x},t)\ \zeta(\underset{\sim}{x} + \underset{\sim}{r},\ t + \tau)} \tag{36}$$

Under the homogeneity assumption, the correlation function $R(\underset{\sim}{x},t;\ \underset{\sim}{r},\tau)$ should be independent of the origin of the coordinate system, therefore $R(\underset{\sim}{x},t;\ \underset{\sim}{r},\tau)$ reduces to $R(\underset{\sim}{r},\tau)$. By a simple translation of coordinates in space and time,

$$R(\underset{\sim}{r},\tau) = R(-\underset{\sim}{r},\tau) = R(\underset{\sim}{r},-\tau) = R(-\underset{\sim}{r},-\tau) \tag{37}$$

i.e. $R(\underset{\sim}{r},\tau)$ is an even function with respect to both $\underset{\sim}{r}$ and τ.

Now since the spectrum function $\psi(\underset{\sim}{k},n)$ is defined as

$$\psi(\underset{\sim}{k},n) = \int_{\underset{\sim}{r}} \int_{\tau} R(\underset{\sim}{r},\tau)\ e^{i(\underset{\sim}{k}\cdot\underset{\sim}{r}-n\tau)}\ d\underset{\sim}{r}\ d\tau \tag{38}$$

note that $\psi(\underset{\sim}{k},n)$ has to be an even function with respect to $\underset{\sim}{k}$ and n. In other words, there is no difference between

$$\psi(\underset{\sim}{k},n) \text{ and } \psi(-\underset{\sim}{k},-n) \text{ or } \psi(-\underset{\sim}{k},n).$$

Therefore, strictly speaking, we can get only directional information which does not include the sense of the direction from traditional spectral analysis. Of course, it must be understood that the ambiguity occurs only when the homogeneity assumption is used, but whether this assumption really holds is not known exactly. However, without this assumption, or if the condition of homogeneity does not exist, then the data collected would be representative of that particular place and time. At any rate, the information contained in this conventional spectral analysis is not complete. In order to resolve this dilemma of the π ambiguity under the homogeneity assumption, additional physical information has to be added independently to the spectral analysis to specify the exact direction and sense which is essential to the oceanographer's definition of a complete directional spectrum. In simple cases such as in the study of swell or of waves with well-defined crest lines, this additional physical information is easy to obtain. However, in complicated random wave fields, where individual waves are difficult to follow, the true direction of the wave propagation can be known only if a complete time history of the whole wave field is known. None of the measurement techniques developed to date will provide the required information.

In spite of this difficult problem, some observations have been made, limited, of course, by practicality and loaded with assumptions and approximations. The following is a summary of the methods used and results obtained.

(a) Stereo Photography

A photographic record of the instantaneous state of the sea will undoubtedly contain the necessary information needed for determining the directional spectrum. This idea was first used by Barber[82] to obtain a qualitative estimation of the directional spectrum. Later the New York University group embarked on an extensive stereo

wave observation project[57] and produced a series of complete evaluations of directional spectra (reported by Cote et al[83] and U'beroi[84]). Despite the considerable trouble taken, the results obtained were not the real directional spectrum, but instead $[\phi(\sigma,\theta) + \phi(\sigma,\theta + \pi)]$, because of the built-in ambiguity of π in the spectrum analysis. This forced the investigators to assume that the energy distribution was confined between $(\pi/2,-\pi/2)$. This assumption easily solved the directional ambiguity, and could be accepted as a first approximation for the energy containing range. Unfortunately, in the light of the wave modification mechanisms previously discussed, a fraction of waves with small, albeit non-zero amounts of energy at high wave number can propagate against the mean wind. In addition, there even exists the possibility of residual low wave number swells coming from other possible directions including the one against the wind. Though their omission might not be crucial in energy considerations, the high wave number part is important in determining the slope and curvature spectrum of the sea; therefore, the result obtained by limiting the energy contained between $(\pi/2,-\pi/2)$ is of questionable quality.

(b) Directional Array of Probes

The idea of using a linear array of probes for directional wave measurement was suggested by Barber[85,86], but the only example of measurement was for a single band of frequencies. The same idea was later picked up by Konyayev and Dreyer[87] and Dreyer and Konyayev[88], but the results so far are still qualitative.

A slight alteration of this linear array of probes was to arrange the probes at the vertex of a triangle. This was tried by Munk et al[89] in observing long swells, and by Tsyplukhin[90] in observing near shore shallow water waves. In both cases, the waves were relatively simple with the fixed direction of propagation; therefore, the results were not representative of a truly random wave.

Krylov et al[91] used the same setup of Tsyplukhin in relatively deep water to obtain information on the angular energy spectrum which is defined as

$$\phi(\theta) = \int_{\sigma} \psi(\sigma,\theta)\, d\sigma \tag{39}$$

where $\phi(\sigma,\theta)$ is the two-dimensional spectrum. They found that the best fit directional angular spectrum is a cosine power law such as

$$\phi(\theta) \;\alpha\; \cos^2 (\theta - \alpha) \tag{40}$$

where α is the principal direction of the spectrum. Later, Drylov et al[92] proposed an empirical formula for the directional spectrum;

$$\psi(\sigma,\theta) = \frac{\overline{\zeta^2}\,\tau_o}{2\pi} \{\frac{0.32}{\sigma^6} (\cos\theta)\, \frac{1.8}{\sigma} \exp\,(- \frac{0.8}{\sigma^4})\} \tag{41}$$

where τ_o is the average period. Comparison with observation is favorable, but compared to Phillips' equilibrium range theory[19] the dependence of $1/\tau_o$ coupled with the inconsistency of dimensionality in the expression itself would undoubtedly limit its usefulness.

The idea of using the probe array method is theoretically sound but impractical unless stable working platforms and large numbers of densely deployed probes become easily accessible in deep water; this severely limits its usefulness.

(c) Buoy Techniques

This idea was also first suggested by Barber[82], but subsequently developed by Longuet-Higgins[2] and put in practice by an NIO group. The instrumentation, measuring process and results were reported by Longuet-Higgins[80], Longuet-Higgins et al[93], Cartwright and Smith[94] and Erwing[95]. The principle involved using the freely floating buoy to measure ζ, $\partial\zeta/\partial x$ and $\partial\zeta/\partial y$ by gyroscopes, then relate these quantities to the first five Fourier components of the spectrum function. In this conversion, different combinations of coefficients will produce slightly different results, with the same effect as using different weighting functions in averaging, but comparisons with the data suggested that cosine power laws gave the best fit. The results so obtained are the most detailed and complete to date. Some of them are

rendered in contour diagrams in Figs. 5.2, 5.3, and 5.4.

Several points should be brought up here. First, an interesting comparison with theoretical prediction on resonance angle could be made here. Consider the integral

$$I = \frac{1}{2\pi} \int 16 \sin^2 \frac{\theta-\theta_1}{2} \sin^2 \frac{\theta-\theta_2}{2} \psi(\sigma,\theta)\, d\theta \tag{42}$$

with θ_1,θ_2 = arbitrary fixed angles. We can find a set of θ_1,θ_2 for each given $\psi(\sigma,\theta)$ to minimize I. It can be shown that

$$\overline{\theta} = 1/2(\theta_1 + \theta_2)$$

is approximately the main direction of the spectrum, while

$$\psi = 1/2(\theta_1 - \theta_2)$$

is approximately the r.m.s. angular width of the energy distribution. Comparison of ψ with Phillips' resonance angle shows the experimental points are low but not inconsistent with the theoretical result. Secondly, there is no clear bimodal distribution of energy, instead the best approximation is a cosine power law as

$$\phi(\sigma,\theta) \propto (\cos 1/2\theta)^{2s} \tag{43}$$

where s varies with frequency. This power law dependency was reported both by Longuet-Higgins et al[93] and by Krylov et al[91,92] through different methods of measurements. From the form of Longuet-Higgins' expression, it can seem that as s decreases so does the dependence of ϕ on θ. For a special case of s = 0, the distribution of energy will be isotropic. At high frequencies the value of s is indeed very small. Therefore, the angular range of energy distribution could be expected to be fairly wide. A word of caution should be added. Although both Longuet-Higgins and Krylov suggested the cosine power

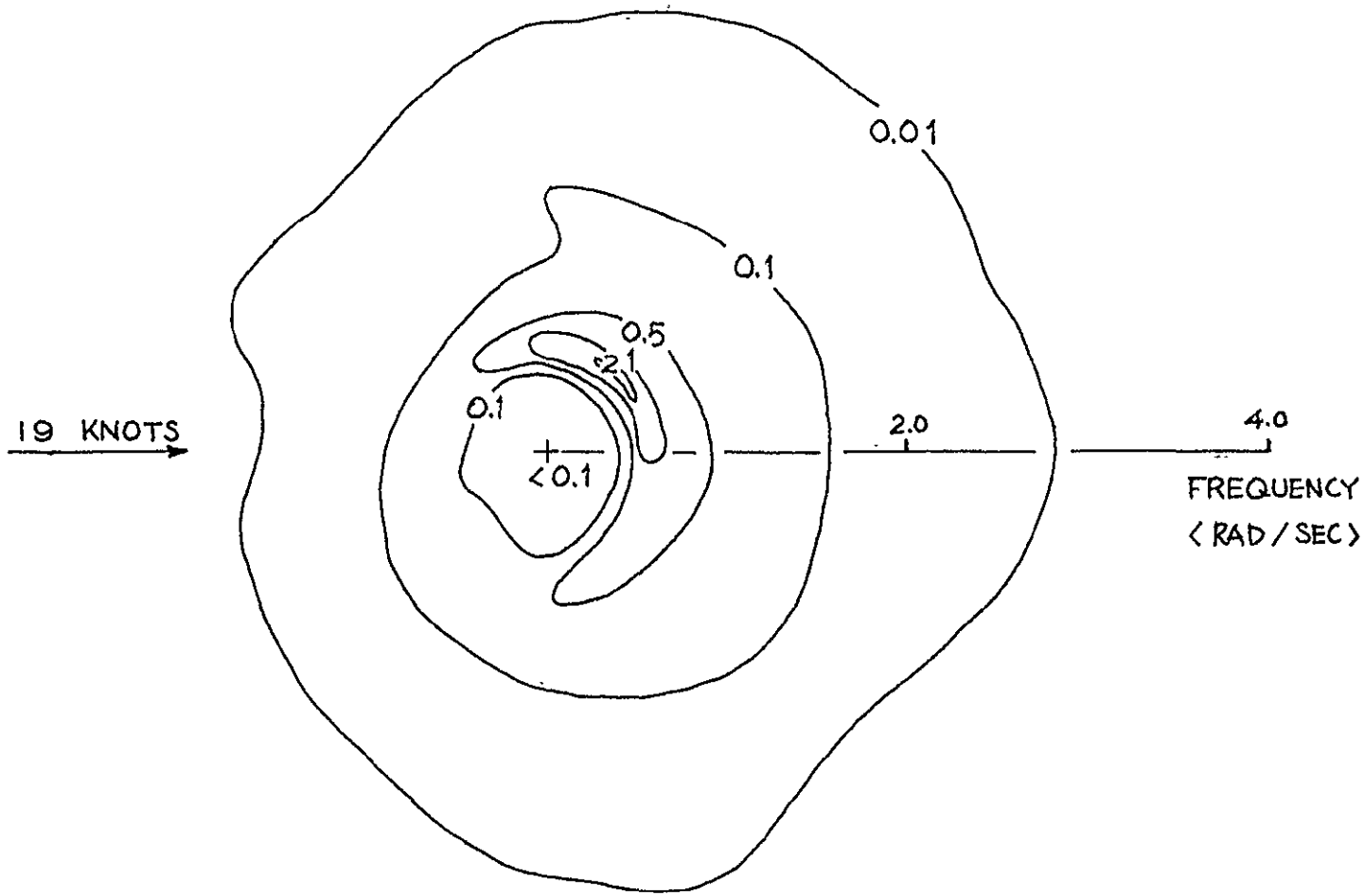

Fig. 5.2. Two-Dimensional Spectrum

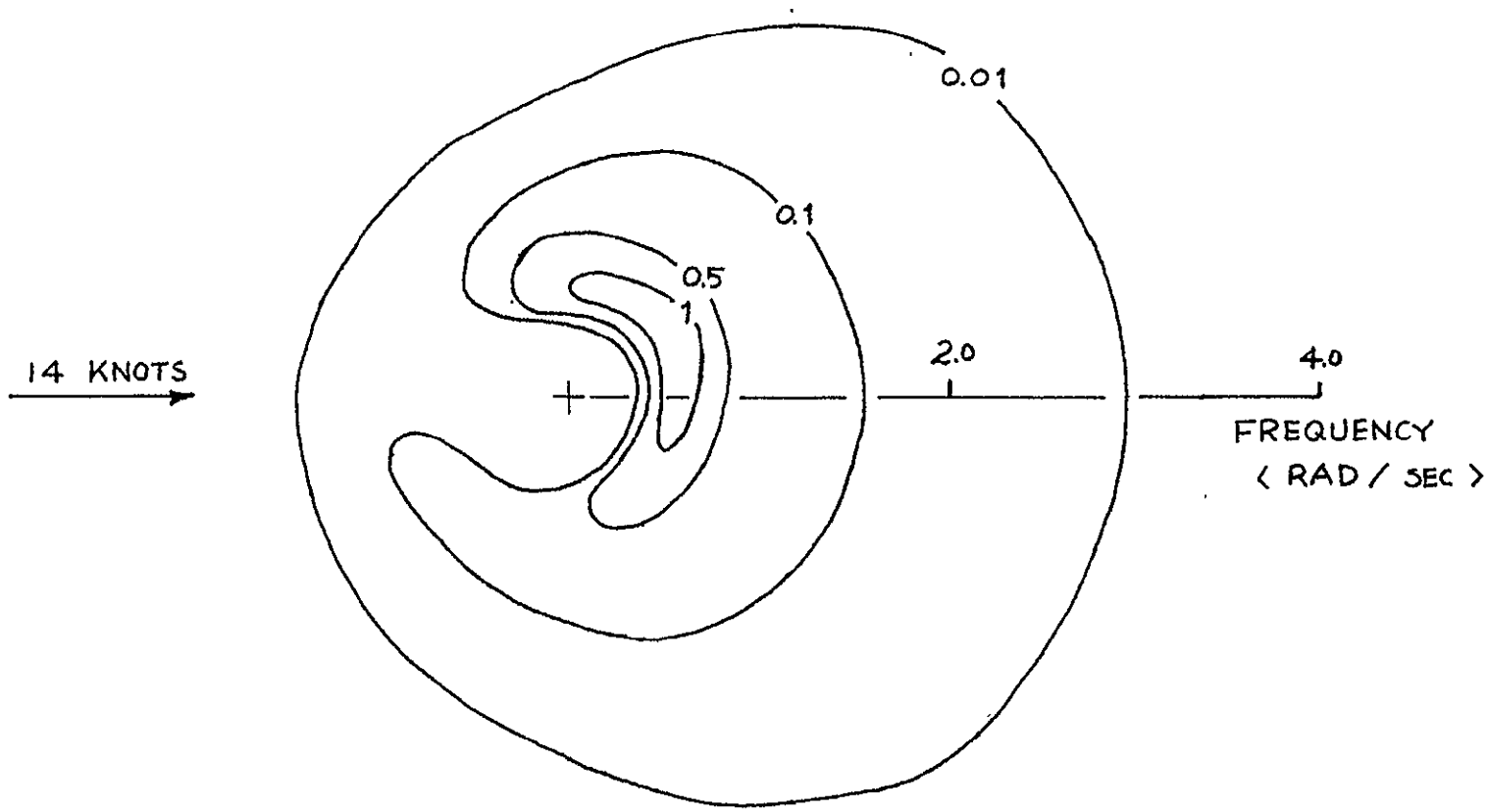

Fig. 5.3. Two-Dimensional Spectrum

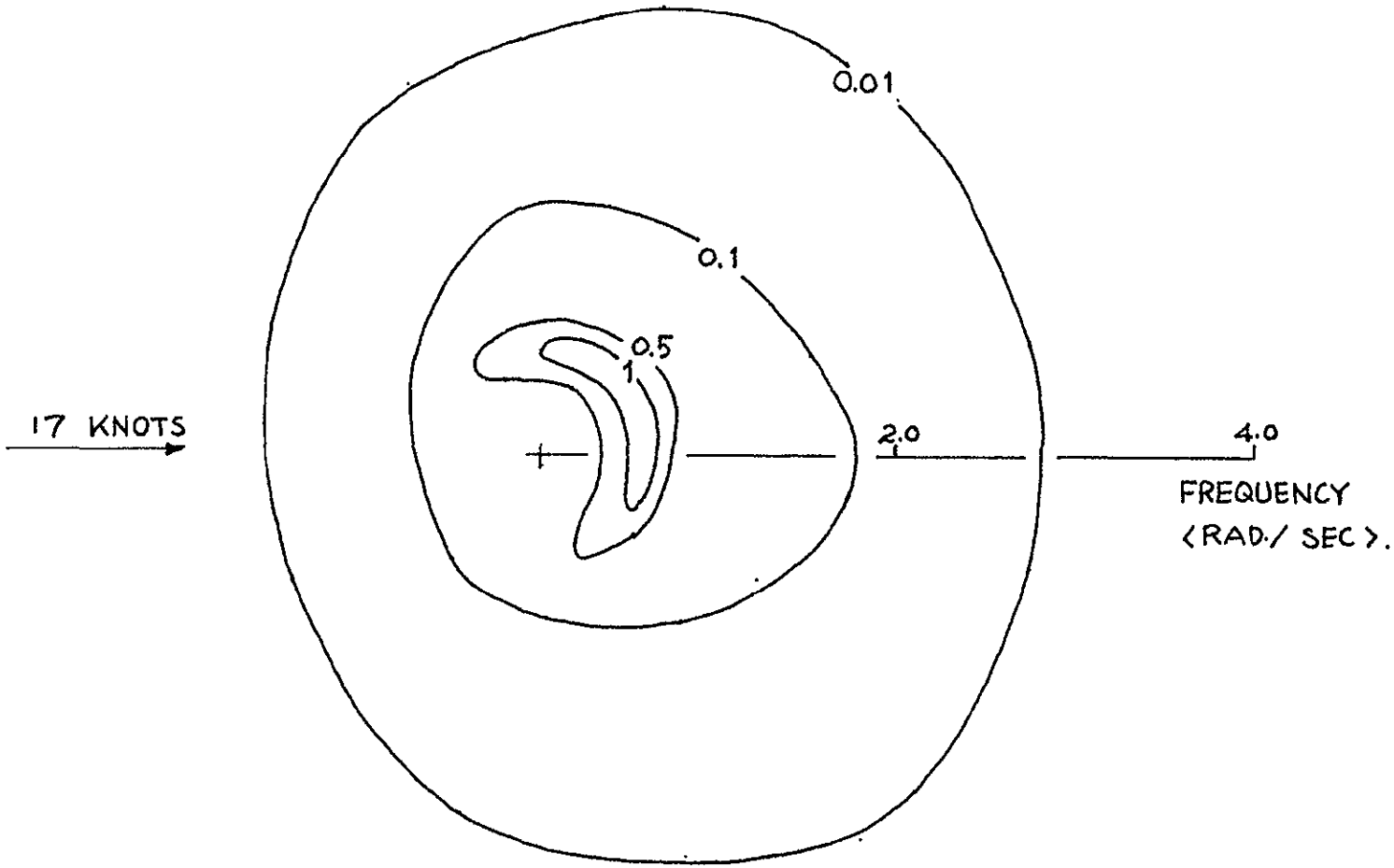

Fig. 5.4. Two-Dimensional Spectrum

law, and both their power indices decrease with increasing frequency, there is a cruicial difference. In Krylov's expression, energy distribution is confirmed in a half plane bounded by $(\frac{\pi}{2}, -\frac{\pi}{2})$, as implied by the dependence of cos $(\beta-\alpha)$; while in the Longuet-Higgins expression the dependency is on cos $\frac{\theta}{2}$; thus energy could be coming from the other side of the half plane at high frequencies. Considering the modification mechanism the Longuet-Higgins form seems more realistic.

Thirdly, the energy spectra contour diagram shows that skewness toward the wind directions is apparent, but that energy of small intensity is propagating against the wind. This upwind propagation of energy could easily be accounted for by one or more of the mechanisms discussed earlier. The skewness could be attributed to the direction from which the wind is blowing and also to the attenuation effect under adverse winds.

Fourthly, the integrated spectrum over all angular contributions shows the existence of an equilibrium range.

(d). Measurements of Orbital Velocity of Waves and Pressure and Their Use in Determining the Directional Spectrum

This idea was first suggested by Nagata[96] and later developed by Bowden and White[97] and Simpson[98] for measurements in England. The method of deriving the directional spectral information from velocity and pressure measurements is very similar to the buoy technique. Assuming there is a potential function ϕ for the wave motion,

$$u = -\frac{\partial\phi}{\partial x}, \quad v = -\frac{\partial\phi}{\partial y} \quad \text{and} \quad p = \frac{1}{g}\frac{\partial\phi}{\partial\tau} \tag{44}$$

then applying Fourier analysis to the record data of u, ν, and ρ, the first five Fourier components of the directional spectrum can be obtained.

e. Other Methods

Other methods, such as use of sun glitter as reported by Stilwell[99] have not been fully evaluated. The 180° ambiguity is inherent.

SECTION 5

REFERENCES

[1] Cramer, H. (1937), Random Variable and Probability Distributions, Tract No. 36, Cambridge University Press.

[2] Longuet-Higgins, M. S. (1946), "Resolution of the sea into long crested waves", Note ARL/103-30/N1/W, Admin, Res. Lab., Teddington, Middlesex, England.

[3] Pierson, W. J., Jr. (1952), "A unified mathematical theory for the analysis, propagation and refraction of storm generated ocean surface waves", Parts 1-11, Report College of Engr., Dept of Meteoro. & Ocean., NYU.

[4] Phillips, O. M. (1957), "On the generation of waves by turbulent wind," J. Fluid Mech. 2, 417-455.

[5] Phillips, O. M. (1958c), "Wave generation by turbulent wind over a finite fetch", Proc. 3rd. U. S. Congress of Appl. Math., 785-789.

[6] Phillips., O. M. (1967), "The theory of wind-generated waves", Advances in Hydro. Sci. 4, 119-149.

[7] Miles, J. W. (1957), "On the generation of surface waves by shear flows. J. Fluid Mech. 3, 185-204.

[8] Miles, J. W. (1959), "On the generation of surface waves by shear flows. Part II, III, J. Fluid Mech. 6, 568-598.

[9] Miles, J. W. (1962), "On the generation of surface waves by shear flows. Part IV, J. Fluid Mech. 13, 433-448.

[10] Miles, J. W. (1967), "On the generation of surface waves by shear flows. Part V J. Fluid Mech. 30, 163-175.

[11] Hulburt, E. O. (1943), "The polarization of light at sea", J. Optical Soc. Am. 24, 35-42.

[12] Schooley, A. H. (1954), "A simple optical method for measuring the statistical distribution of water surface slopes", J. Optical Soc. Am. 44, 37-40.

[13] Cox, C. S. and W. H. Munk (1954a), "Measurement of the roughness of the sea surface from photographs of the sun's glitter", J. Optical Soc. Am. 44, 838-850.

[14] Cox, C. S. and W. H. Munk (1955), "Some problems in optical oceanography", J. Mar.Res.14, 63-78.

[15] Cox, C. S. (1958), "Measurement of slopes of high frequency wind waves", J. Mar. Res. 16, 199-215.

[16] Stilwell, Denzil, Jr. (1969), "Directional energy spectra of the sea from photographs", J. Geophys. Res. 74, 1974-1986.

[17] Kolmogoroff, A. N. (1941), "The local structure of turbulence in incompressible viscous fluid for very large Reynolds numbers", C. R. Acad. Sci. USSR 30, 301.

[18] Kolmogoroff, A. N. (1941), "Dissipation of energy in locally isotropic turbulence", C. R. Acad. Sci. USSR 34, 16.

[19] Phillips, O. M. (1958a), "The equilibrium range in the spectrum of wind generated waves", J. Fluid Mech. 4, 426-434.

[20] Stokes, G. G. (1880), "Supplement to a paper on the theory of oscillatory waves", Math. & Phys. Papers, Vol. 1, Cambridge Univ. Press, 314-326.

[21] Gaillard, D. D. (1904), "Wave action in relation to engineering structure", Professional Paper of Corps of Engineers, No. 31, U. S. Army, Government Printing Office, Washington, D. C., 232 pp.

[22] Longuet-Higgins, M. S. and R. W. Stewart (1964) "Radiation stresses in water waves; a physical discussion with applications", Deep Sea Res. 11, 529-562.

[23] Longuet-Higgins, M. S. and R. W. Stewart (1960), "Change in the form of short gravity waves on long waves and tidal current", J. Fluid Mech. 8, 565-583.

[24] Crapper, G. D. (1957), "An exact solution for progressive capillary of arbitrary amplitude", J. Fluid Mech. 2, 532-539.

[25] Schooley, A. H. (1958), "Profiles of wind-created water waves in capillary gravity transition region", J. Mar. Res. 16, 100-108.

[26] Phillips, O. M. (1966), The Dynamics of the Upper Ocean, Cambridge Univ. Press, London and New York, 261 pp.

[27] Barnett, T. P. and J. C. Wilkerson (1967), "On the generation of ocean wind waves as inferred from airborne radar measurements of fetch-limited spectrum", J. Mar. Res. 25, 292-328.

[28] Burling, R. W. (1959), "The spectrum of wave at short fetches", Deutsche Hydro Zeit. 12, 45-65.

[29] Hicks, B. L. (1960), "The energy spectrum of small wind waves". Univ. of Illinois, Control System Laboratory Report No. M-92.

[30] Kinsman, B. (1960), "Surface waves at short fetches and low wind speed--a field study", Chesapeake Bay Inst., The Johns Hopkins University, Tech. Report No. 19.

[31] Kitaigorodskii, S. A. (1962), "Applications of the theory of similarity to the analysis of wind-generated motion as a Stochastic Process", Bull. (Izv) Acad. Sci. USSR Geophysical Series No. 1, 105-117.

[32] Pierson, W. J., Jr. (1962), "The directional spectrum of a wind generated sea as determined from data obtained by the Stereo Wave Observation Project", College of Engr. NYU, Meteor. Paper 2. No. 6.

[33] Longuet-Higgins, M. S., D. E. Cartwright, and N. D. Smith (1963), "Observations of the directional spectrum of sea waves using the motions of a floating buoy", Ocean Wave Spectra, Prentice-Hall, Inc., Englewood Cliffs, N. J., 111-130.

[34] Hidy, G. M. and E. J. Plate (1966) "Wind action on water standing in a laboratory channel", J. Fluid Mech. 26, 651-687.

[35] Volkov, Yu. A. (1968), "An analysis of the spectra of ocean waves generated by turbulent wind", Atmo. and Oceanic Phys., Izv. Akad. Nauk SSSR 4, 968-987.

[36] Phillips, O. M., "On some properties of the spectrum of wind generated waves", J. Mar. Res. 16,231-245.

[37] Phillips, O. M., "The low frequency components of the spectrum of wind generated waves", J. Mar. Res. 19, 57-69.

[38] Kitaigorodskii, S. A. and S. S. Strekalov (1962), "Analyzing the spectra of a wind swell I" Bull. (IZV) Acad. Sci. USSR, Geophysical Series 1962, No. 9, 765-769.

[39] Moskowitz, Lionel (1964), "Estimates of the power spectrums for fully developed seas for wind speed of 20 to 40 knots", J. Geophys. Res. 69, 5161-5179.

[40] Pierson, W. J., Jr. (1959), "A study of wave forecasting method and of the height of a fully-developed sea on the basis of some wave records obtained by the O. W. S. Weather Explorer during a storm at sea," Deutsche Hydro. Zeit. 12, 244-259.

[41] Pierson, W. J., Jr. and L. Moskowitz (1964), "A proposed spectral form for fully developed wind seas based on the similarity theory of S. A. Kitaigorodskii", J. Geophys. Res. 69, 5181-5190.

[42] Neuman, G. (1964), "Zur Characteristik des Seeganges", Arch. Meteor. Geophys. Bio. A 7, 353.

[43] Bretschneider, C. L. (1959), "Wave variability and wave spectra for wind-generated gravity waves", Beach Erosion Board, Tech. Memo No. 118, 192 pp.

[44] Bretschneider, C. L., (1963), "A one dimensional gravity wave spectrum", Ocean Wave Spectra, Prentice-Hall, Inc., Englewood Cliffs, N. J.

[45] Darbyshire, J. (1955), "An investigation of storm waves in the North Atlantic Ocean", Proc. Roy, Soc. Am. A 230, 560-569.

[46] Darbyshire, J. (1959), "A further investigation of wind generated waves", Deutsche Hydro. Zeit. 12, 1-13.

[47] Kitaigorodskii, S. A. andS. S. Strekalov (1963), "Analyzing the spectra of a wind swell II", Bull, (IZV) Acad. Sci. USSR, Geophysical Series 1963, No. 3, 754-760.

[48] Stommel, H. (1965) The Gulf Stream, University of California - Press Berkeley 2nd Ed. 248.

[50] Phillips, O. M. (1966), "The dynamics of the upper ocean, Cambridge Univ. Press. London and New York.

[51] Ursell, F. (1956), "Wave generation by wind", Survey in Mech. ed. by Batchelor Cambridge Univ. Press 216-249.

[52] Phillips, O. M. (1957) "On the generation of waves by turbulent wind" J. Fluid Mech. 2 417-445.

[53] Miles, J. W. "On the generation of surface wave by shear flows", Part 2 JRM 6 568-582 1959a.
Part 3 6 582-598 1959b
Part 4 13 433-448 1962
Part 5 30 163-175 1967

[54] Phillips, O. M. (1958c) "Wave generation by turbulent wind over a finite fetch" Proc. 3rd. U. S. Congress App. Math.

[55] Willmorth, W. W. and Wooldridge (1962) "Measurement of the fluctuating pressure at the wall beneath a thick turbulent boundary layer J. Fluid Mech. 14, 187-210.

[56] Lighthill, M. J. (1959) Introduction to Fourier Analysis and Generalized Functions, London: Cambridge University Press.

[57] Stereo Wave Observation Project (1957) "The directional spectrum of a wind generated sea" Research Div. College of Engr. NYU, 267.

[58] Brooke, Benjamin T. (1959), "Shearingflow over a wavy boundary" J. Fluid Mech. 6 161-205.

[59] Lighthill, M. J. (1962) "Physical interpretation of the mathematical theory of wave generation by wind." Jour. Fluid Mech. 14, 385-398.

[60] Miles, J. W. (1960) "On the generation of surface waves by turbulent shear flows" J. Fluid Mech. 7 469-478.

[61] Shemdin, O. H. and Hsu E. Y. (1967), "Direct measurement of aerodynamic pressure above a simple progressive gravity wave" J. Fluid Mech 30, 403-416.

[62] Lamb, H. (1932) "Hydrodynamics" Cambridge Univ. Press, London.

[63] De, S. C. (1955) "Contributing to the theory of Stokes waves" Proc. Camb Phil. Soc. 51 713-736.

[64] Phillips, O. M. (1962) "Resonance phenomenon in gravity waves" Proc. of Symp. in Applied Math Vol 13.

[65] Phillips, O. M. (1963a) "The dynamics of random finite amplitude gravity waves" Ocean Wave Spectrum 171-190.

[66] Longuet-Higgins, M. S. (1962a) "Resonant interaction between two trains of gravity waves" J. Fluid Mech. 12 321-332.

[67] Benney, D. J. (1962) "Non-linear gravity wave interactions" J. Fluid Mech 14 577-584.

[68] Hasselman, K. (1962) "On the non-linear energy transfer in a gravity wave spectrum" J. Fluid Mech 12 481-500.

[69] Hasselman, K. (1963) "On the non-linear energy transfer in a wave spectrum" Ocean Wave Spectrum 191.

[70] Bretherton, F. P. (1964) "Resonant interactions between waves" J. Fluid Mech. 20 457-479.

[71] McGoldrick, L. F. (1965) "Resonant interactions among capillary-gravity waves" J. Fluid Mech 21 305-332.

[72] McGoldrick, L. F. Phillips, Huany, Hodgson (1966) "Measurements on resonant wave interactions" J. Fluid Mech. 437-456.

[73] Longuet-Higgins, M. S. and Smith, N. D. (1966) "An experiment on third order resonant wave interaction J. Fluid Mech. 25 417-436.

[74] Batchelor, G. K. (1957) "Wave scattering due to turbulence" Proc. 1st Symp. Naval Hyd. 409-422.

[75] Phillips, O. M. (1959) "The scattering of gravity waves by turbulence" J. Fluid Mech. 5 177-192.

[76] Longuet-Higgins, M. S. (1963) "The generation of capillary waves by steep gravity waves" J. Fluid Mech. 16 138-159.

[77] Longuet-Higgins, M. S. and Stewart, R. W. 1960) "Change in the form of short gravity waves on long waves and tidal current" J. Fluid Mech. 8 565-583.

[78] Phillips O. M. (1963b) "On the attenuation of long waves by short breaking waves" J. Fluid Mech 16 321-332.

[79] Longuet-Higgins, M. S. (1952) "On the statistical distribution of the height of sea waves" J. Marine Res. 11 245-266.

[80] Longuet-Higgins, M. S. (1962b) "The directional spectrum of ocean waves and process of wave generation" Proc. Roy. Soc. A 265 286-315.

[81] Longuet-Higgins, M. S. (1963b) "The effect of non-linearities on statistical distributions in the theory of sea waves." J. Fluid Mech 17 459-480.

[82] Barber, N. F. (1946) "Measurements of sea conditions by the motions of a floating buoy." Admiralty Res. Lab. Rep. 130 40/N_2W 8.

[83] Cote, L. J. et al (1960) "The directional spectrum of a wind generated sea as determined from data obtained by the Stereo Wave Observation Project." College of Engr. Meteor Paper 2 No. 6 88.

[84] Uberior, M. S. (1964) "Directional spectrum of wind generated ocean waves" J. Fluid Mech. 19 452-464.

[85] Barber, N. F. (1954) "Finding the direction of travel of sea waves" Nature 174 1048-1050.

[86] Barber, N. F. (1963a) "The directional resolving power of an array of wave detectors" Ocean Wave Spectrum 137-150.

[87] Konyayev, K. V. and Dreyer A. A. (1965) "Measurement of a two-dimensional energy spectrum of wave disturbance" Oceanology 5 121-126.

[88] Dreyer, A. A. and Konyayev, K. V. (1967) "Sea wave measurements using a directional probe system" Oceanology 7 721-725.

[89] Munk, W. H. et al (1963) "Directional recording of swell from distant storms" Phil Trans. A 225 505-584.

[90]Tsypluklin, V. R. (1966) "Experimental study of probability characteristics of wind caused wave measurement" Stereo and Ocean Phys 2 41-45.

[91] Krylov, Yu. M. et al (1968) "On the angular energy spectrum of wind waves"Atmo. and Ocean Phys 2 441-446.

[92] Krylov, Yu. M. et al (1968) "Investigation of the two-dimensional energy spectrum and of the wavelength of wind-induced waves" Atmo. and Ocean Phys. 4 376-381.

[93] Longuet-Higgins, M. S. Cartwright, D. E. and Smith, N. D. (1963) "Observations of the directional spectrum of sea waves using the motions of a floating buoy" Ocean Wave Spectra 111-130.

[94] Cartwright, D. E. and Smith, N. D. (1964) "Buoy techniques for obtaining directional wave spectra" Buoy Technology 112-122.

[95] Ewing, J. A. (1969) "Some measurements of the directional wave spectrum" J. Marine Res. 27 481-500.

[96] Nagata, T. (1964) "The statistical properties of obital wave motion and their application for the measurement of directional wave spectra" J. Ocean Soc. Japan 19 169-182.

[97] Bowder, K. F. and White, R. A. (1966) "Measurements of the obital velocity of sea waves and their use in determining the directional spectrum" Geophys J. Roy Astr. Soc. 12 33-54.

[98] Simpson, J. H. (1969) "Observations of the directional characteristics of sea waves" Geophys J. Roy. Astr. Soc. 17 93-120.

[99] Stilwell, D., Jr. (1969) "Directional energy spectra of the sea from photographs" J. Geophys. Res. 74 1974-1986.

APPENDIX A

This Appendix contains a number of waveforms which resulted from the computer simulation study of the altimeter. Each series of figures is preceeded by a short description of the simulation parameters.

Figures A-1 through A-4 illustrate typical simulated results of square-law (E^2) and linear (E) detector waveforms for a 50 ns rectangular pulse. These data correspond to the backscattered signal for the limiting case of a fast rise-time transmitter pulse, wide-band receiver, and infinite signal-to-noise ratio.

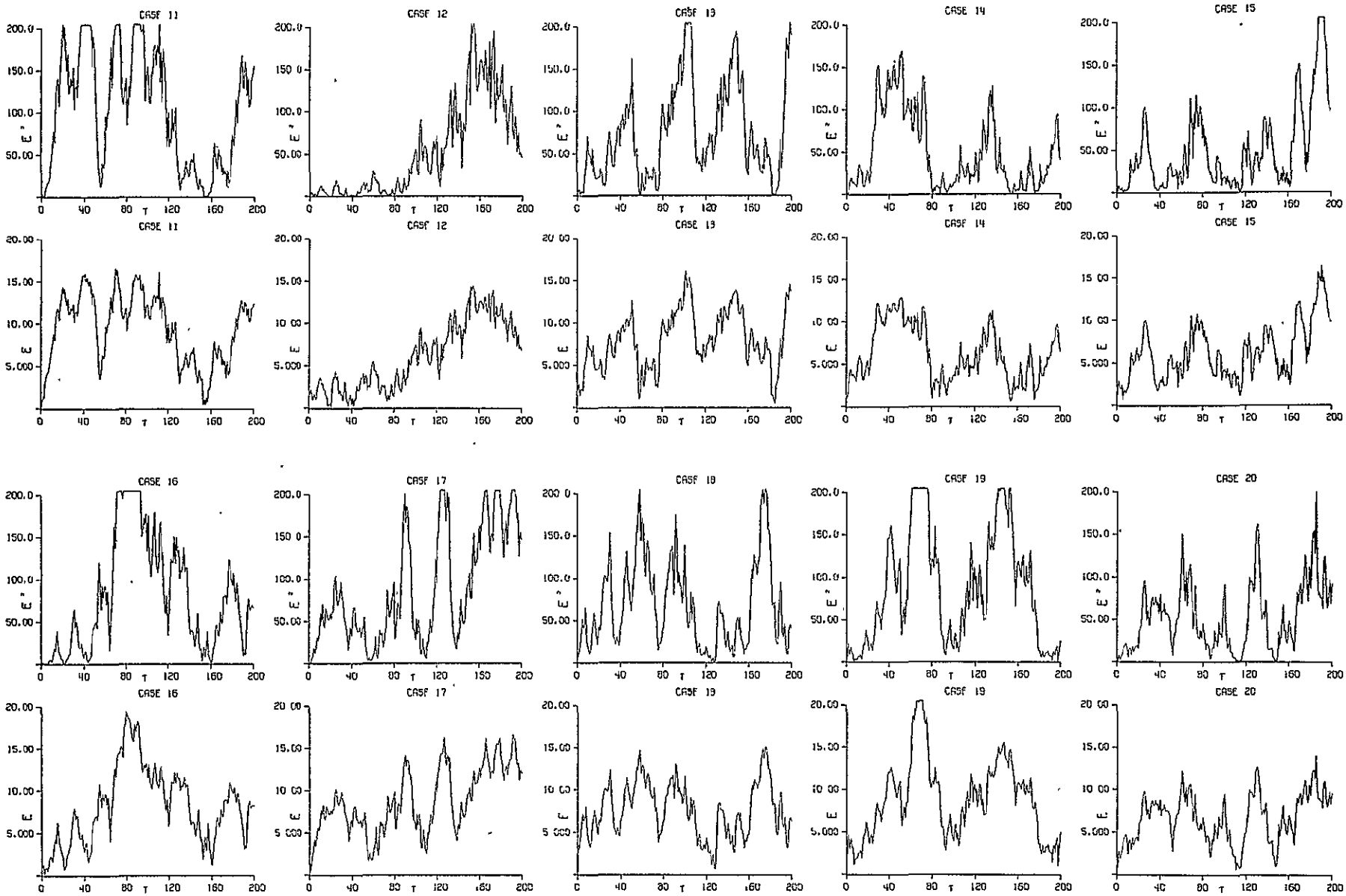

Fig. A-1. Typcial Simulated Results of Square Law and Linear Detector Waveforms for a 50 ns Rectangular Pulse, SNR = ∞

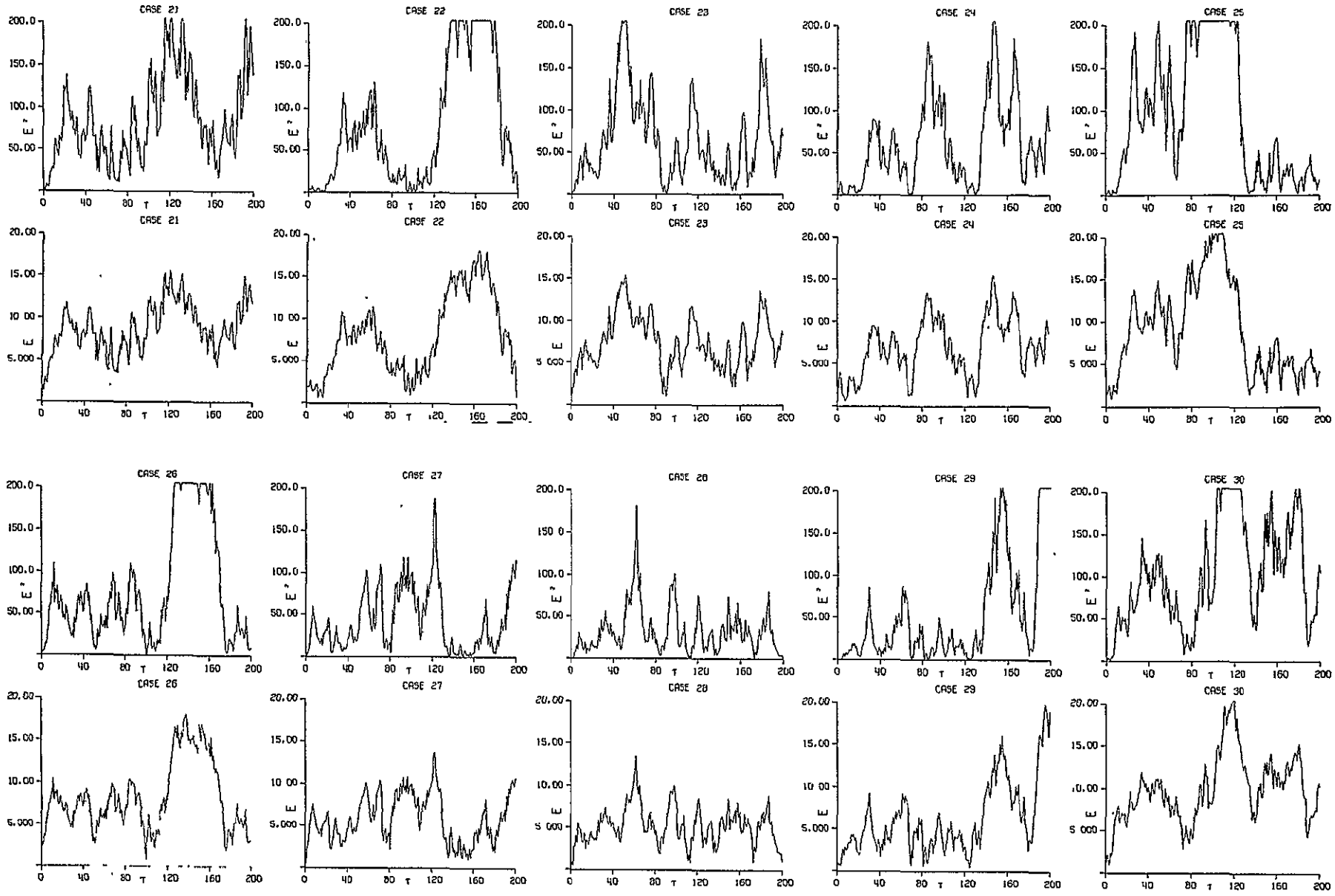

Fig. A-2. Typical Simulated Results of Square Law and Linear Detector Waveforms for a 50 ns Rectangular Pulse, SNR = ∞

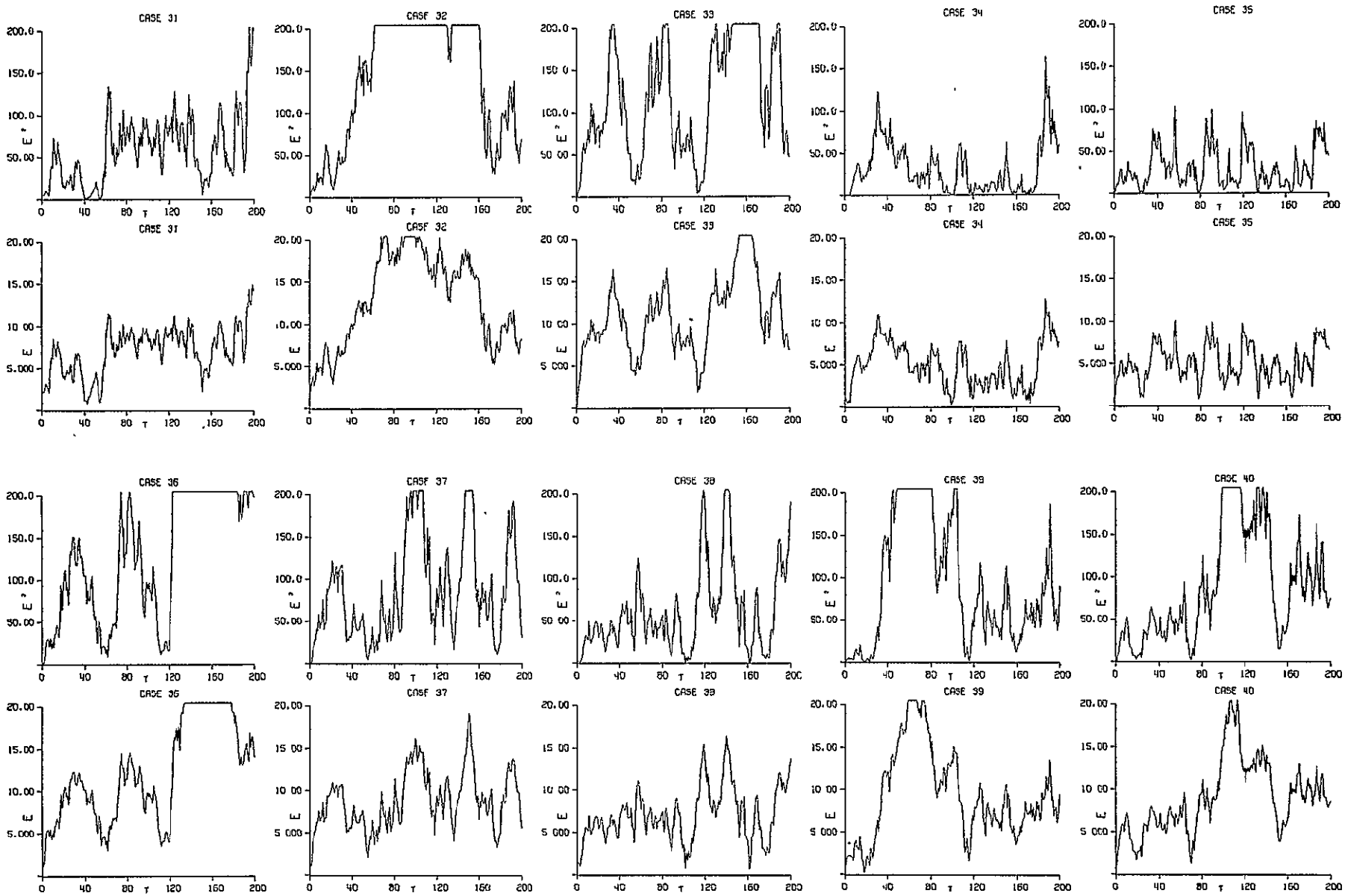

Fig. A-3. Typical Simulated Results of Square Law and Linear Detector Waveforms for a 50 ns Rectangular Pulse, SNR = ∞

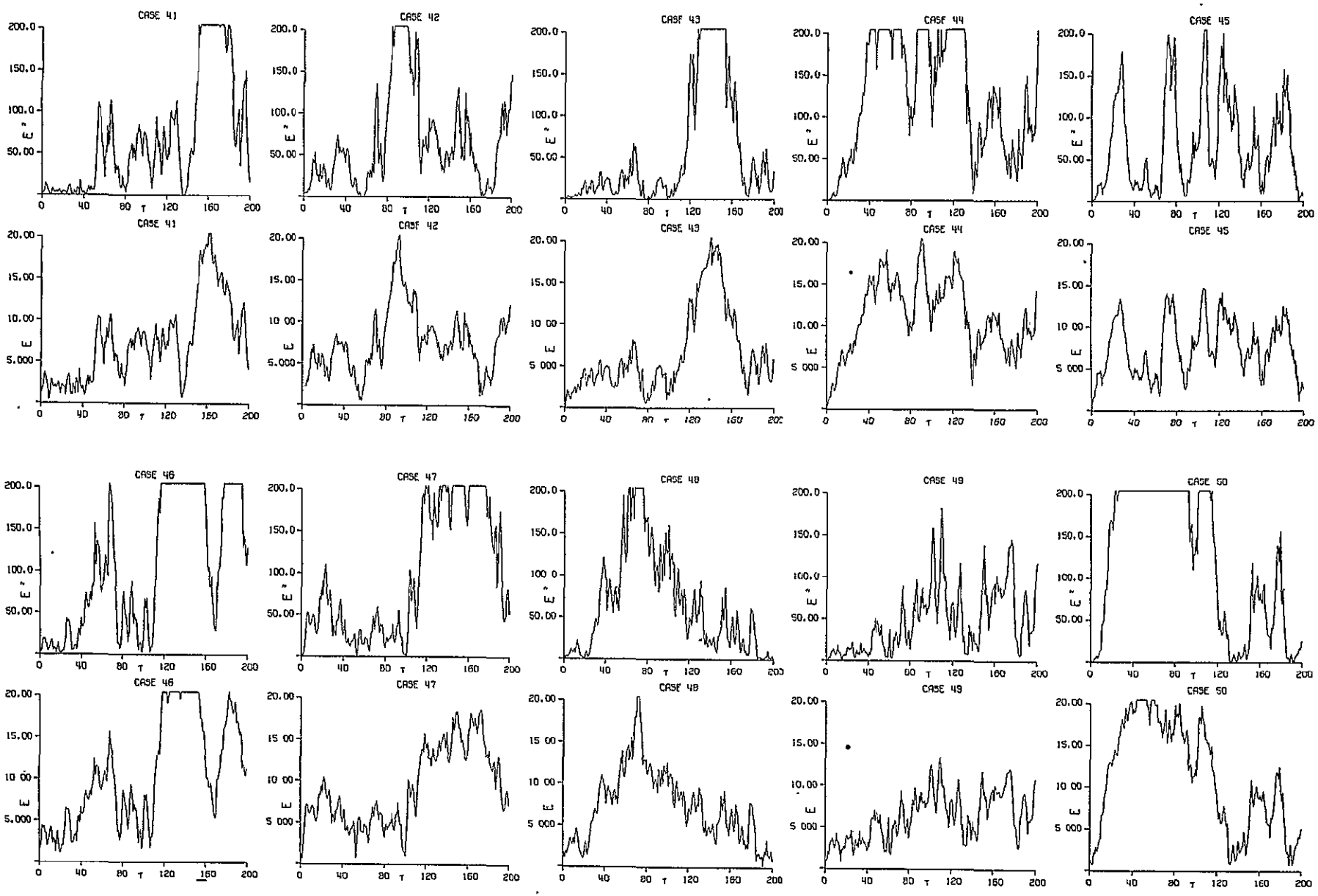

Fig. A-4. Typical Simulated Results of Square Law and Linear Detector Waveforms for a 50 ns Rectangular Pulse, SNR = ∞

Figures A-5 through A-9 illustrate typical simulated results of square-law (E^2) and linear (E) detector waveforms for a 50 ns pulse of Gaussian shape and for noise-free reception. These data are representative of the waveforms for a matched-filter receiver.

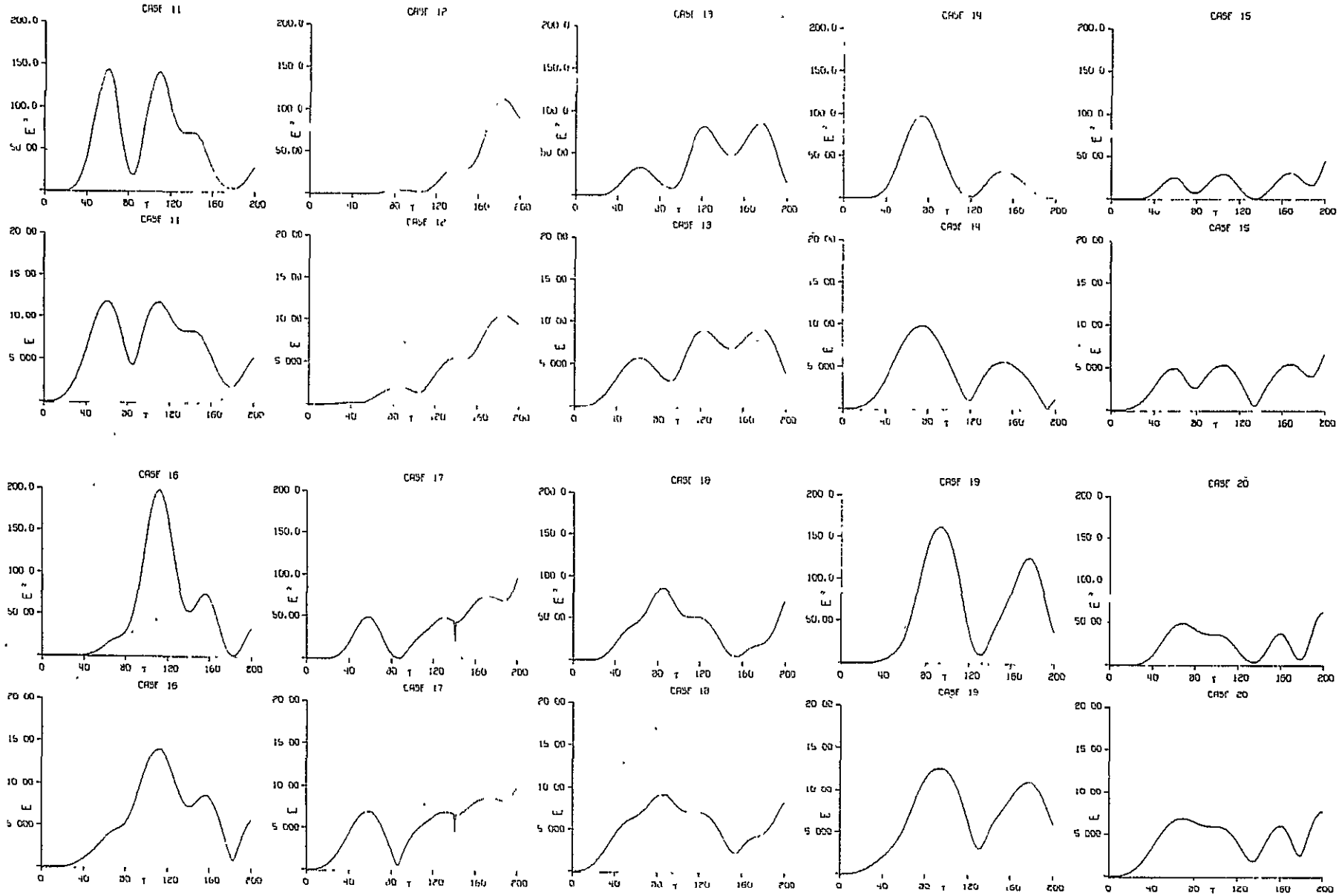

Fig. A-5. Typical Simulated Results of Square Law and Linear Detector Waveforms for a 50 ns Gaussian Pulse, SNR = ∞

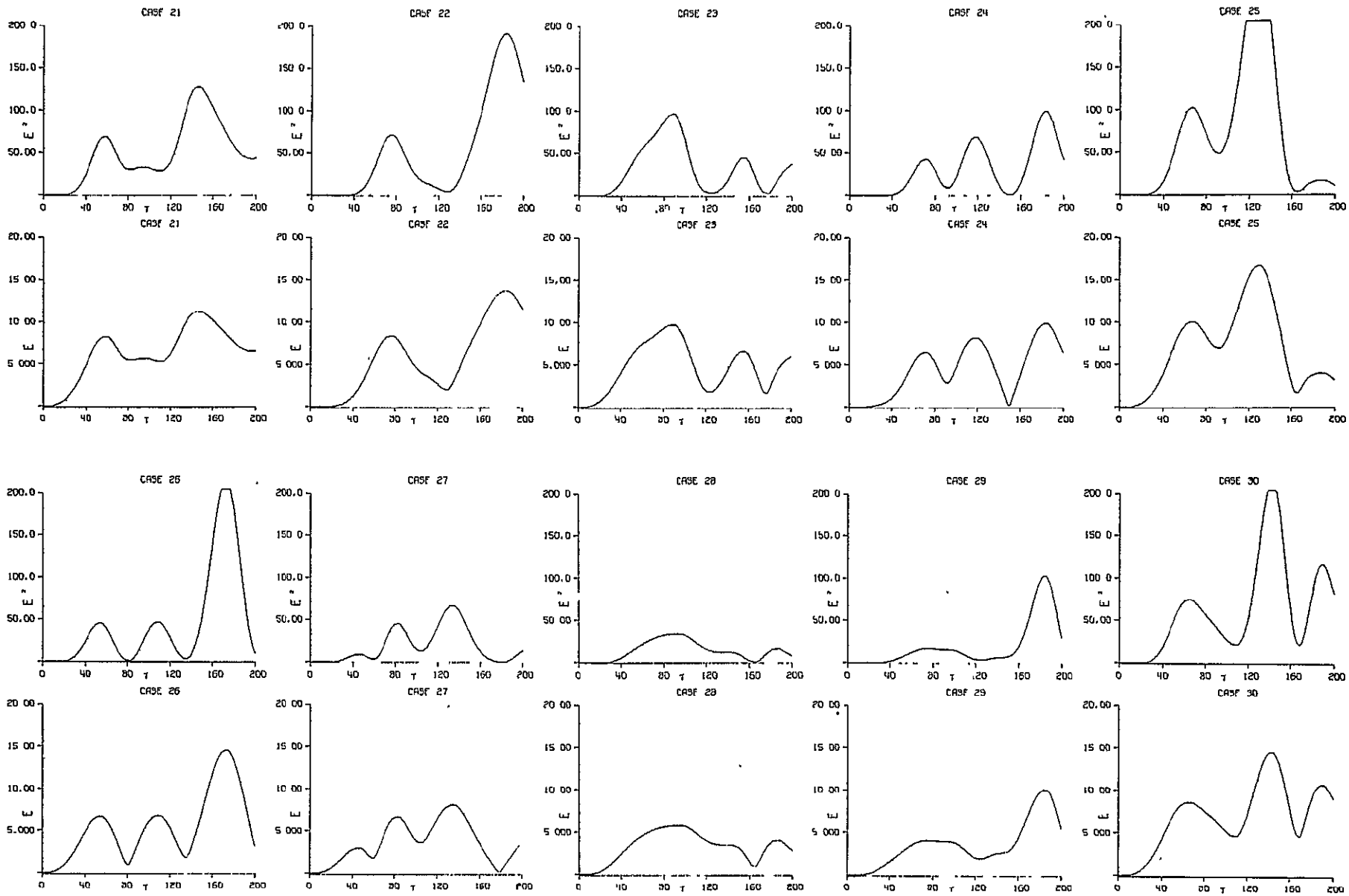

Fig. A-6. Typical Simulated Results of Square Law and Linear Detector Waveforms for a 50 ns Gaussian Pulse, SNR = ∞

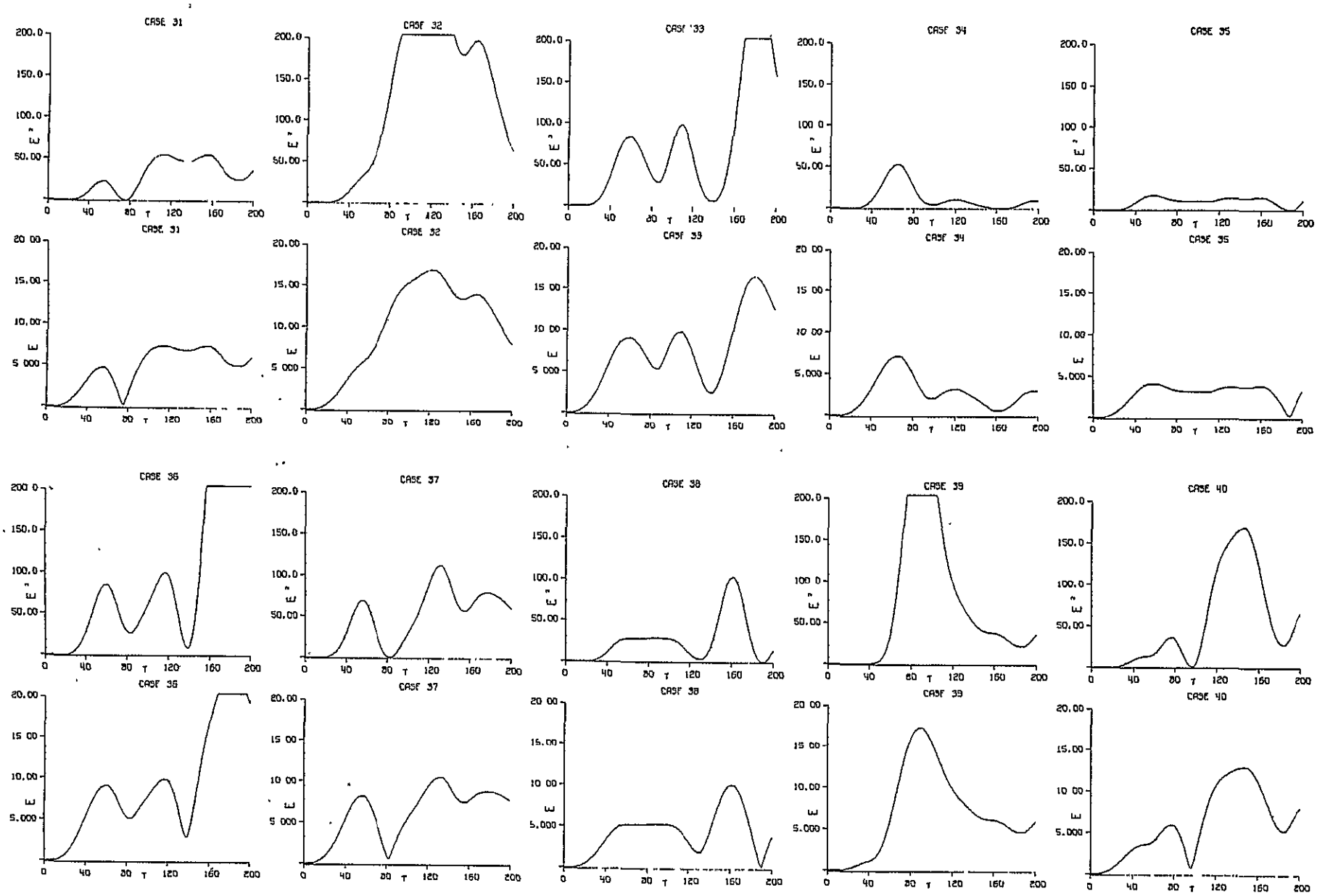

Fig. A-7. Typical Simulated Results of Square Law and Linear Detector Waveforms for a 50 ns Gaussian Pulse, SNR = ∞

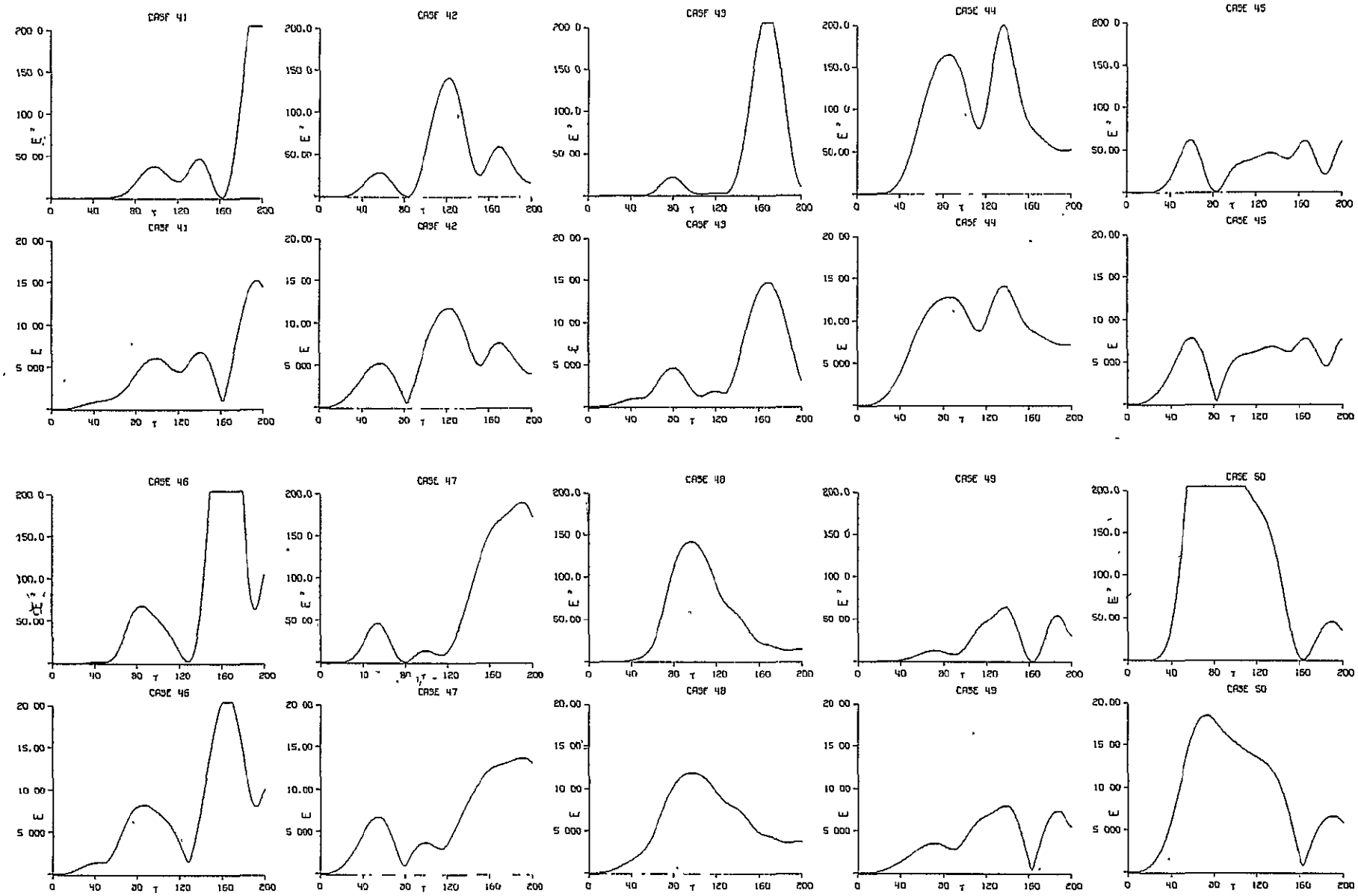

Fig. A-8. Typical Simulated Results of Square Law and Linear Detector Waveforms for a 50 ns Gaussian Pulse, SNR = ∞

Figures A-9 and A-10 are comparable to the data shown in Figure 2-3 of the text, except that new random numbers were used for both signal and noise in Figure A-10.

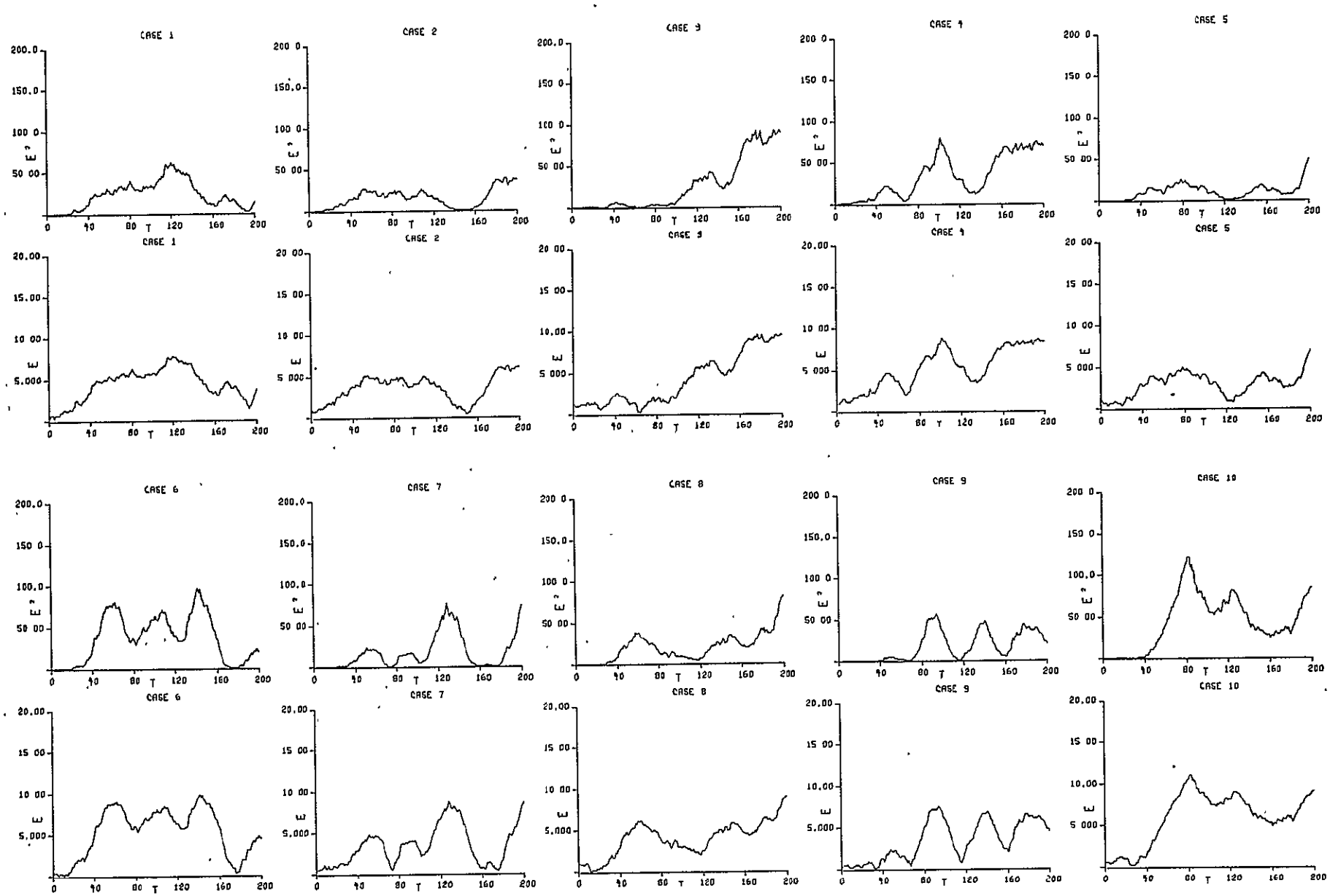

Fig. A-9. Typical Simulated Results of Square Law and Linear Detector Waveforms For a 50 ns Gaussian Pulse, SNR = 20 db (First Computation)

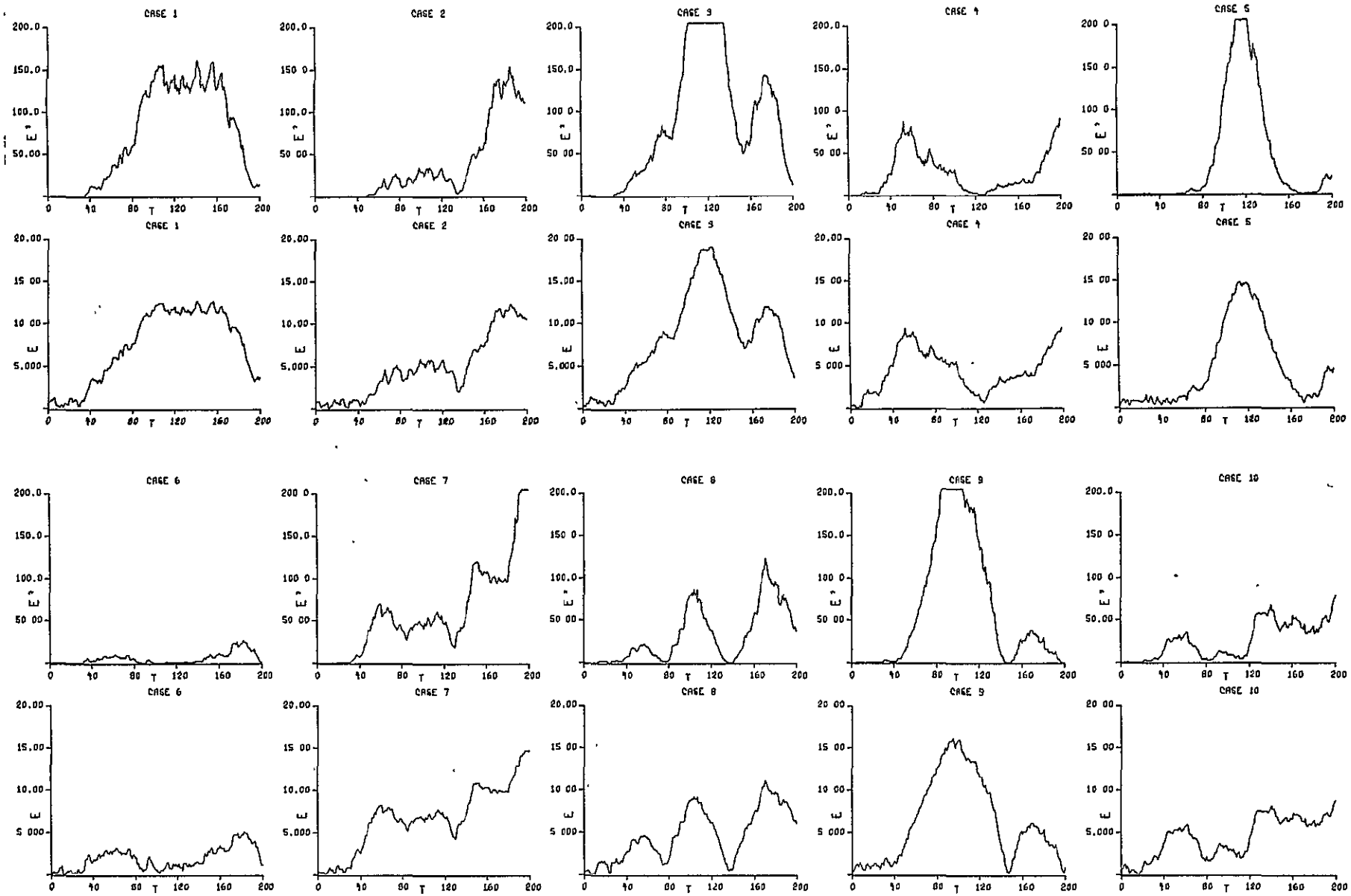

Fig. A-10. Typical Simulated Results of Square-Law and Linear Detector Waveforms For a 50 ns Gaussian Pulse, SNR = 20 db (Second Computation)

This section contains several double-delay differencing results. Figures A-11 and A-12 show the effect of receiver noise bandwidth and comparison of Figures A-11 and A-13 demonstrates the effect of new random numbers (for both signal and noise) on the waveforms involved in double-delay differencing. Additional double-delay differencer output waveforms are shown in Figures A-14 through A-16. Figures A-17 and A-18 show the double-delay differencer output for a Gaussian-shaped pulse, when the input is a 50 case average for SNR=∞ and 30 db, respectively.

CASE 1

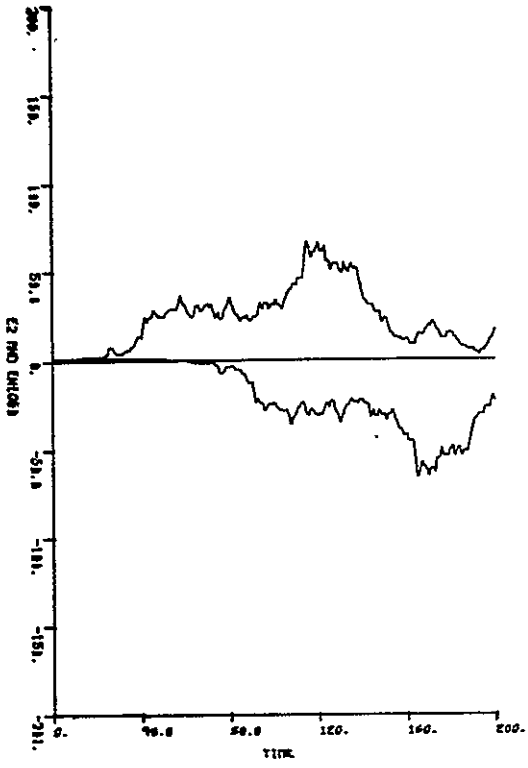

First Difference

CASE 1

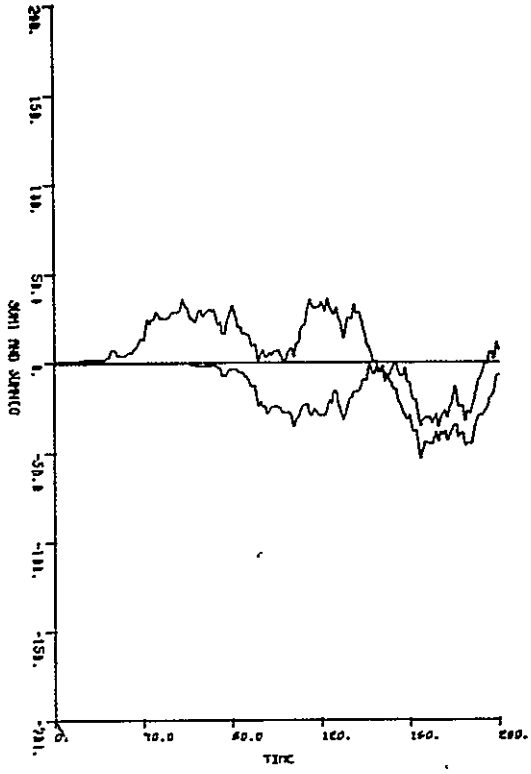

Second Difference

CASE 1

Final Waveform

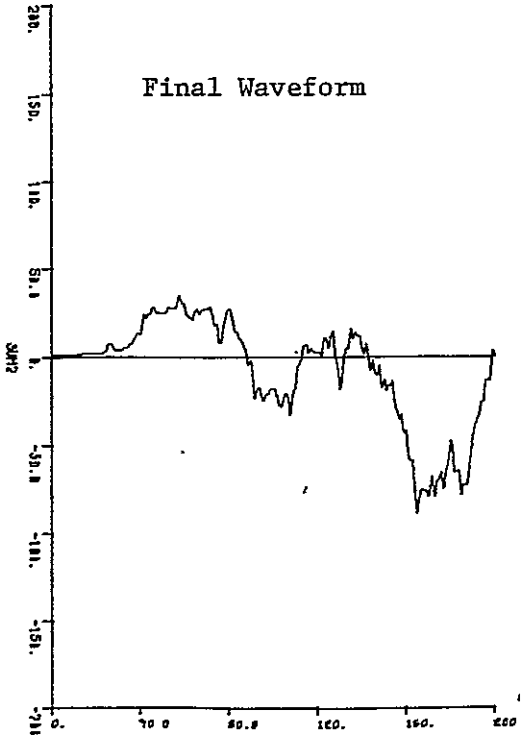

Fig. A-11. Typical Waveforms Involved in Double-Delay Differencing Operations, SNR = 20 db, ACF = $e^{-.125}$

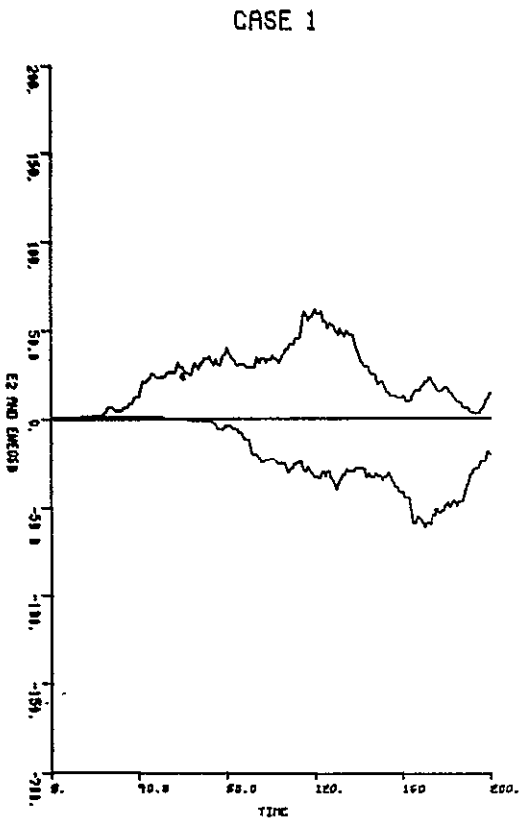

First Difference

Second Difference

Fig. A-12. Typical Waveforms Involved in Double-Delay Differencing Operations, SNR = 20 db, ACF = $e^{-.062}$

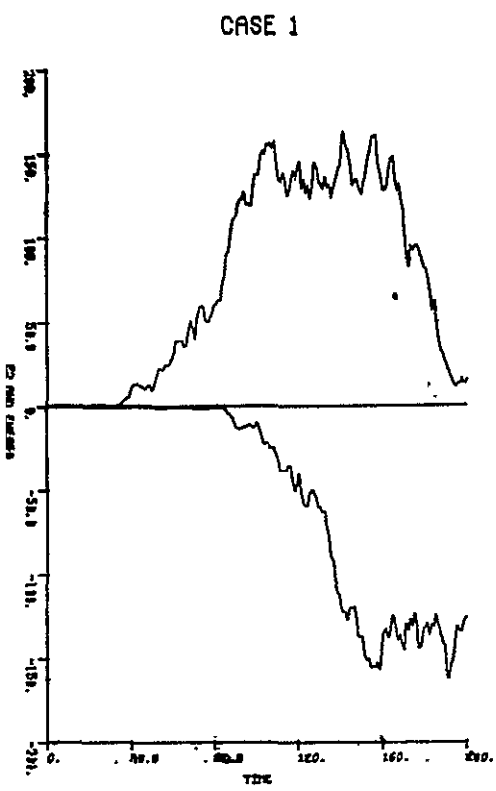

First Difference

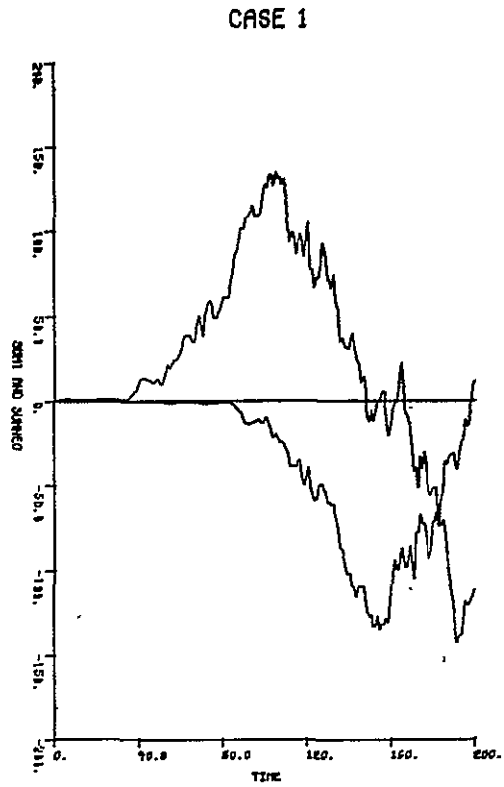

Second Difference

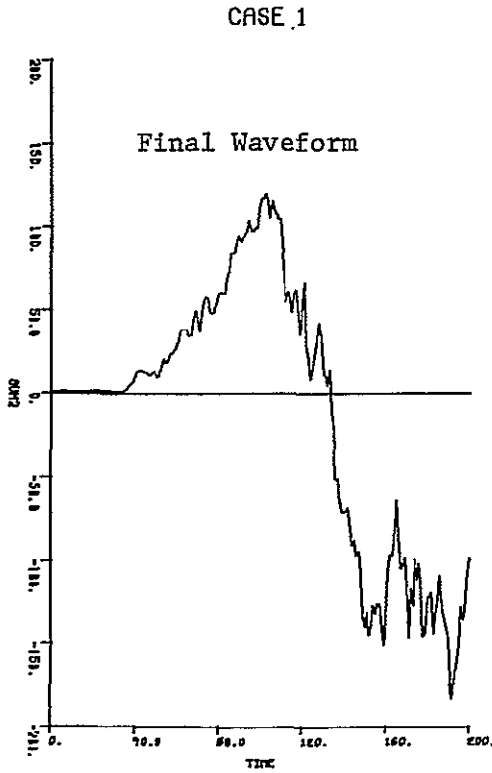

Fig. A-13. Typical Waveforms Involved in Double-Delay Differencing Operations, SNR = 20 db, ACF = $e^{-.125}$

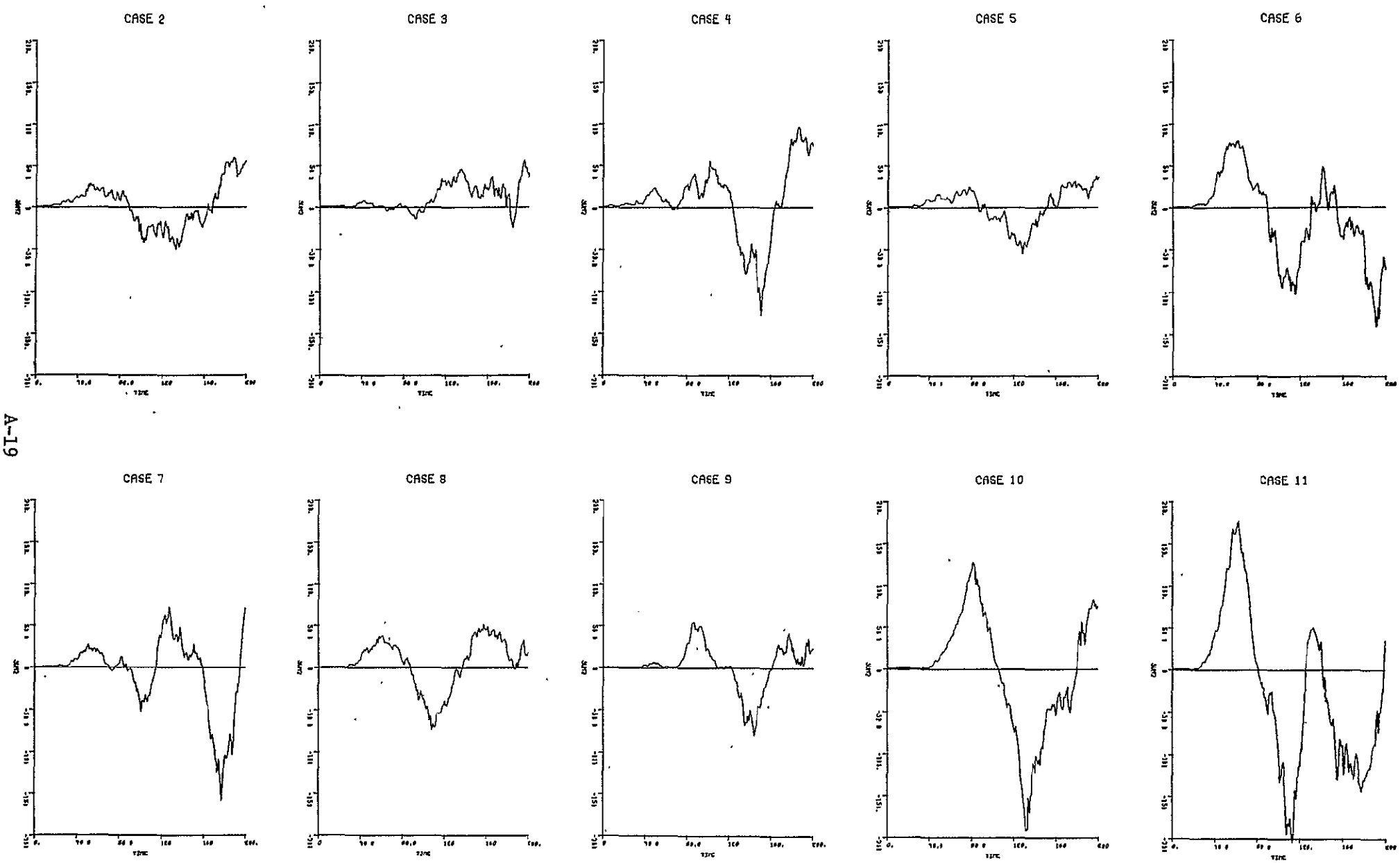

Fig. A-14. Final Waveforms for 10 Simulated Cases of Double-Delay Differencing Operations, SNR = 20 db, ACF = $e^{-.125}$

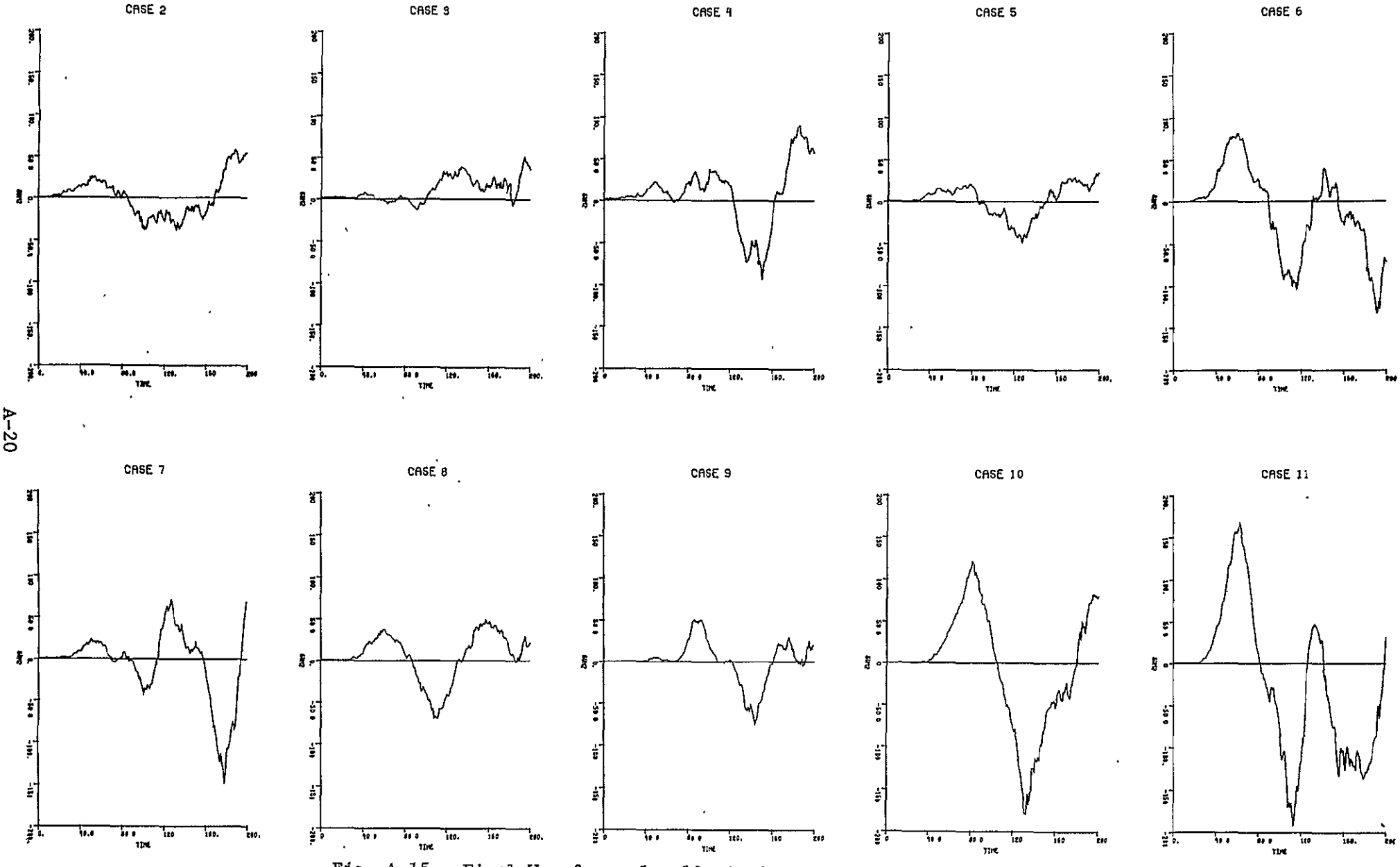

Fig. A-15. Final Waveforms for 10 Simulated Cases of Double-Delay Differencing Operations, SNR = 20 db, ACF = $e^{-.062}$

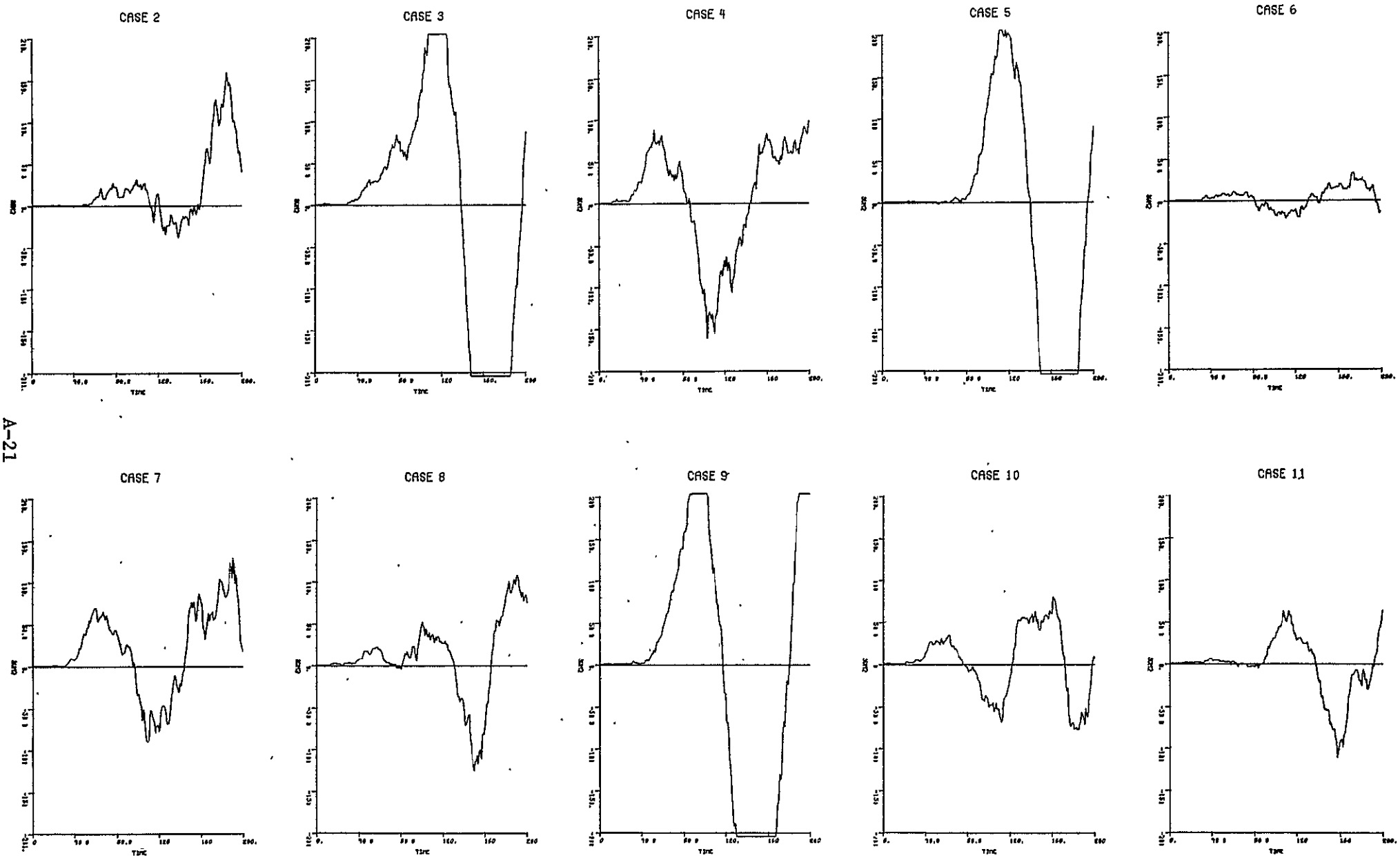

Fig. A-16. Final Waveforms for 10 Simulated Cases of Double-Delay Differencing Operations, SNR = 20 db, ACF = $e^{-.125}$ (New Random Numbers)

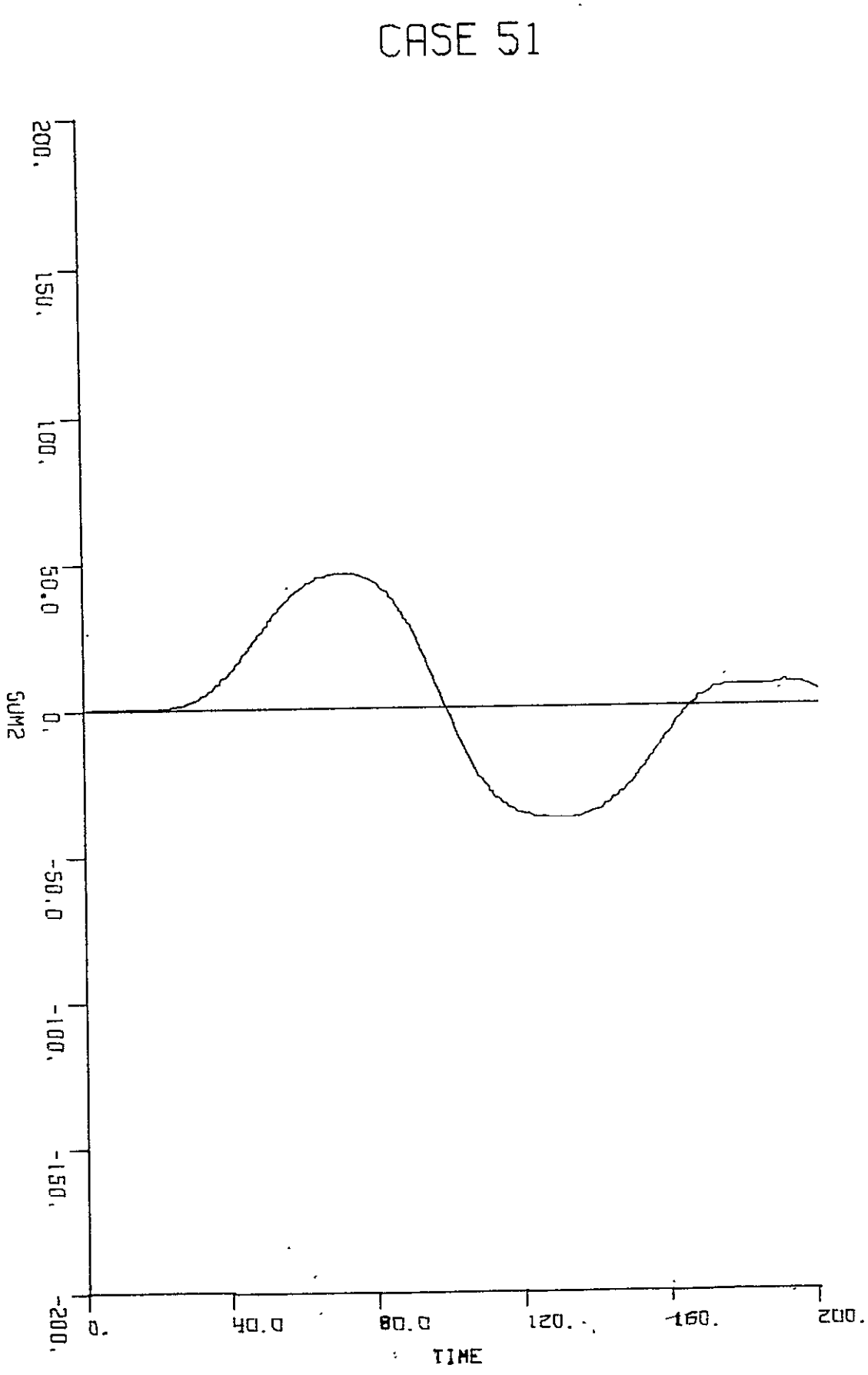

Fig. A-17. Double-Delay Differencer Output When Input is Average of 50 Waveforms, SNR = ∞

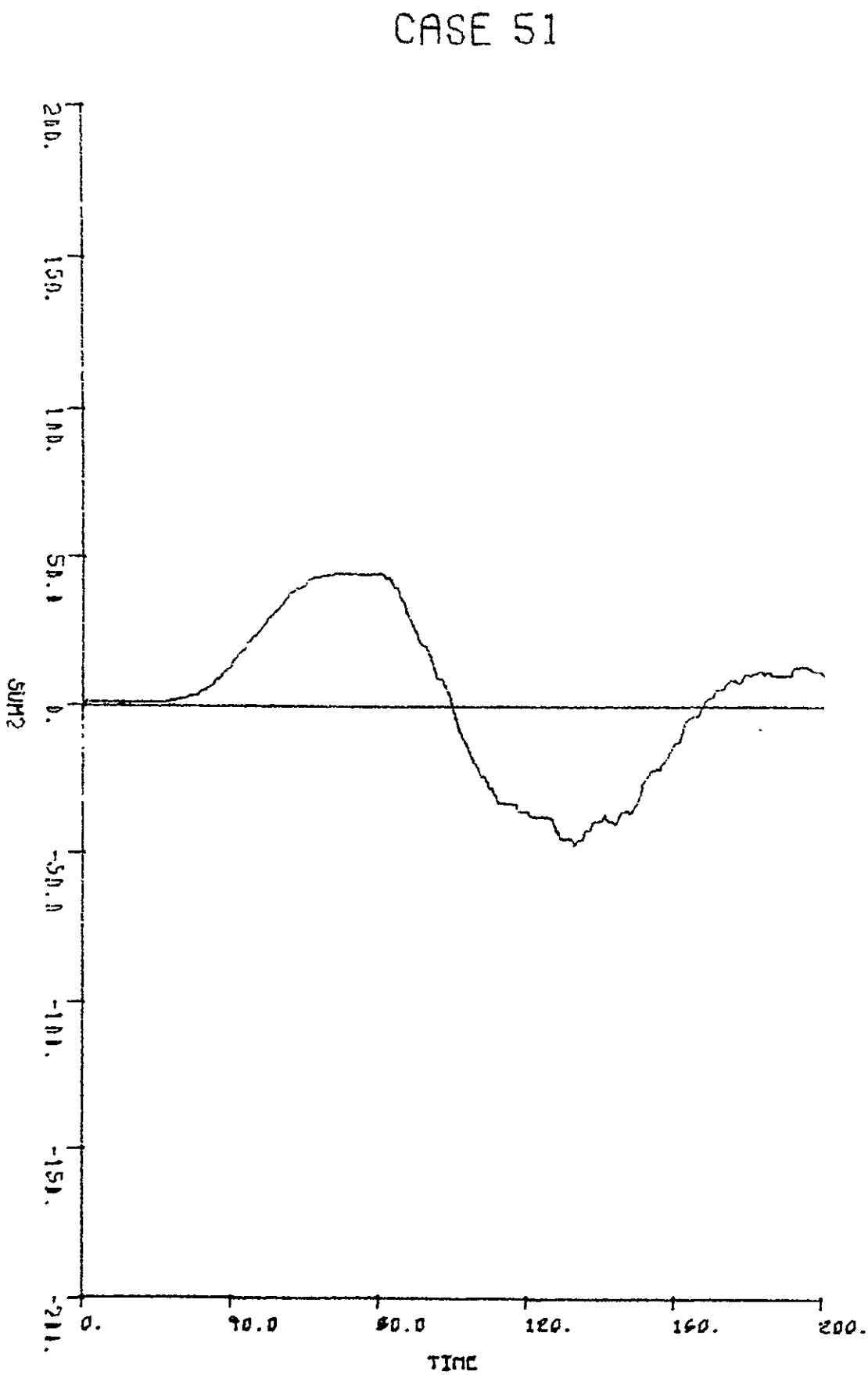

Fig. A-18. Double-Delay Differencer Output When Input is Average of 50 Waveforms, SNR = 20 db

Figures A-19 through A-26 show the results obtained by averaging 50 individual waveforms, for various signal and noise conditions.

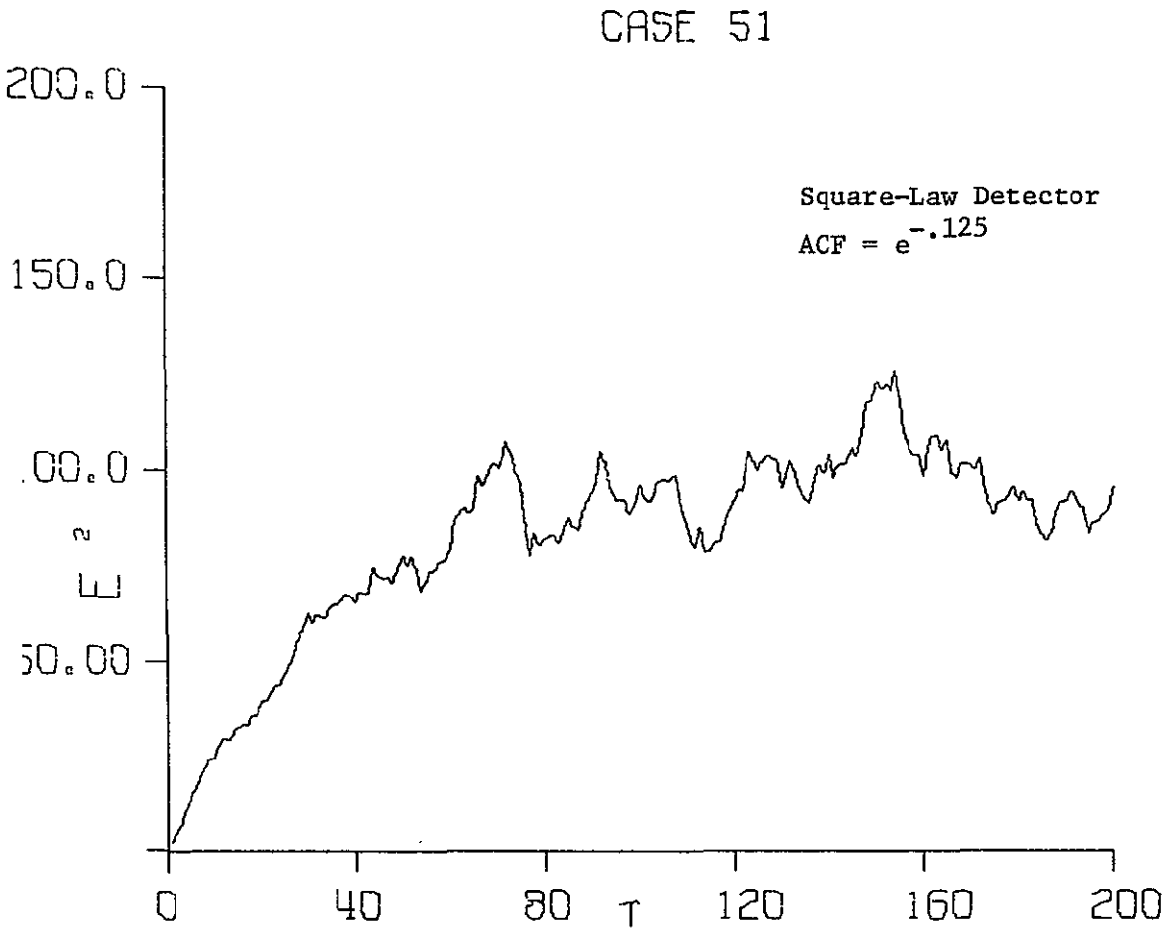

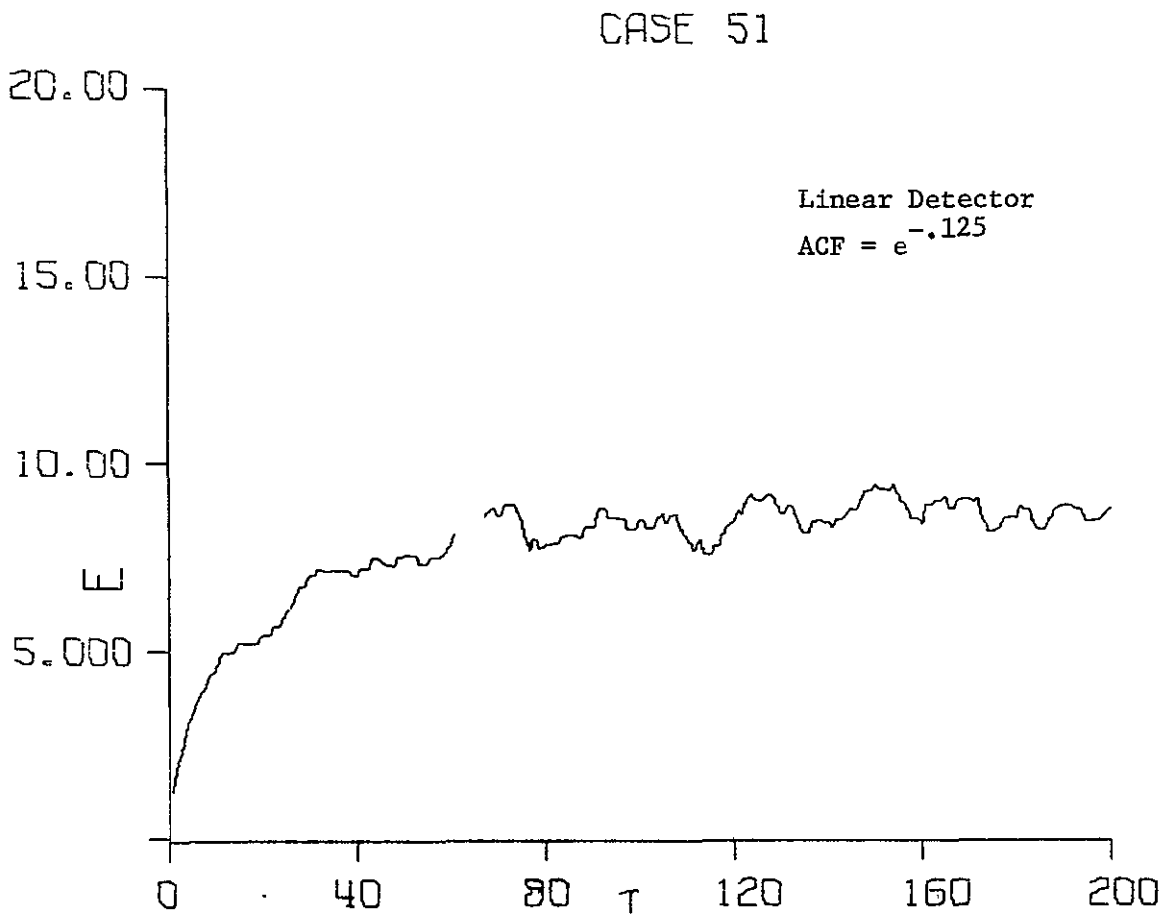

Fig. A-19. Averaged Waveform for Rectangular Pulse, SNR = ∞ (50 Cases)

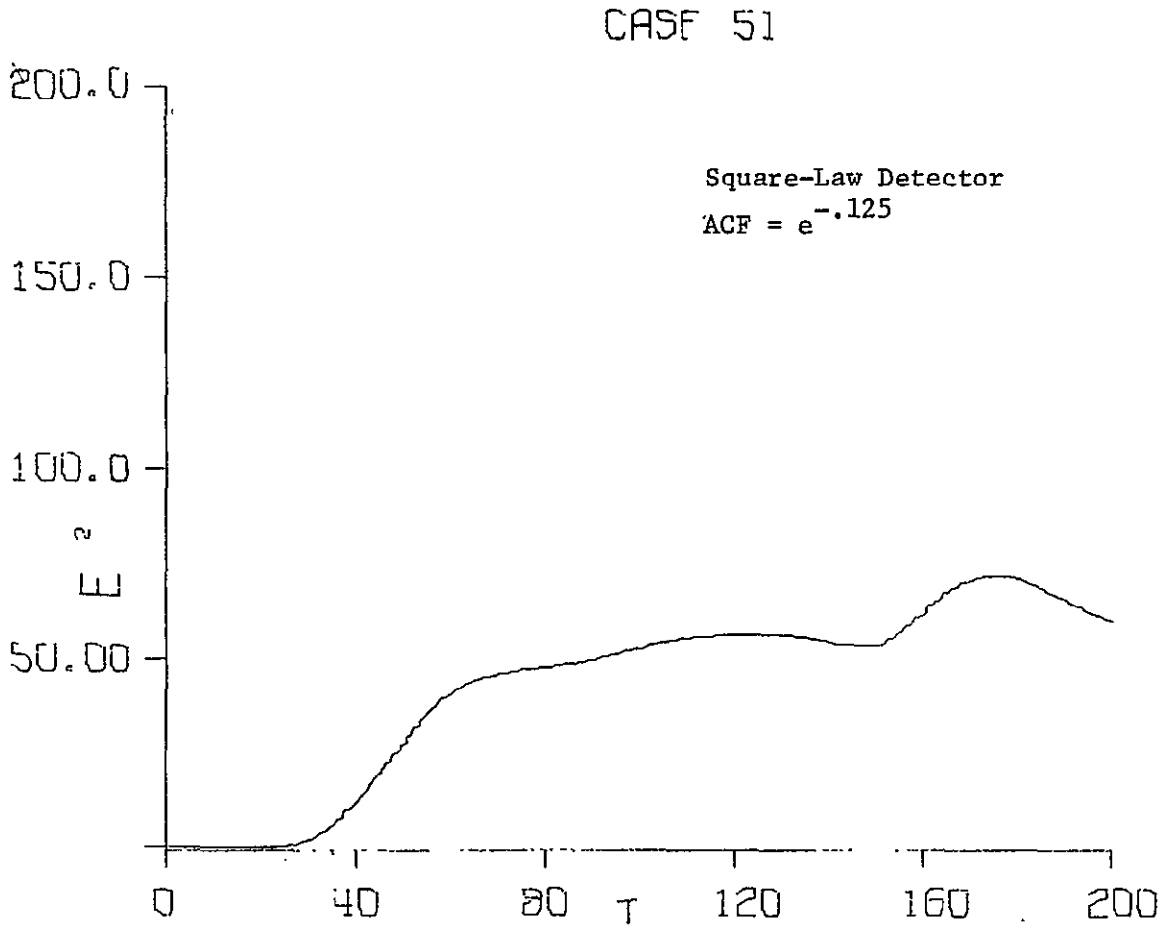

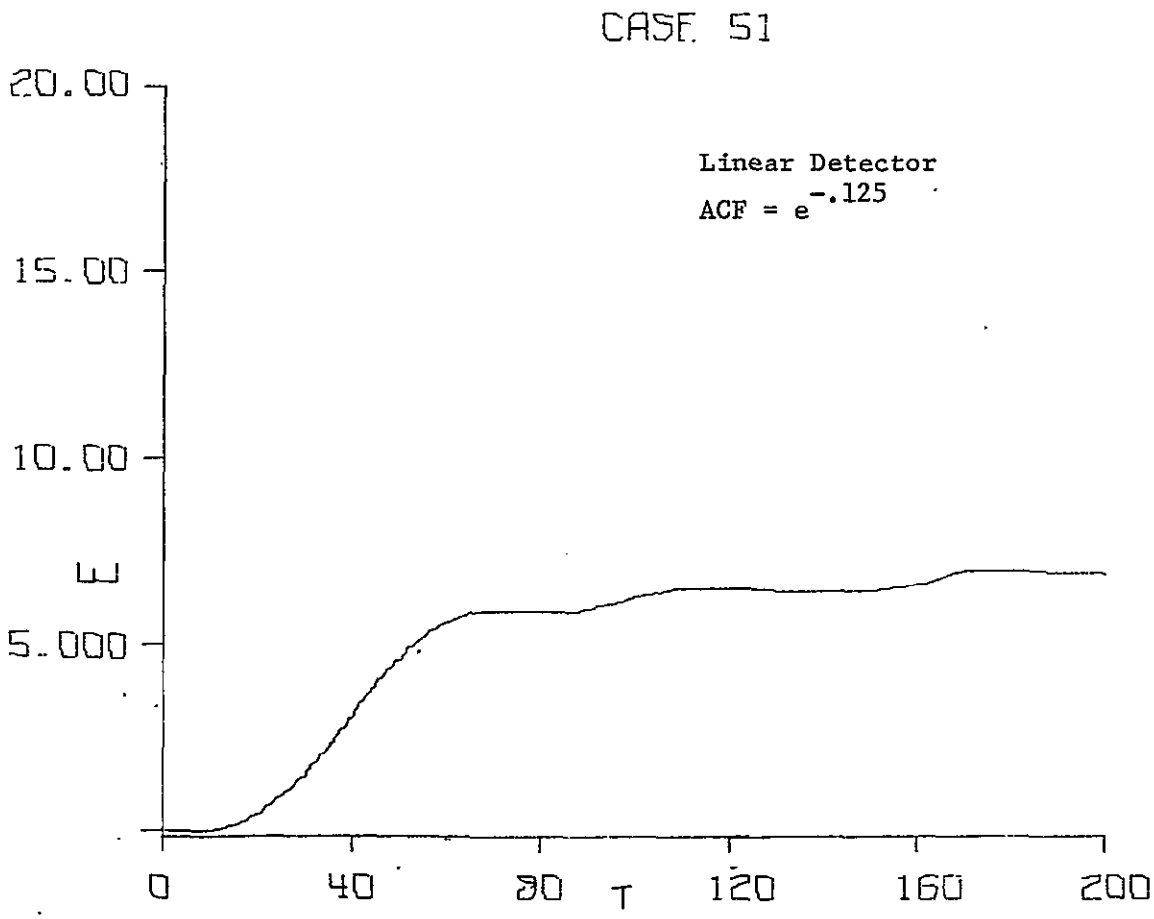

Fig. A-20. Averaged Waveform for Gaussian Pulse, SNR = ∞ (50 Cases)

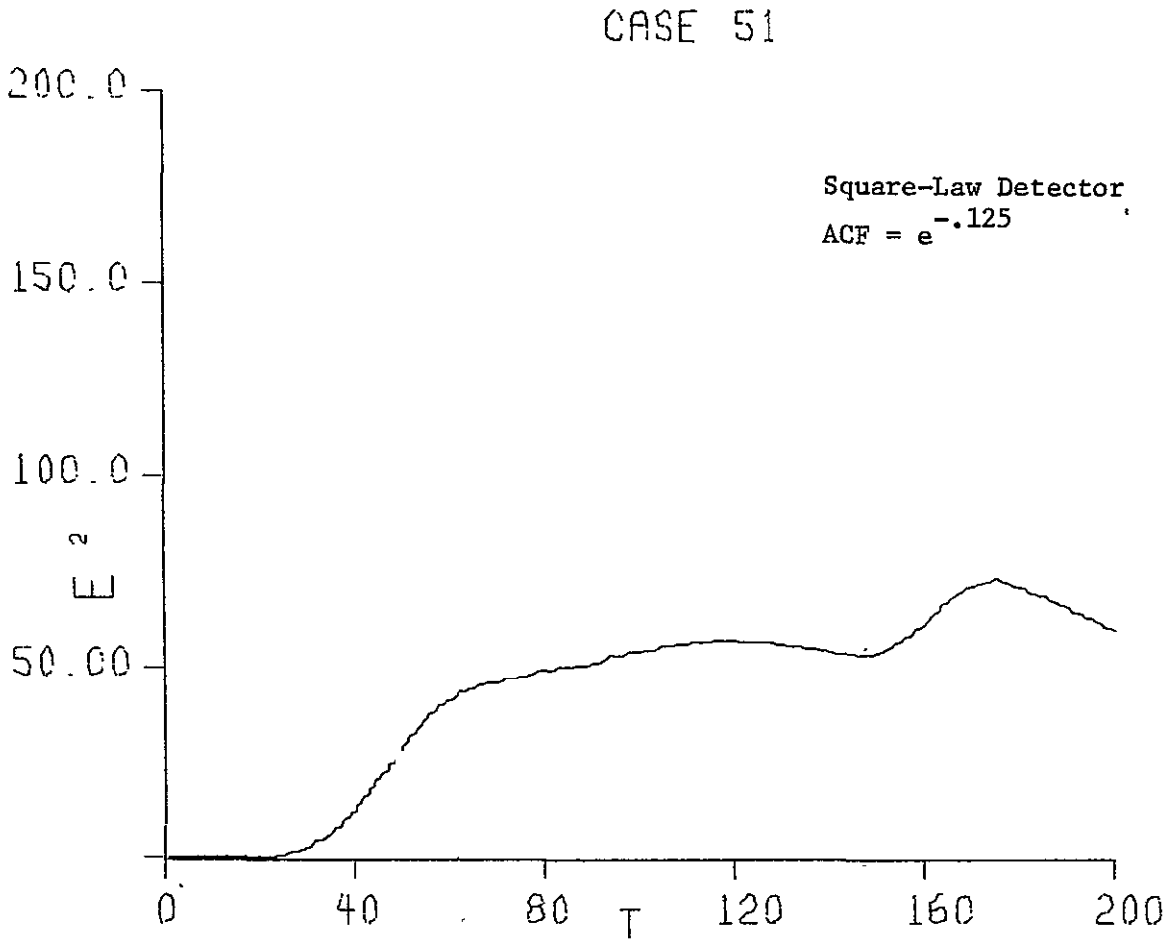

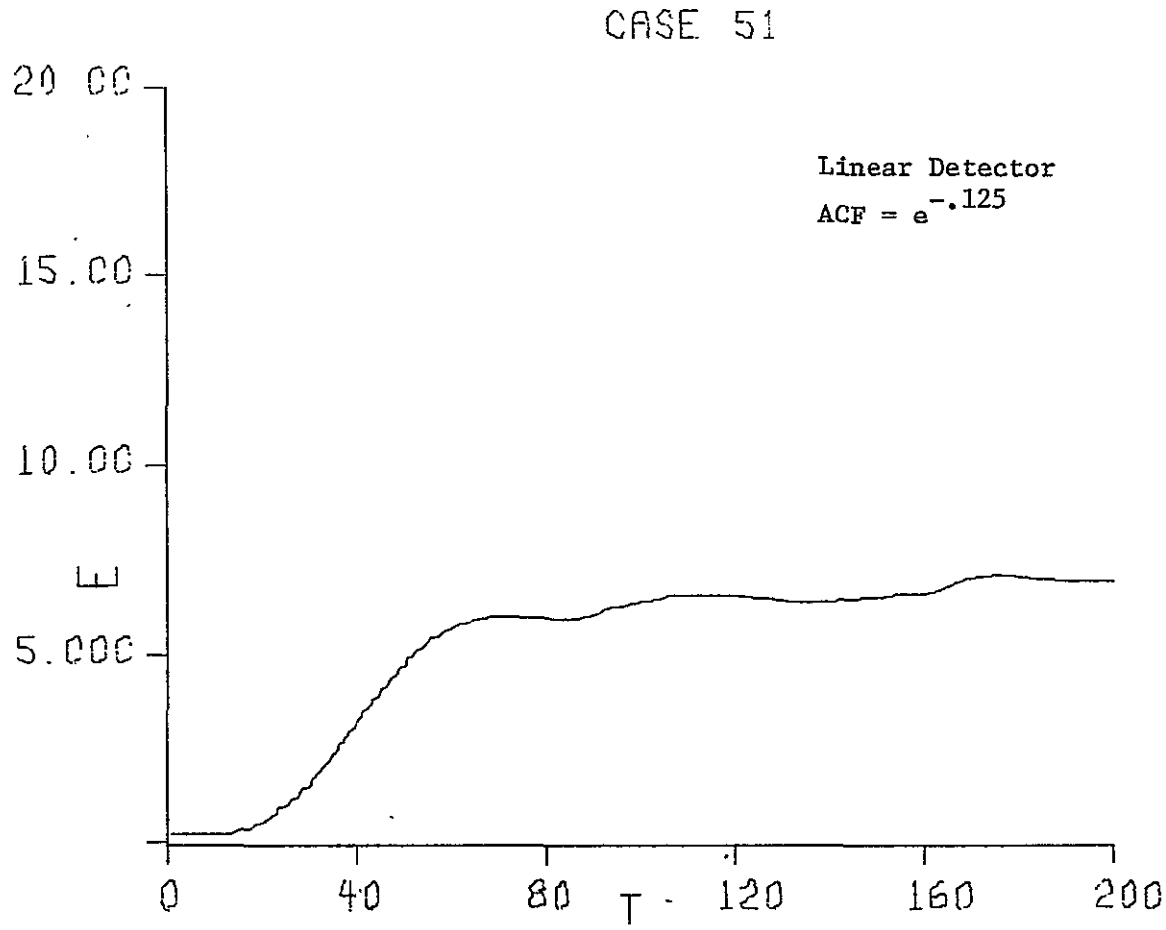

Fig. A-21. Averaged Waveform for Gaussian Pulse, SNR = 30 db (50 Cases)

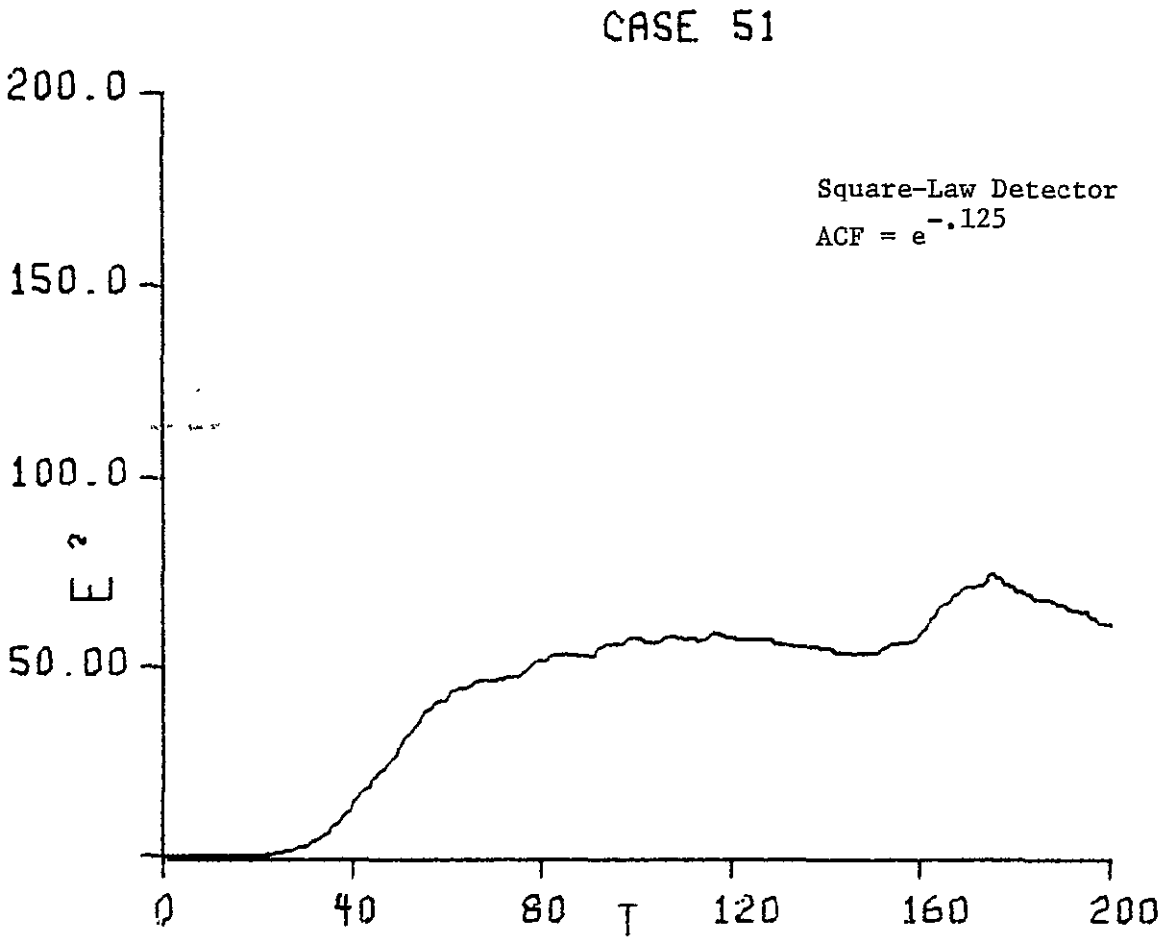

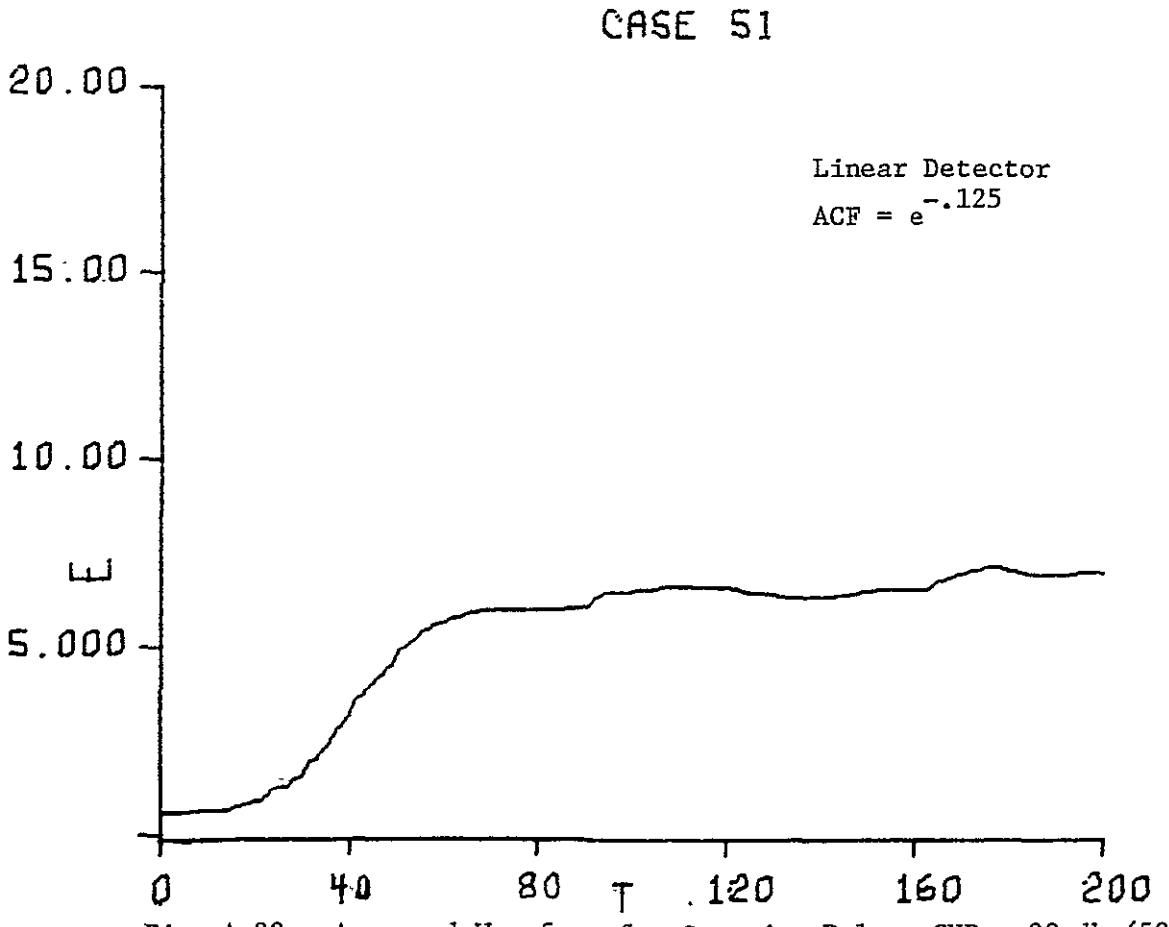

Fig. A-22. Averaged Waveform for Gaussian Pulse, SNR = 20 db (50 Cases)

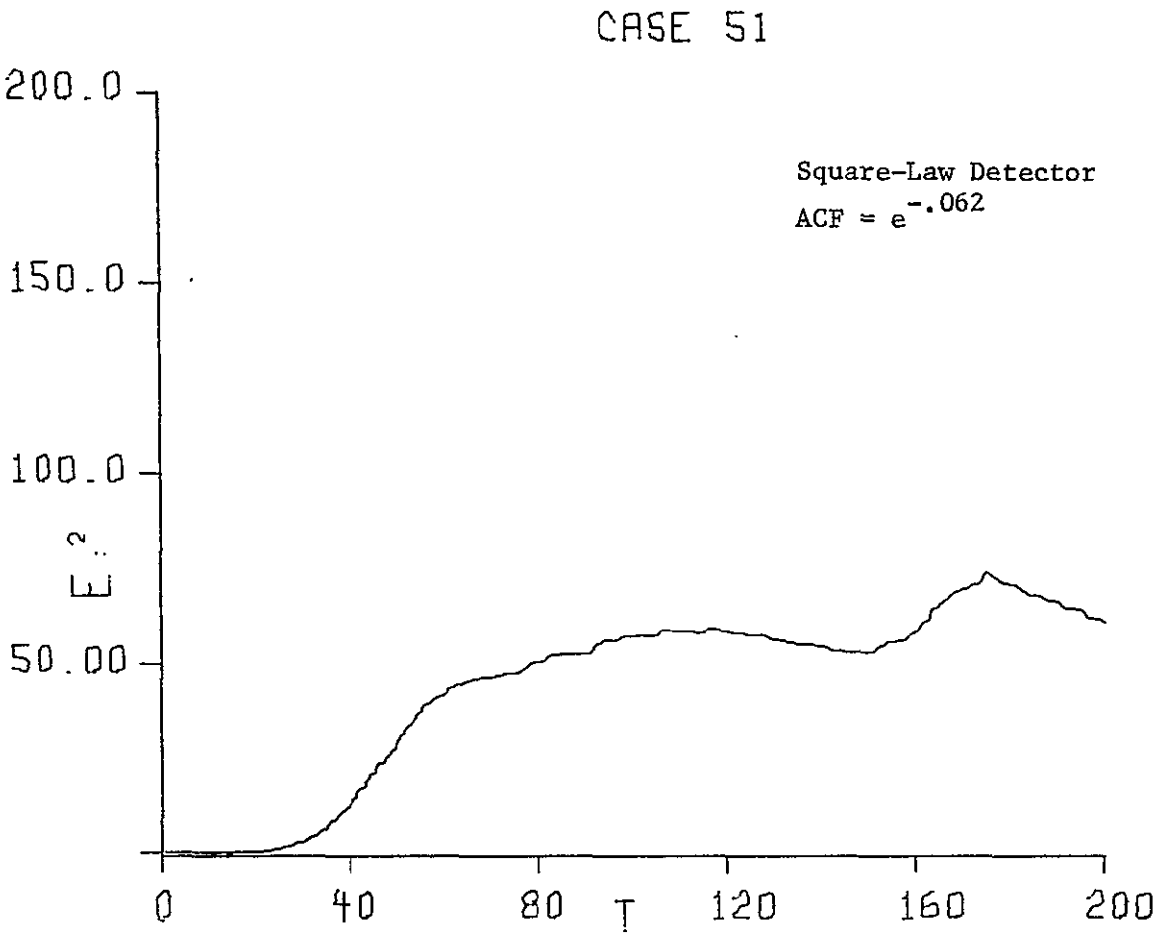

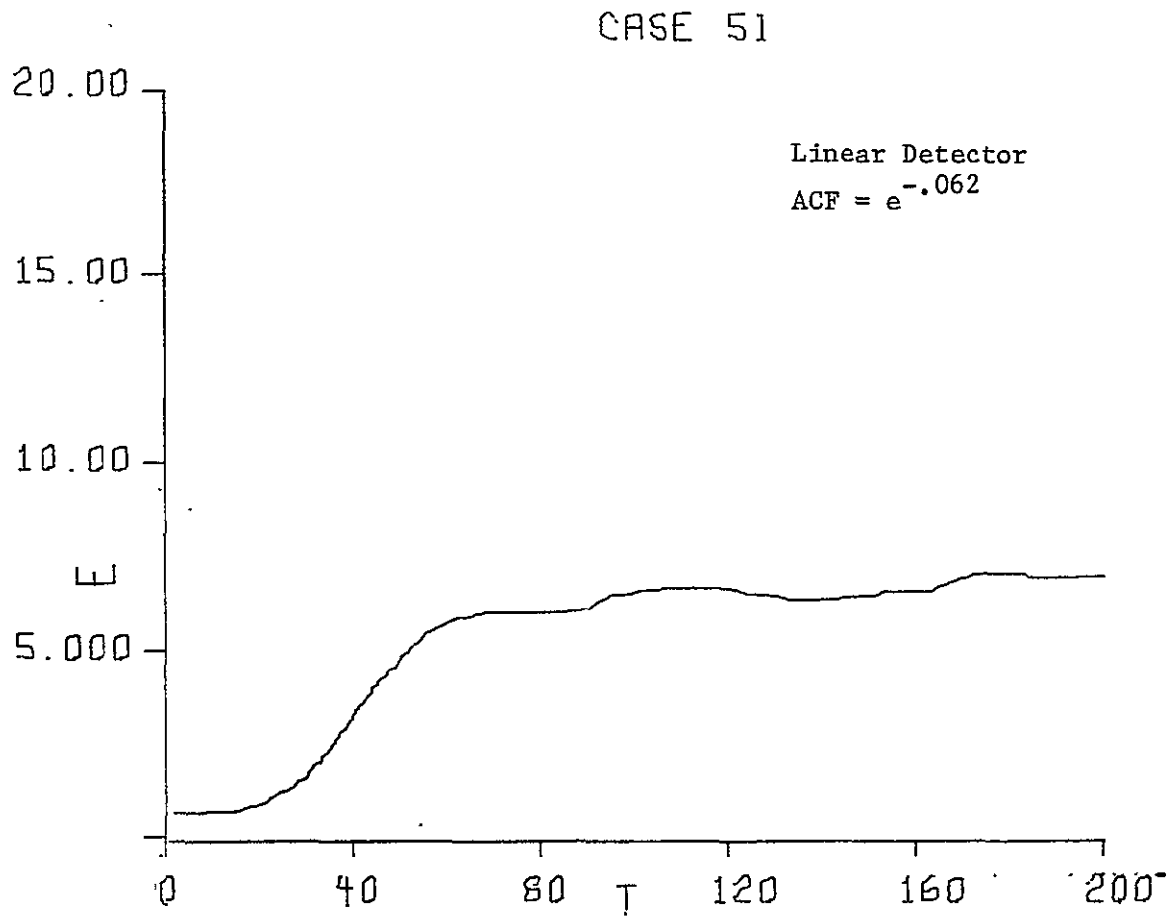

Fig. A-23. Averaged Waveform for Gaussian Pulse, SNR = 20 db (50 Cases)

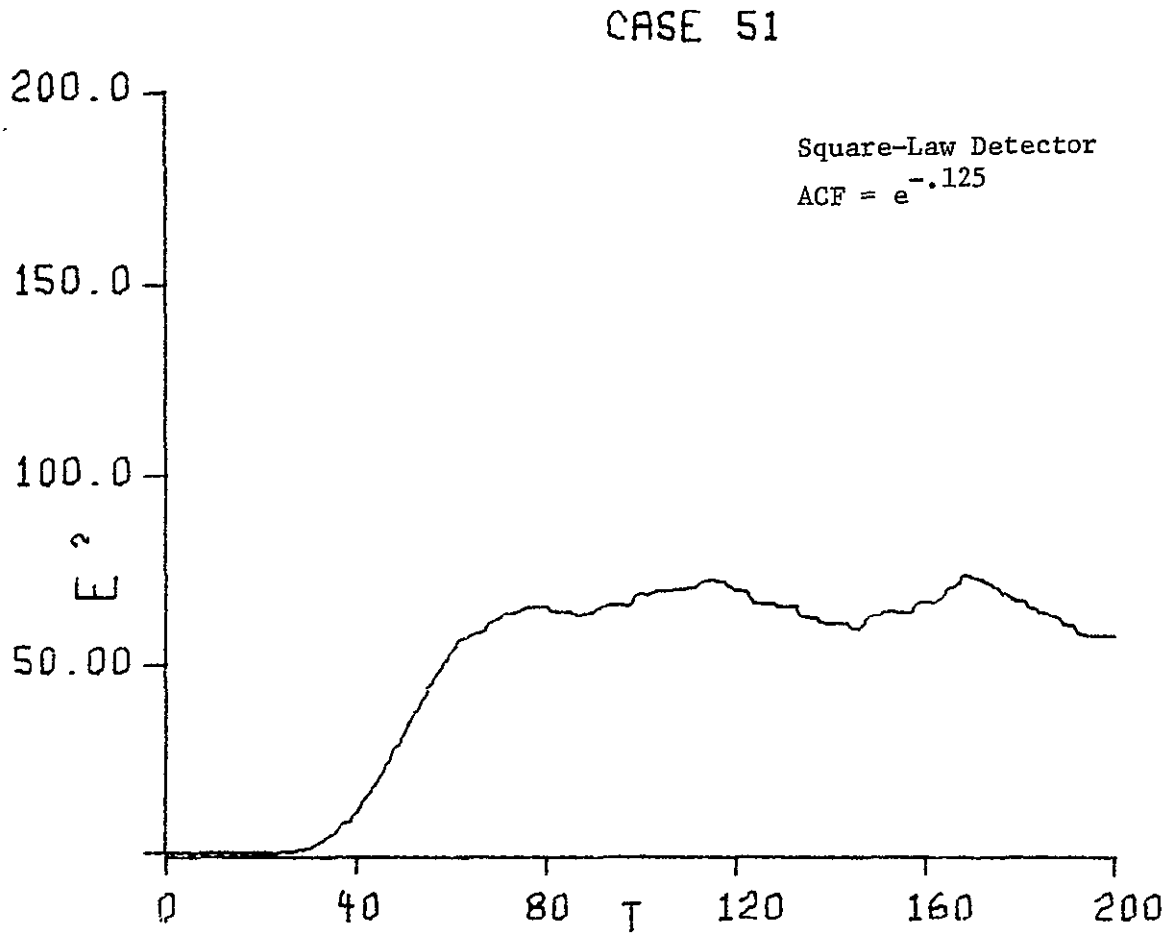

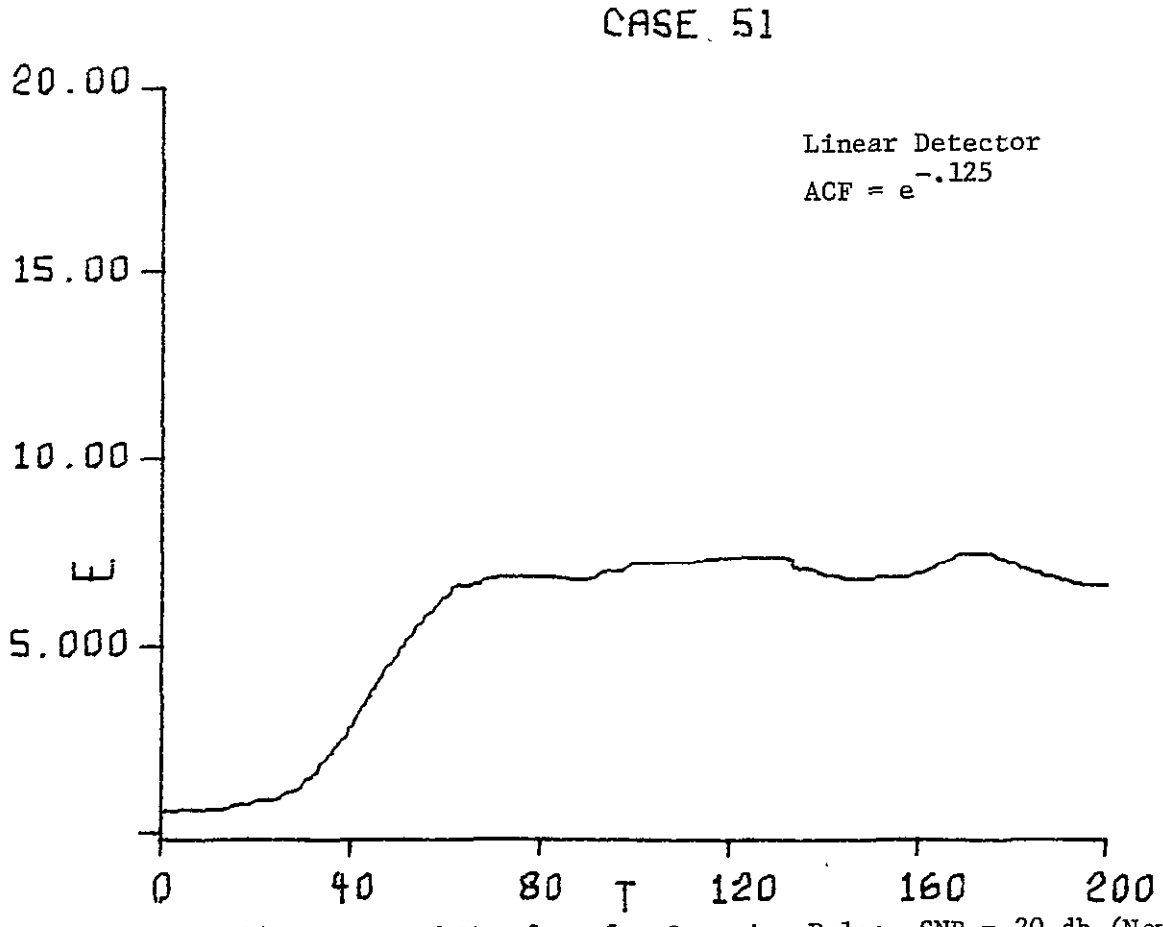

Fig. A-24. Averaged Waveform for Gaussian Pulse, SNR = 20 db (New Random Numbers, 50 Cases)

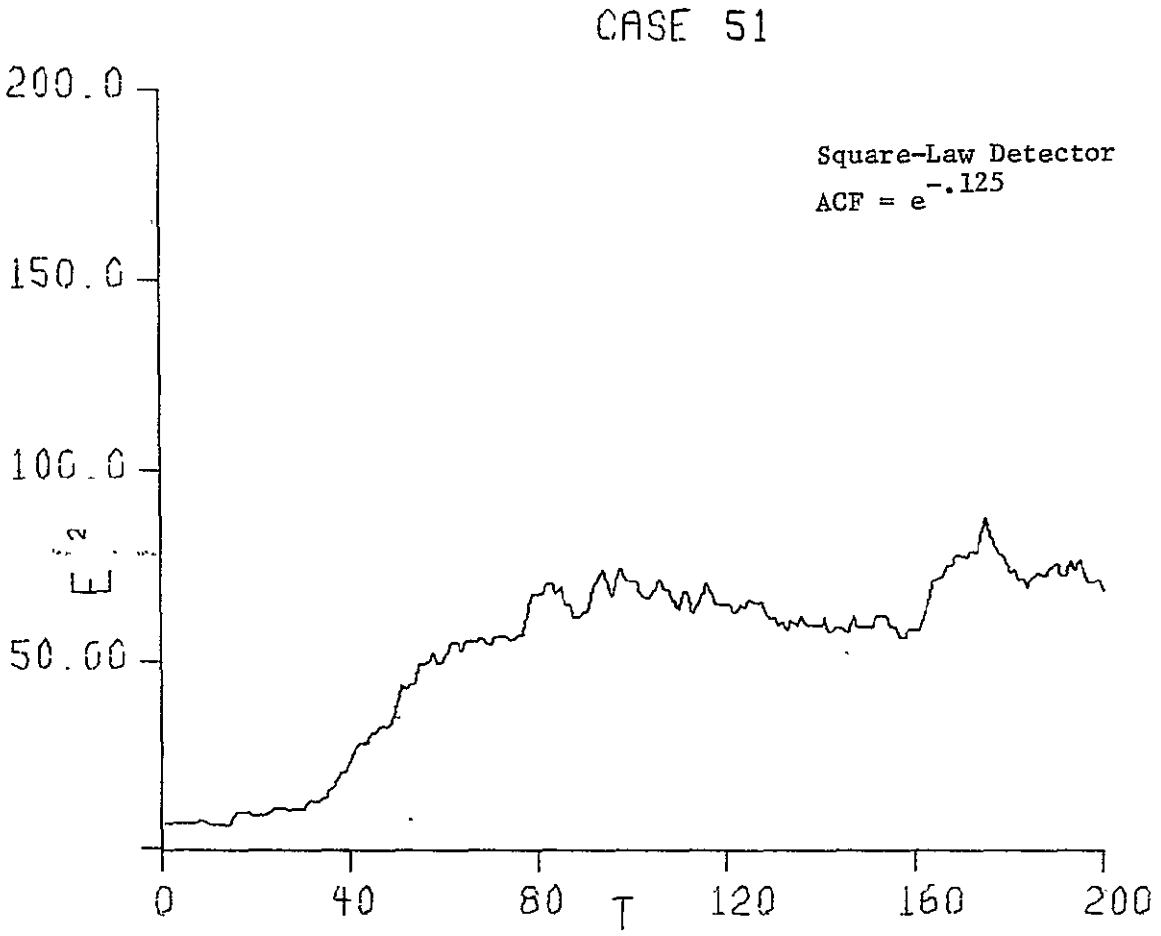

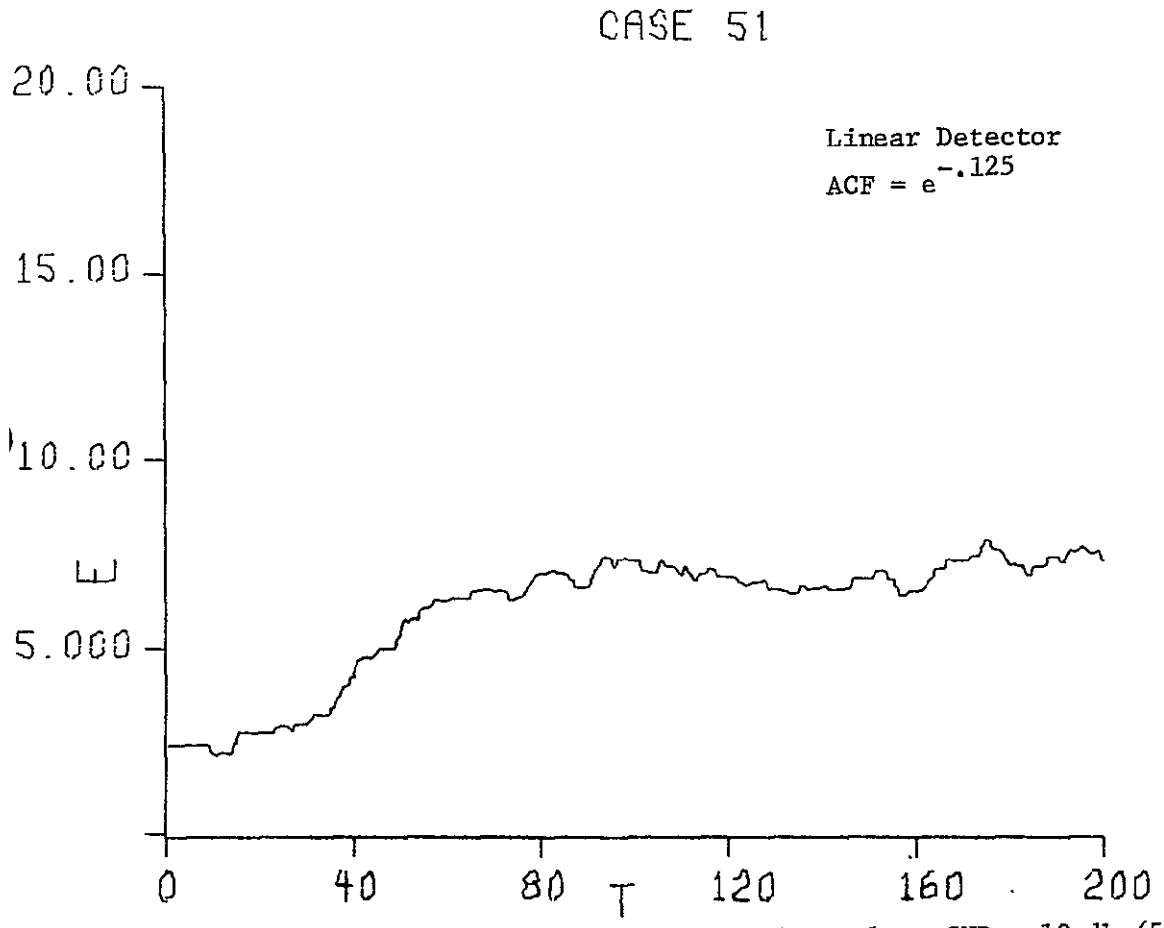

Fig. A-25. Averaged Waveform for Gaussian Pulse, SNR = 10 db (50 Cases)

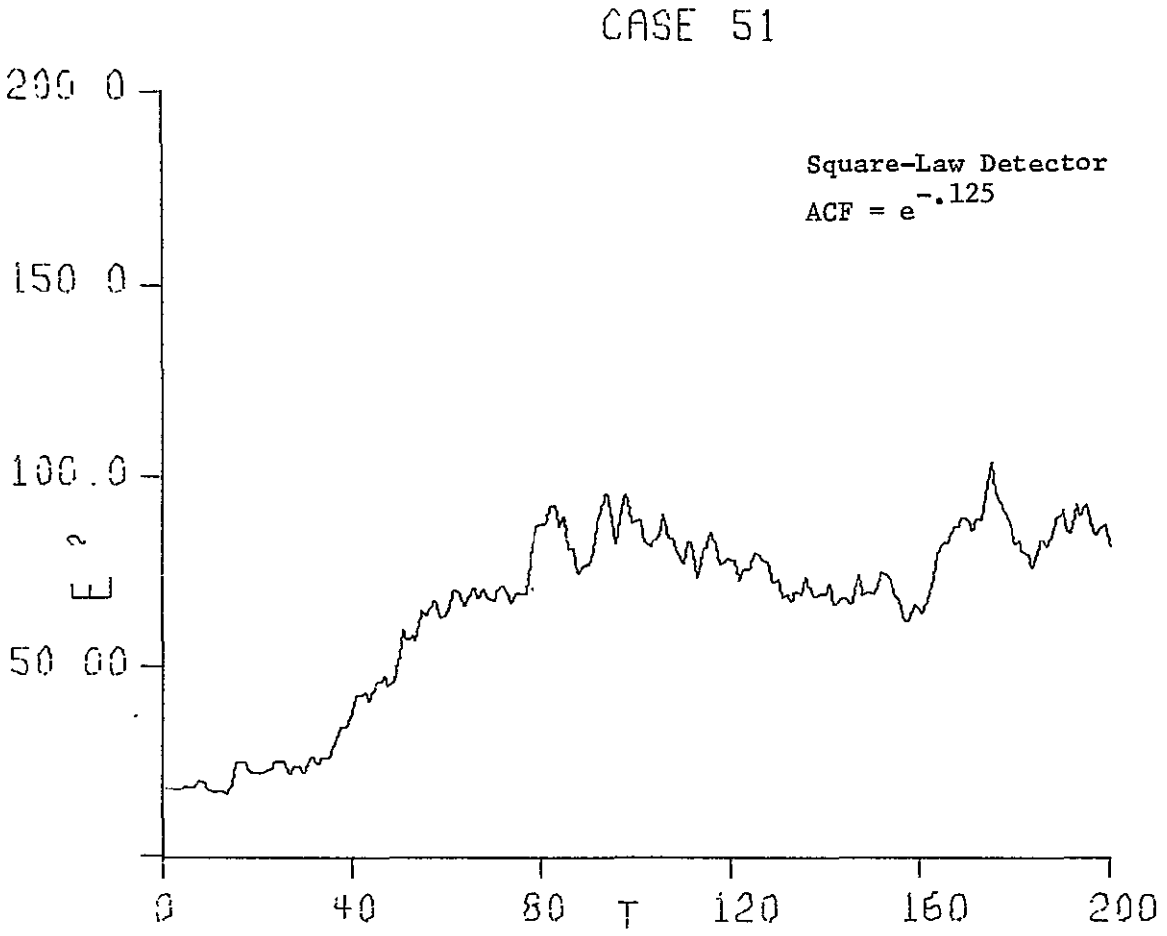

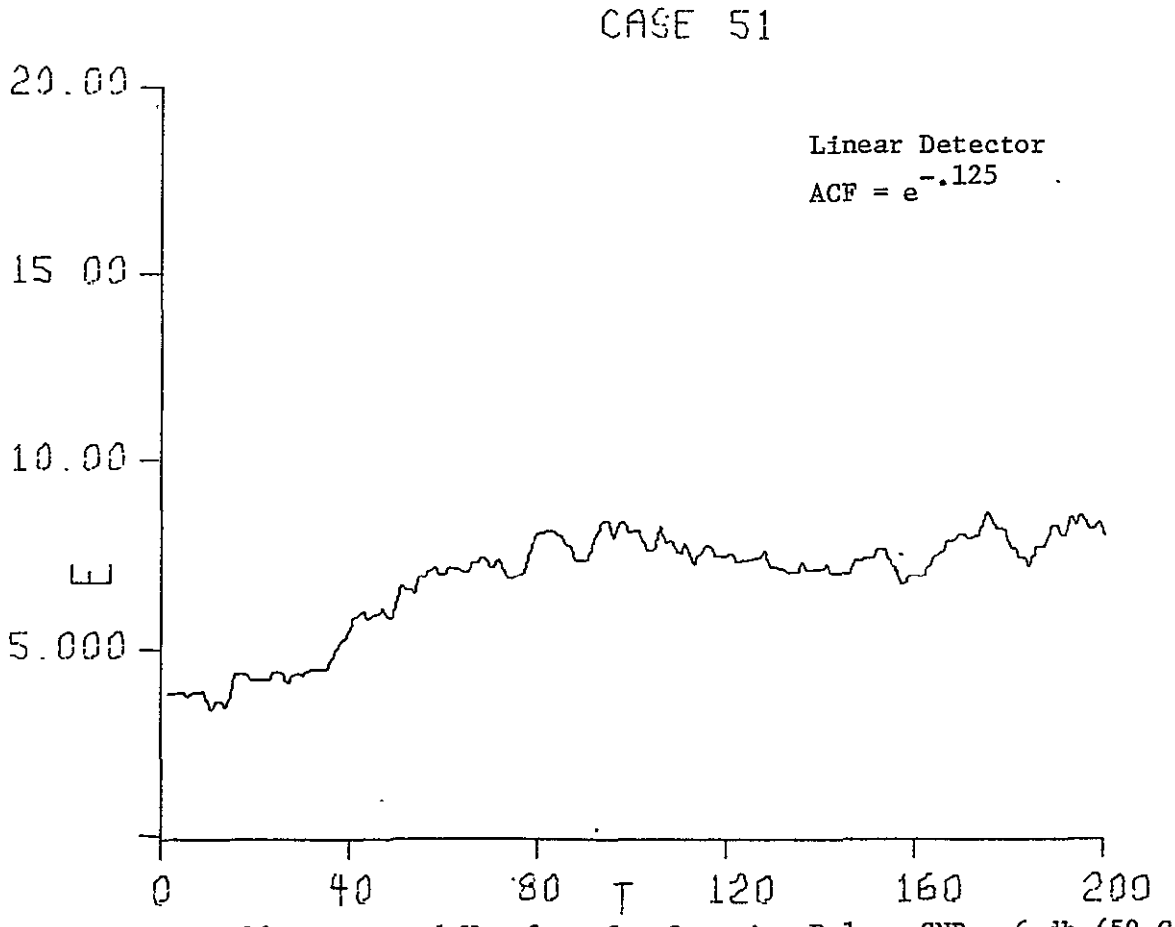

Fig. A-26. Averaged Waveform for Gaussian Pulse, SNR = 6 db (50 Cases)

APPENDIX B

THEORETICAL ALTITUDE MEASUREMENT ANALYSIS

This appendix contains the results of a theoretical analysis of altitude errors for a double-delay processor type of altimeter. The transient region of the sea-return signal is modeled by the technique shown in Fig. B-1.

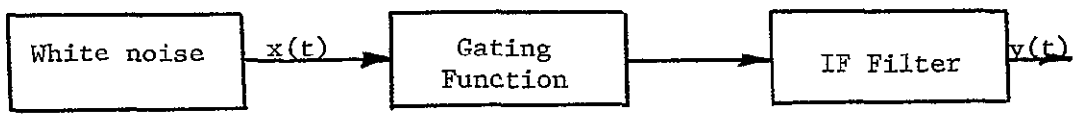

Fig. B-1. Signal generation model.

This signal is then combined with thermal noise, fed into a square law detector, and finally processed by a double-delay differencer and zero-crossing extractor. Exponential type autocorrelations were used in the analysis because of the difficulty in obtaining closed-form expressions with other functions such as the Gaussian. The purpose of the signal model (Fig. B-1) is to account for pre-detection filtering characteristics in the return signal. These details will be given first.

Referring to Fig. B-1, the input autocorrelation function for the noise is assumed to be

$$R_{xx}(t_1,t_2) = S_o\delta(t_1-t_2) \qquad 0 \leq t_1,t_2 \leq T \ . \tag{B-1}$$

The output of the gating function is nonstationary noise with the properties

$$S_o\ \delta(t_1 - t_2)\ U(t_1)\ U(t_2) \qquad 0 \leq t_1,t_2 \leq \infty \tag{B-2}$$

where $U(\cdot)$ is the unit step function. For an IF filter impulse response $e^{-\alpha t}\,U(t)$, the output correlation $R_{yy}(t_1,t_2)$ is given by

$$R_{yx}(t_1,t_2) = S_o \int_{-\infty}^{+\infty} \delta(t_1-\tau-t_2)\; U(t_1-\tau)\; U(t_2)\; e^{-\alpha\tau}\; U(\tau)\; d\tau \qquad \text{(B-3)}$$

(t_1 variable)

$$= S_o U(t_2)\;\; e^{-\alpha(t_1-t_2)}\; U(t_1-t_2)\;,$$

$$R_{yx}(t_1,t_2) = S_o e^{-\alpha(t_1-t_2)}\; U(t_1-t_2)\; U(t_2)\;, \qquad \text{(B-4)}$$

$$R_{yy}(t_1,t_2) = S_o \int_{-\infty}^{+\infty} e^{-\alpha(t_1-t_2+\tau)}\; U(t_1-t_2+\tau)\; U(t_2-\tau) e^{-\alpha\tau}\; U(\tau)\; d\tau\;,$$

(t_2 variable)

and

$$R_{yy}(t_1,t_2) = S_o e^{-\alpha(t_1-t_2)} \int_{-\infty}^{+\infty} e^{-2\alpha\tau}\; U(t_1-t_2+\tau)\; U(t_2-\tau)\; U(\tau)\; d\tau \qquad \text{(B-5)}$$

where

$U(t_1-t_2+\tau) \rightarrow U(.) = 1$ for $\tau > t_2-t_1$

$U(t_2-\tau) \rightarrow U(.) = 1$ for $\tau < t_2$

$U(\tau) \rightarrow U(.) = 1$ for $\tau > 0$.

The integration of (B-5) gives,

$$R_{yy}(t_1,t_2) = S_o \frac{e^{-\alpha(t_1-t_2)}}{-2\alpha}\; e^{-2\alpha\tau}\Big|_{o}^{t_2}$$

$$= S_o \frac{e^{-\alpha t_1}}{\alpha}\left[\frac{e^{\alpha t_2}-e^{-\alpha t_2}}{2}\right]; \quad t_1 > t_2$$

and

$$R_{yy}(t_1,t_2) = S_o \frac{e^{-\alpha(t_1-t_2)}}{-2\alpha} e^{-2\alpha\tau} \Bigg|_{t_2-t_1}^{t_2}$$

$$= S_o \frac{e^{-\alpha t_2}}{\alpha} \left[\frac{e^{\alpha t_1} - e^{-\alpha t_1}}{2}\right]; \quad t_2 > t_1 .$$

Further Algebraic substitution yields the result,

$$R_{yy}(t_1,t_2) = S_o e^{-\alpha t_1} \sinh \alpha t_2; \quad t_2 < t_1 \tag{B-6}$$

$$= S_o e^{-\alpha t_2} \sinh \alpha t_1; \quad t_1 < t_2 .$$

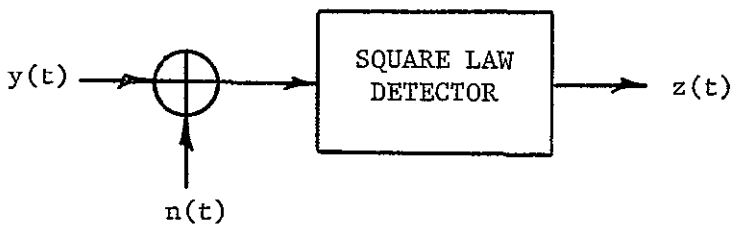

Fig. B-2. Detector model.

Assuming that the signal is a (non-stationary) narrow-band Gaussian process to which the thermal noise

$$R_{nn}(\tau) = N_o e^{-\beta|\tau|} \tag{B-7}$$

is added, the output of the square-law detector z(t) (see Fig. B-2) is derived as follows:

$$z(t) = [y(t) + n(t)]^2$$

$$R_{zz}(t_1,t_2) = E\{z(t_1)\ z(t_2)\}$$

$$= E\{[y(t_1) + n(t_1)]^2\ [y(t_2) + n(t_2)]^2\}$$

$$= E\{y^2(t_1)\ y^2(t_2) + 2y^2(t_1)\ n(t_2)y(t_2) + y^2(t_1)n^2(t_2)$$

$$+ 2n(t_1)\ y(t_1)\ y^2(t_2) + 4n(t_1)\ n(t_2)y(t_1)\ y(t_2) + 2n(t_1)y(t_1)\ n^2($$

$$+ n^2(t_1)\ y^2(t_2) + 2n^2(t_1)\ n(t_2)\ y(t_2) + n^2(t_1)\ n^2(t_2)\}$$

$$= E\{y^2(t_1)\}\ E\{\ y^2(t_2)\} + 2E^2\ \{y(t_1)\ y(t_2)\}$$

$$+ E\{y^2(t_1)\}\ E\ \{n^2(t_2)\} + 2E^2\ \{y(t_1)\ n(t_2)\}$$

$$+ 4E\ \{n(t_1)\ n(t_2)\}\ E\ \{y(t_1)\ y(t_2)\}$$

$$+ E\{n^2(t_1)\}\ E\ \{y^2(t_2) + 2E^2\{n(t_1)\ y(t_2)\}$$

$$+ E\{n^2(t_1)\}\ E\ \{n^2(t_2)\} + 2E^2\{n(t_1)\ n(t_2)\}$$

Note: indicates uncorrelated term.

$$\boxed{\begin{aligned} R_{zz}(t_1,t_2) &= R_{yy}(t_1,t_1)\ R_{yy}(t_2,t_2) + 2R_{yy}^{\ 2}\ (t_1,t_2) \\ &+ N_o R_{yy}(t_1,t_1) + 4R_{nn}(t_1,t_2)\ R_{yy}\ (t_1,t_2) \\ &+ N_o R_{yy}(t_2,t_2) + N_o^{\ 2} + 2\ R_{nn}^{\ 2}\ (t_1,t_2) \end{aligned}} \qquad \text{(B-8)}$$

Collecting the previous results, the mean square output of Square Law Detector is

$$\overline{z^2} = 3S_o^2 \left[\frac{1}{\alpha} e^{-\alpha t} \sinh \alpha t\right]^2 + \frac{6S_oN_o}{\alpha} e^{-\alpha t} \sinh \alpha t + 3N_o^2 . \qquad \text{(B-9)}$$

The signal-to-noise ratio (SNR) at detector output is,

$$\text{SNR} = \frac{\left(\frac{S_o}{N_o}\right)\left[\frac{1}{\alpha} e^{-\alpha t} \sinh \alpha t\right]^2}{2\left(\frac{S_o}{N_o}\right)\left[\frac{1}{\alpha} e^{-\alpha t} \sinh \alpha t\right] + 1} . \qquad \text{(B-10)}$$

Some of the above results have been given for purposes of documentation. The autocorrelation at the output of the double-delay differencer is readily derived, however, the zero-crossing solution has not been obtained. Approximate results will now be discussed.

Referring to the idealized waveforms shown in Fig. B-3, the variance at the instant of zero-crossing can be estimated as follows:

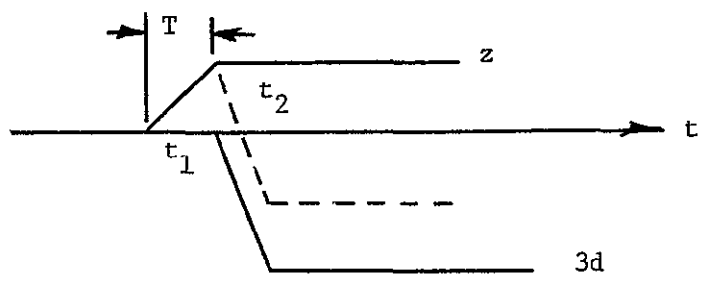

Figure B-3. Differencer characteristic.

Only two stages of the differencing operation are necessary for the discussion. The variance at the point zero crossing t_2 is for $t_2 > t_1$,

$$
\begin{aligned}
&E\{[z(t_2) - 2z(t_1)]^2\} - E^2\{z(t_2) - 2z(t_1)\} \\
&\quad = E\{z^2(t_2)\} - E^2\{z(t_2)\} - 2E\{z(t_1)\, z(t_2)\} \\
&\quad + 4\,[E\{z^2(t_1)\} - E^2\{z(t_1)\} + 2E\{z(t_1)\}\, E\{z(t_2)\} \\
&\quad = R_{zz}(t_2,t_2) - 2R_{zz}(t_1,t_2) + 4\, R_{zz}(t_1,t_1) \\
&\quad - \mu_z^2(t_2) - 4\mu_z^2(t_1) + 2\,\mu_z(t_1)\,\mu_z(t_2)
\end{aligned}
\tag{B-11}
$$

where μ_z is the mean value, i.e.,

$$
\mu_z(t) = \frac{S_o}{\alpha}\, e^{-\alpha t} \sinh \alpha t + N_o \quad . \tag{B-12}
$$

Substituting from (6), (8) and (9) with

$$
t_1 = \frac{T}{2}; \quad t_2 = \frac{3T}{2}
$$

and for the matched conditions,

$$
T = \frac{1}{\alpha}
$$

the variance at the zero crossing normalized to a unit mean value is

$$
\sigma_{zc}^2 \cong 2.7S_o^{\,2} + 38S_oN_o + 31.6N_o^{\,2} \quad . \tag{B-13}
$$

This amplitude variance can be scaled to a time variance as

$$
\sigma_t = \sigma_{zc} \overline{\left(\frac{dv}{dt}\right)}^{-1}
$$

where the mean slope $\overline{\left(\frac{dv}{dt}\right)}^{-1}$ is from Fig. B-3 approximately $\frac{T}{2}$/volt (T = pulse length, in n.s.). Using an altitude uncertainty of

$$\sigma_a = \frac{c\tau}{2} \sigma_t$$

the final altitude error estimate is

$$\sigma_a \cong \frac{0.15T}{\sqrt{n}} \sqrt{0.68 + 9.5(SNR)^{-1} + 7.9\ (SNR)^{-2}} \qquad \text{(B-14)}$$

where n is the number of samples.

Appendix C

This appendix presents the results of a brief survey of prior work in estimation theory from the standpoint of the altimeter problem. The objective of the survey is to compare optimum* altitude extraction schemes with the ad hoc threshold, split-gate, and delay differencing techniques. Since the altimeter signal constitutes return from the sea-surface with simultaneous range and doppler spreading, the target scattering function $\sigma(\tau, f)$ approach is adopted. The received signal characteristics are considered prior to discussing optimal processing techniques.

The basis for assuming that the scattered signal fluctuations will be Rayleigh distributed (at the output of a linear detector) was discussed in Section III of this report. The physical modeling of the scattering process relative to a first-order convolutional model of the altimeter signal can be established as follows: The signal s(t) reflected from a small region of the sea-surface, with a two-way time delay τ_n, will be a sample function of the clutter process, i.e.,

$$s_n(t) = \sigma_n s(t-\tau_n) \tag{1}$$

where σ_n, is proportional to the scattering magnitude and inversly proportional to range squared, within the region illuminated. The total received signal during a time interval T is obtained by summing terms i.e.,

$$s_o(t) = \sum_{n=1}^{N} \sigma_n \, s(t-\tau_n) \quad -\frac{T}{2} \leq \tau_n \leq \frac{T}{2} \quad . \tag{2}$$

Since

$$s(t) * \delta(t-\tau) = \int_{-\infty}^{\infty} s(t), \; \delta(t-t_1-\tau) \, dt_1 = s(t-\tau)$$

this result can be expressed as the convolution (*) of s(t) with an impulse train $\delta(t-\tau_n)$.

---

*"optimum" in the sense that some index of performance is minimized (or maximized).

Therefore

$$s_o(t) = \sum_{n=1}^{N} \sigma_n \; s(t) * \delta(t-\tau_n) \; , \tag{3}$$

which can formally be written as

$$s_o(t) = s(t) * \sum_{n=1}^{N} \sigma_n \; \delta(t-\tau_n) \; . \tag{4}$$

This last form places in evidence the impulse response nature of the sea return. The impulse response will be non-stationary if the range (or time) dependence of the σ_n's is taken into account. The stationary assumption should certainly be valid for the altimeter problem. Equation 4 shows that the impulse response of the sea surface can be conceptualized as arising from a collection of discrete reflectors of sizes σ_n and delay t_n. This is essentially the concept used in the simulation. Use of terms such as <u>impulse response</u> of spread function to describe sea scattering are not precise, since these idealizations can be described in the mean only. Also, the impulse response cannot be rigorously defined in terms of scatter obtained by illuminating an infinitesimal <u>area</u> containing a normal incidence diffraction element. Equation 4 is therefore considered to consist of a convolution of a signal with a pseudo-impulse response.

For the altimeter problem, the clutter impulse response from (4) is

$$h_c(t) = \sum_{n=1}^{N} \sigma_n \; \delta(t-\tau_n). \tag{5}$$

Ocean surface correlation has been neglected thus far in the discussion. Arguments given in Section IV indicate that the sea return correlation time at the altimeter can be less than one nanosecond. Therefore, for the present purposes the delta function concept will be valid for time-increments of one nanosecond or greater, or signal bandwidths less than about 1000 MHz, for normal-incidence altimeter geometry. On the above basis, samples of the sea-surface impulse response can be generated by selecting random numbers.

Assuming that the clutter is "frozen" during the period of the r-f pulse (rectangular of length T,) the scattered signal would be of the form

$$h_c(t - T) * [U(t) - U(t - T)]$$

where U(t) is a step function.

The pulse response for a particular sample function of h_c thus consists of a transient period (the integral of the impulse response) followed by a steady state period in which the output is a moving average over the time interval T. The sample functions given in Fig. 2-1 are examples of detected sea-return for rectangular pulse illumination.

This model of sea-return also leads to the Rayleigh description of radar return. The scattered signal will be a sum of phasors.

$$\sigma_n e^{j\theta_n} .$$

This expression, which consists of a random collection of phasors, leads to the well known Rayleigh probability distribution. Since the step response is the integral of the impulse response, the Rayleigh model can be shown to lead to a time-varying Gaussian envelope distribution of the form

$$P(v) = \frac{1}{\sqrt{2\pi\gamma t}} \exp\left\{\frac{-v^2}{2\gamma t}\right\} \qquad t \leq T$$

where γt is the process variance. P(v) will be a Wiener Levy process[2] in which the variance increases linearly with time. For the above model the spectrum (the Fourier transform of $h_c(t)$) will be nearly constant up to some frequency on the order of the reciprocal of the correlation time (<1 ns). The bandwidth requirements for a signal which accurately probes the sea-return impulse response can thus be estimated. Visualizing the above described spectrum as one corresponding to a linear system, it is obvious that the exploring signal must contain frequency components

that extend throughout the transform of $h_c(t)$. Therefore a signal that is designed to make complete measurements of the impulse response sample functions must contain frequency components in the gigahertz range. The measurement of this quantity is of concern in the radar altimeter design. As discussed in Section II, one of the problems in design of a system which attempts to estimate the mean value of a fluctuating signal, is the problem of obtaining an adequate number of independent samples. For a transmitted pulse length in the order of 50 nanoseconds, errors arising from self noise appear to be comparable to thermal noise errors. Therefore design of a precision altimeter may greatly benefit from improved knowledge of the characteristics of the received signal. Conventional (non-adaptive) matched filter IF bandwidth criteria may not be appropriate since, for unequal errors in the two sources, an optimum bandwidth would be expected to exist.

With these qualitative remarks on signal processing considerations, the subjects of detection and parameter estimation will be considered. The parameter estimation problem is simplified by considering signals existing in the IF, since the statistics are time-varying Gaussian at this point. Otherwise, non-Gaussian statistics must be considered.

Neglecting, for the time being, the non-deterministic nature of the scattered signal, the optimum processor for measuring range (time of arrival) in the presence of additive Gaussian noise will be considered. For a partially coherent system the processor shown in Fig. C-1 is optimum. This processor consists of quadrature detectors, matched filters, and a bank of correlators [3-4].

The limitation of the above theory is that it does not take into account the random nature of the received signal. The fluctuating altimeter signal is strongly akin to multipath signals encountered in radar astronomy and scatter communications. The solution to this problem, due to Kailath[5], is diagrammed in Fig. C-2. The estimation filter H shown in Fig. C-2 is derived from the equation

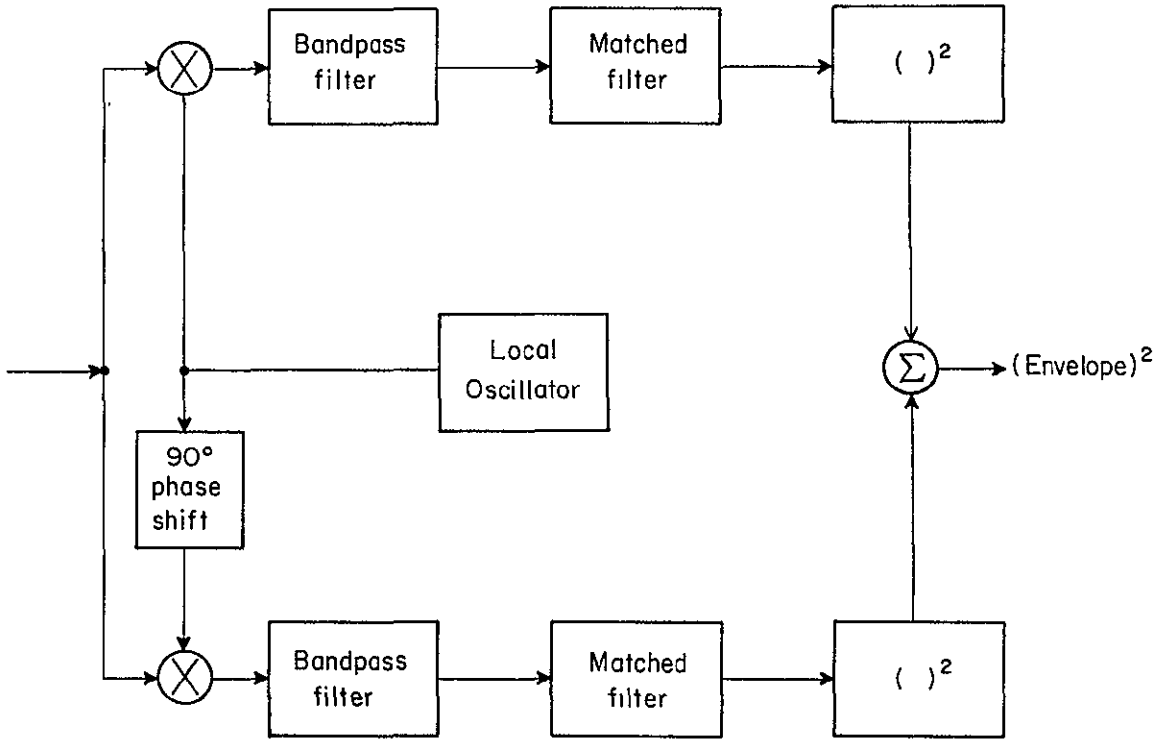

Fig. C-1. Matched Filter Processor for Estimating Time Delay

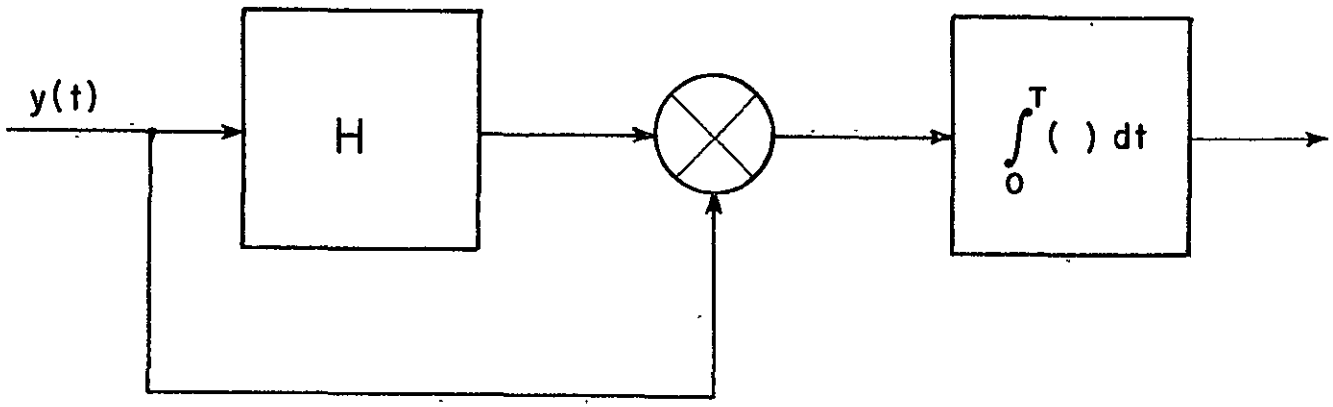

Fig. C-2. Optimum Filter Due to Kailath

$$H = (1+\Lambda_n \Lambda_{sy})$$

where Λ_n is the noise covariance and Λ_{sy} is the covariance of the channel output y(t).

The scattering function $\sigma(\tau)$ approach developed by Price and Green[6] and discussed by Evans and Hagfors[7] will be reviewed next. This approach is based on the likelihood ratio of the form

$$\iint_{-\frac{T_o}{2}}^{\frac{T_o}{2}} W_o(t)\, W_o(t')\, \phi_g\,(t,t')\, dt\, dt'$$

Where T_o is the observation time,

W_o is a sample observation of the received signal, and

ϕ_g is the echo correlation function.

This last quantity is related to the scattering function through the relationship

$$\phi_g(t,t') = \frac{1}{2}\,\mathrm{Re}\left[\exp\,[jw_o(t - t')] \int_{-\infty}^{\infty} X(t - \tau)\, X^*(t' - \tau)\, L_y(t - t', \tau)\, d\tau\right]$$

in which X(•) is the complex transmitted envelope and L_y is given by

$$L_y(\Delta t,\tau) = \iint_{-\infty}^{\infty} \sigma\,(w,\tau)\; e^{jw\Delta t}\; dw\ .$$

The solution to this set of equations provides what is termed the "practically optimum" processor[7]. The optimum range estimation technique, for a target spread in both delay and Doppler, consists of a bank of processors spaced in range and the receiver chooses the processor exhibiting the largest output. This filter shown in Fig. C-3 is termed a weighted radiometer, in contrast to a matched filter envelope detector. The first filter shown in this figure is one matched to the transmission replica s(t). This is followed by a squarer (envelope detector) and a filter matched to the mean target delay characteristics. The impulse response of the latter is

$$h(t) = H^2(\tau_n - t)$$

where $H^2(t)$ is the square of the filter matched to the scattering function $\sigma(\omega_o, t)$. Thus for fluctuations small relative to the spectrum of $s(t)$, the impulse response is essentially $\sigma(t)$. This form of processor is shown in Ref. 7 to be optimum if 1) a Gaussian pulse is used, 2) $\sigma(\tau,\omega)$ is factorable in τ and ω, and 3) if the observations extend over all time.

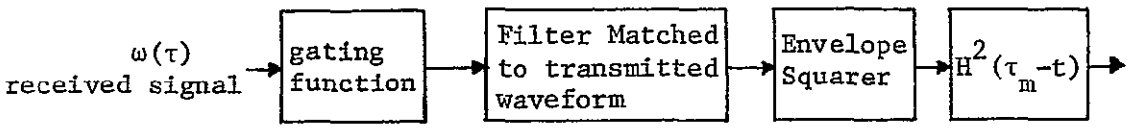

Fig. C-3.

The implementation of such a processor in the altimeter does not appear promising. The only novel feature is the video filter matched to the target time-profile. Based on our previous discussion, the filter would have an impulse response of the type shown in Fig. 4-C.

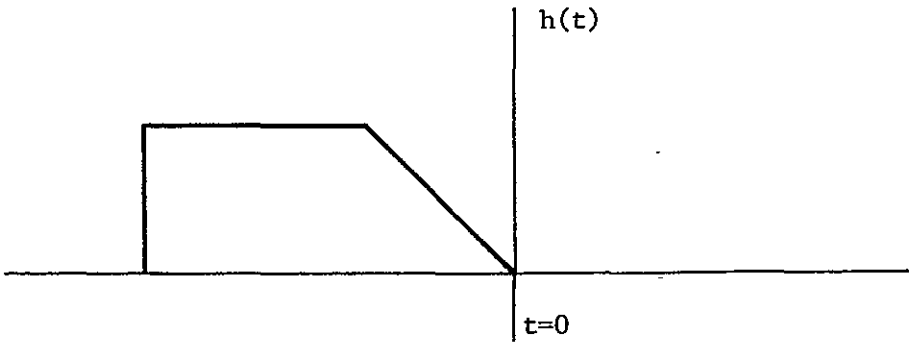

Fig. C-4.

In practice, realizability would require some time delay. However, its general form appears to be an "integrate and dump" circuit, which is similar to the split-gate concept studied on the altimeter program.

This discussion indicates that the synthesis of the above type of optimum processors will not yield substantial improvements over the present ad hoc techniques. The areas of waveform synthesis and adaptive filtering should be investigated.

Appendix C

REFERENCES

[1] Skolnik, M. I., "A Review of Radar Sea Echo", Naval Res. Lab Washington, D. C., Report No. 2025, July 1969.

[2] Papoulis, A., Probability, Random Variables and Stochastic Processes, McGraw Hill Book Company, New York, 1965.

[3] Di Franco, J. V. and W. L. Rubin, Radar Detection, Prentice Hall Inc. Englewood Cliffs, New Jersey, 1960.

[4] Van Trees, H. L., Detection Estimation and Modulation Theory, John Wiley Company, New York, 1967.

[5] Kailath, T., "Correlation Detection for Signals Perturbed by a Random Channel," IRE Trans. on Information Theory, June 1960, p. 361-366.

[6] Price, R., and P. E. Green, "Signal Processing in Radar Astronomy," MIT Technical Report 234, Cambridge, Mass., 1960.

[7] Evans, J. V. and T. Hagfors, Radar Astronomy, McGraw Hill, New York, 1968.

APPENDIX D

Analysis of Ocean Surface Effects on the Received Waveform

In order to account for the rough sea surface, it is necessary to compute the density of stationary points per unit area as a function of height above the mean sea surface. Rice[1] has examined the distribution of local maxima and minima for a bandlimited signal, which corresponds to a one-dimensional sea. Longuet-Higgins[2] examined the density of specular points with height above the sea surface. Making use of the latter work and the fact that the density of stationary points (specular points for normal incidence illumination) is four times the density of the maximum points, the distribution of stationary points per unit area may be established as a function of height above mean sea level (msl).

Formally, the required probability is given by

$$dp = \frac{4dz}{(2\pi)^{5/2}} |M|^{-1/2} \int_{-\infty}^{0} \int_{-\infty}^{0} z_{xx} z_{yy} \exp\left\{\frac{-1}{2|M|} [M_{11} z^2 + 2M_{14} z_{xx} + z_{yy} M_{15} + 2z_{xx} z_{yy} M_{45} + z_{xx}^2 M_{44} + z_{yy}^2 M_{55}]\right\} dz_{xx} dz_{yy}$$

where dp is the probability that a maximum exists between z and z + dz. z is the height of the surface above msl (a function of x and y), the position coordinates on the mean surface, and

$$z_{xx} = \frac{\partial^2 z}{\partial x^2}$$

$$z_{yy} = \frac{\partial^2 z}{\partial z^2}$$

and M_{ij} are elements of the correlation matrix for the random variables $z, \frac{dz}{dx}, \frac{\partial z}{\partial y}, \frac{\partial^2 z}{\partial y^2}, \frac{\partial^2 z}{\partial x^2}$. $|M|$ is the determinant of the correlation matrix.

The elements of the correlation matrix can be related to derivatives of the correlation function of the surface (and hence to the energy spectrum). For example:

$M_{11} = (0)$ the mean squared height of surface,

$$M_{14} = \frac{\partial^2 \psi}{\partial x^2}\bigg|_{x=y=0} = -\iint k_x^2 \, S(k_x, k_y) \, dk_x dk_y$$

$$M_{15} = \frac{\partial^2\psi}{\partial y^2}\Big|_{x=y=0} = -\iint k_y^2 S(k_x,k_y)\ dk_x dk_y$$

$$M_{44} = \frac{\partial^4\psi}{\partial x^4}\Big|_{x=y=0} = \iint k_x^4 S(k_x,k_y)\ dk_x dk_y$$

$$M_{45} = \frac{\partial^2\psi}{\partial x^2 \partial y^2}\Big|_{x=y=0} = \iint k_x^2 k_y^2\ S(k_x,k_y)\ dk_x dk_y$$

$$M_{55} = \frac{\partial^4\psi}{\partial y^4} = \Big|_{x=y=0} \iint k_y^4\ S(k_x,k_y)\ dk_x dk_y$$

This approach cannot be pursued because the moments involving k^2 and k^4 are not known to sufficient accuracy. For presently available oceanographic spectra, the last three integrals are infinite.

APPENDIX D

REFERENCES

1. Rice, S. O., "Mathematical Analysis of Random Noise", in Noise and Stochastic Processes, Dover Pub., New York, 1954, pp. 133-294.
2. Cartwright, D. E., and M. S. Longuet-Higgins, "The Statistical Distribution of Maxima of a Random Function", Proc. Roy. Soc. A237, pp. 212-232.